

COHERENT FEEDBACK AND CONTROL OF LINEAR  
QUANTUM STOCHASTIC DYNAMICAL SYSTEMS

A DISSERTATION  
SUBMITTED TO THE DEPARTMENT OF APPLIED PHYSICS  
AND THE COMMITTEE ON GRADUATE STUDIES  
OF STANFORD UNIVERSITY  
IN PARTIAL FULFILLMENT OF THE REQUIREMENTS  
FOR THE DEGREE OF  
DOCTOR OF PHILOSOPHY

Orion Crisafulli  
August 2012

© 2012 by Orion Steven Kwong-Yu Crisafulli. All Rights Reserved.  
Re-distributed by Stanford University under license with the author.



This work is licensed under a Creative Commons Attribution-Noncommercial 3.0 United States License.  
<http://creativecommons.org/licenses/by-nc/3.0/us/>

This dissertation is online at: <http://purl.stanford.edu/mg430qs7206>

I certify that I have read this dissertation and that, in my opinion, it is fully adequate in scope and quality as a dissertation for the degree of Doctor of Philosophy.

**Hideo Mabuchi, Primary Adviser**

I certify that I have read this dissertation and that, in my opinion, it is fully adequate in scope and quality as a dissertation for the degree of Doctor of Philosophy.

**Sebastian Doniach**

I certify that I have read this dissertation and that, in my opinion, it is fully adequate in scope and quality as a dissertation for the degree of Doctor of Philosophy.

**Shanhui Fan**

I certify that I have read this dissertation and that, in my opinion, it is fully adequate in scope and quality as a dissertation for the degree of Doctor of Philosophy.

**John M.J. Madey**

Approved for the Stanford University Committee on Graduate Studies.

**Patricia J. Gumport, Vice Provost Graduate Education**

*This signature page was generated electronically upon submission of this dissertation in electronic format. An original signed hard copy of the signature page is on file in University Archives.*

# Abstract

Coherent feedback will play an important role in the emerging field of quantum control, whose goal is to apply concepts from control engineering and dynamical systems theory to the realm of quantum systems in order to tailor system behavior and performance to suit the needs of scientific and engineering applications. In this thesis I present a system of coupled degenerate optical parametric oscillators (OPOs) that are arranged in a feedback configuration to demonstrate some basic principles of coherent feedback and control. A key point is that the system exhibits gain in the feedback loop, a fundamental component necessary for design flexibility of system dynamics. System behavior will be discussed from a perspective of control goals for narrow band disturbance rejection and amplification, as well stabilization control.



# Acknowledgements

The work presented in this thesis would not have been possible without the help and contributions of a great number of people, and I would like to take this space to acknowledge as many of them as I can.

First, I must thank my research advisor Professor Hideo Mabuchi, for his guidance and support throughout the PhD, and for assembling a team of graduate students whose members are outstanding both for their intellectual acuity and generosity as people. The welcoming atmosphere of the group and its commitment to education and integrity are a reflection of Hideo's personal philosophy, and I count myself as very fortunate to have been a part of the team. Throughout my initial years in the MabuchiLab, Tony Miller was instrumental in training me up on the optics and electronics used in the laboratory, and his approach to science and decency as a person have left an indelible impression on me; it indeed has been a pleasure to know him as a friend for so many years. I'd also like to thank my optical table mate, Yeong Dae Kwon, for his help with technical details and reliable company throughout the many days in lab; his work ethic and ingenuity, combined with his level of mastery of a certain real time strategy game continues to leave me in awe. The biophysics folks, Michael Zhang ("Dr. Little Mikey", my thesis writing buddy) and Charles Limouse provided continuous personal support, ranging from helping with the nitty gritty of assembling electronic components to just hanging out and having fun together, and their immediate predecessor Kevin McHale was very patient and generous with his advice in my early years in the lab. I'd like to thank Jie Wu for his staunch optimism and friendship, and his thoughtful attention to detail in his role as the group's laser safety officer. I'd also like to thank Joe Kerckhoff for friendly chats, wild humor

and reminding me about the impact that people can have through their individual efforts. Hendra Nurdin, who developed much of the initial theoretical framework that motivates the experimental work presented here, was very patient and open with his discussions, and it was great to have him as a collaborator; as well, Ryan Hamerly's work on quantum LQG controllers was crucial in getting basic intuition relevant for the experiment and providing it direction. As postdocs in our lab, Andrew Silberfarb and Luc Bouten also provided me with a lot of wisdom during the early years, and I'd like to thank our current postdoc, Armand Niederberger, for his friendship and supplying me with additional real-world wisdom in the final years of the program. And I'm grateful to Gopal Sarma, who in addition to providing friendship and intellectual camaraderie on a daily basis, stood fast for me in times of turmoil and went the extra mile for my personal well-being. I'd also like to wish Dodd Grey and Dong-Bang Tsai luck with their future endeavors in the group and to thank them for the good times.

With specific regards to my experiment, on the theory side, Nikolas Tezak contributed a substantial amount to the analysis and understanding presented here, and his willingness to slog through code development, debugging, as well as the sometimes abstruse physics involved in the modeling was critical to both predicting and explaining the physical results. On the data processing side, Dmitri Pavlichin was generous enough to lend his expertise in data filtering and statistical methods to get accurate, meaningful interpretations of the signals acquired by the laboratory equipment. On the electronics side, Hardeep Sanghera contributed to the design and construction of several key components including detectors, servos and amplifiers. Nate Bogdanowicz, in addition to investigating piezo-mechanical designs relevant to the experiment, also helped make a number of servos, amplifiers and auxiliary circuits. Finally, regarding the optics, electronics, theory, and pretty much everything else imaginable, Michael Armen ("Dr. Big Mikey"), our laboratory's research associate, helped with the design and practical realization of the experiment, and contributed heavily to the optical alignment, the designs for the electronics used and their integration into the experiment. His wisdom and mastery of all things laboratory, coupled with his generally empathic demeanor and uprightness, truly make him the "Catcher in the Lab", and the precision measurements and control done in this experiment would not

have been possible without his help (see fig. 1). Technical contributions aside, the above-mentioned colleagues have also been great pals, and their friendship has made the graduate school experience all the more worthwhile.

Outside the MabuchiLab at Stanford, there were a number of other colleagues in the Applied Physics, Physics and Electrical Engineering departments whose advice was especially helpful with obtaining an understanding of what would work in practice in the lab, based on their previous experience in nonlinear optics and mechanics. From the Byer-Feyer group, I'd specifically like to thank Carsten Langrock for his advice on acquiring nonlinear optical crystals and their behavior, Alireza Marandi for his discussions about the basics of optical parametric oscillators and their construction in lab. I'd also like to thank Derek Chang, Chris McGuinness, Jason Pelc from the same group, as well as Sonia Buckley and Michal Bajcsy from the Vuckovic group, and Chia-Ming Chang and Young Ik Sohn from the Solgaard group for their general advice and friendly chats in the basement atrium of the Nano building. I'd like to thank Peter McMahon from the Yamamoto group for his advice and perspective on the current state of affairs in the fields of quantum information science, and Yurika Peterman for her administrative support and willingness to practice Japanese with me, *ichi go ichi e*. Alicia Kollar, Alex Papageorge, Matt Naides and Nate Burdick from the Lev group were helpful in providing advice on various components that were needed in the setup (and, at times, the components themselves!), and were fun to hang out with. I'd also like to thank Kiarash Aghaie from the Dignonnet group with help with machining mechanical parts used in for optical alignment, and the staff of the Varian Physics Machine Shop, in particular Mehmet Solyali, for teaching me how to use the machines and extraordinary effort he put in over the years to give the students the best possible materials and techniques to use in the machining aspects of their projects. Thanks to the staff at Varian Physics receiving, in particular Dorrene Ross, Percy Medina and Lamont Wiley for their help with timely shipments to and from vendors, and the administrative staff in Applied Physics, in particular Paula Perron and Claire Nicholas for not only keeping students on track with their requirements, but for constantly being on the look out for opportunities for them and finding ways tailor their experiences for individual satisfaction. I'd also

like to give Mike Schlimmer an appreciative nod for overseeing the daunting task of the Nano building management, and for doing his utmost to minimize the impact of the construction and maintenance on experimental research inside. Rich Tiberio, our immediate neighbor in the Stanford Nanofabrication Facility and wizard of electronbeam optics, gave not only good engineering advice, but was also generous in sharing his experiences as I entered the job hunting phase at the end of my graduate career, as well as his healthy snacks and tips on pineapple raising. As for my friends here outside of my immediate research environment, I'd also like to thank my fellow Techers-moved-to-Stanford Matt Fisher, Victor Liu, and Shai Barak, as well as Mike Lesnick and Mike Huynh for the get-togethers, gaming, and general fun outside of lab. Finally, I'd like to thank the other members of my thesis committee, Professors Sebastian Doniach, John Madey, Shanhui Fan, Benjamin Lev, and Sanjay Lall for agreeing to serve on it and their support and feedback.

If I expand this circle of gratitude to include my time outside of Stanford, the number of people within it begins to grow exponentially, and even if I were to just list names, this section would still resemble the "Lord of Rings" ending credits, so from here on I'm going to keep it brief. I'd like to thank the previous generations of the MabuchiLab members and other graduate student friends from my time at Caltech, and in particular John Stockton, Raviv Perahia, Matt Lucas, Bill and Molly Jones, and Professor Ken Libbrecht for their earnest council and kind support at a critical turning point in my graduate career, as well as Sheri Stoll's cheerful welcome when I joined the group. I'd like to thank my friends and professors from my undergraduate days, who encouraged me to pursue my dreams of a career in science and friendship made my time on the East Coast something to get nostalgic about; specifically, Paul Oreto, Brad Hill, Eric Harkleroad, Erik Nielsen, Matt Ong, and Weining Man, as well as Professors Edgar Choueiri, Michael Littman, Paul Steinhardt and Oluwole Soboyejo. I'd also like to thank my friends and mentors at the University of Hawaii where I spent my undergraduate summers, especially Frank Price and Troy Hix for acting as my grad student *sempai*, Professor Eric Szarmes for working with me on the very first physics project I did out of high school, and Professor John Madey for what has now become more than a decade of advice, support and mentorship that has

been formative for my scientific career and growth as a person. I'd like to recognize the many extraordinary teachers and I had from kindergarten through 12th grade at Punahou School in Hawaii, whose educational philosophy emphasized treating others with compassion and respect, as well as intellectual freedom; Mike Gearen, Susan Field, John Proud and Ruth Fletcher encouraged my interest in science and mathematics, and Amy Mitsuda, John Bridges and Susan Rudosky encouraged my growth as a musician. The multitude of personal friends from that period of my life continue to inspire me to try my best, and I'd like to recognize those who I've kept in touch with for several decades, and in particular Jeff Loh, Joseph Madamba and Richard Li and their families for treating me as part of their own.

Almost last but far from least, I'd like to thank the members of my family. I'd like to thank my grandparents who have passed away for the extraordinary kindness and generosity towards me during the times we were together, and my grandmother who is still with us for thinking of me every day and inspiring me to be a better person. I'd like to thank my uncle Fuk and his family for taking care of me during all the times I stayed with them (and congratulate them on the success of the Mars Science Lab mission and the landing of the Curiosity rover), and my uncle Rob for the musical fun and intellectualism he's brought to my life. Finally, I'd like to thank my parents, BM and BD, for my existence, and raising me in a loving way so that I can be the person I am today. They made many sacrifices along the long and arduous road of parenthood to try to give BS (me) the "best life possible". In a somewhat vicarious sense, with this, the PhDs they left unfinished in order to spend more time with me will finally be complete.

Lastly, I'd like to thank you, the reader, for reading this, which in principle gives this document its *raison d'être*. I wish the future generations of graduate students, researchers, and otherwise curious people who come across this work the best with their endeavors, and hope that it may aid them in their quests to unravel the mysteries of the universe.



Figure 1: Camera still of the Catcher in the Lab, a rare specimen indeed. Surrounding aura indicates high technical capability and strong adherence to principles. Approach with humorous intent.

# Contents

<b>Abstract</b>	<b>iv</b>
<b>Acknowledgements</b>	<b>v</b>
<b>1 Introduction</b>	<b>1</b>
<b>2 Theory</b>	<b>8</b>
2.1 ABCD models . . . . .	8
2.2 Coherent inputs . . . . .	11
2.3 Dynamic and steady state properties of the system . . . . .	12
2.4 The squeezing spectrum . . . . .	14
2.5 System variables . . . . .	15
2.6 Output power . . . . .	17
2.7 The linear optical parametric oscillator model . . . . .	18
2.8 Steady state photon number . . . . .	20
2.9 Transmission spectrum/transfer function . . . . .	21
2.10 Concrete OPO models for our setup . . . . .	22
2.11 The setup as an LQG problem . . . . .	29
<b>3 Experimental Setup</b>	<b>33</b>
3.1 Master laser and beam generation . . . . .	33
3.2 OPO specs, pump coupling, and feedback loop . . . . .	38
3.3 Locking schemes . . . . .	42
3.4 Detuned coherent input and optical noise generation . . . . .	46

3.5	Homodyne detection . . . . .	47
<b>4</b>	<b>Experimental Results</b>	<b>49</b>
4.1	OPO characterization . . . . .	49
4.2	Narrowband disturbance rejection and amplification . . . . .	52
4.3	System stability modification . . . . .	60
4.4	Future directions . . . . .	62
<b>A</b>	<b>Bowtie Cavity Design</b>	<b>64</b>
A.1	Geometry and Stability Range . . . . .	64
A.2	Effects of Intracavity Crystal and Astigmatism . . . . .	72
A.3	Cavity Frequency Response . . . . .	75
<b>B</b>	<b>Electronics for locking and detection</b>	<b>81</b>
<b>C</b>	<b>SHG and OPA with <math>\chi^{(2)}</math> crystals in practice</b>	<b>88</b>
C.1	Second harmonic generation . . . . .	88
C.2	Optical parametric amplification . . . . .	99
	<b>Bibliography</b>	<b>101</b>



# List of Tables

2.1	Physical model parameters . . . . .	26
-----	-------------------------------------	----

# List of Figures

1	The Catcher in the Lab . . . . .	x
1.1	Aircraft control surfaces for modern jetliners . . . . .	2
1.2	Underlying control structure for aircraft control surfaces . . . . .	3
1.3	Feedback control schematic . . . . .	3
1.4	Coherent feedback control system with gain . . . . .	6
2.1	Equivalent ways to diagram the circuit expression . . . . .	24
2.2	Simplification of the lossy circuit expression. . . . .	32
3.1	Schematic of the full experimental apparatus . . . . .	34
3.2	Apparatus front and back . . . . .	35
3.3	MOPA front and back . . . . .	36
3.4	Frequency doubling setup . . . . .	37
3.5	PPLN crystal and second harmonic generation . . . . .	38
3.6	Degenerate OPO functional schematic . . . . .	40
3.7	Plant and controller OPO pictures . . . . .	40
3.8	Cavity and phase locking schemes . . . . .	45
3.9	Pumping both OPOs . . . . .	48
4.1	Controller OPO gain vs pump power . . . . .	50
4.2	Plant OPO gain vs pump power . . . . .	51
4.3	Effects of resonant feedback without gain . . . . .	54
4.4	Effects of resonant feedback with gain . . . . .	55
4.5	Effects of pump when feedback phase locked to maximize photon number	57

4.6	Effects of pump when feedback phase locked to minimize photon number	58
4.7	Suppressing lasing in the combined system by locking the coherent feedback phase . . . . .	59
4.8	Coherent feedback performance with detuned coherent inputs . . . .	60
4.9	Plant lasing threshold reduction . . . . .	61
A.1	Bowtie cavity schematic . . . . .	65
A.2	Bowtie stability region . . . . .	69
A.3	Bowtie example . . . . .	71
A.4	Cavity circulating power . . . . .	78
A.5	Cavity reflected and transmitted powers . . . . .	79
B.1	Integral control servo used for locking . . . . .	82
B.2	High voltage amp to drive piezos . . . . .	83
B.3	Reset circuit for piezo position . . . . .	84
B.4	Detector used to measure OPO cavity transmission . . . . .	85
B.5	Subtracting detector circuit for balanced homodyne detection . . . .	86
B.6	Output buffer for subtracting detector . . . . .	87
C.1	Multi-watt second harmonic generation on a single pass through PPLN	90
C.2	Single watt second harmonic generation on a single pass through PPKTP	92
C.3	Temperature tuning phase matching profile for PPKTP . . . . .	94
C.4	Decrease in optimal phase matching temperature for PPLN with increasing fundamental power . . . . .	95
C.5	Phase matching for PPKTP with constant temperature vs laser frequency	97

# Chapter 1

## Introduction

Feedback control engineering is crucial to the design of systems and technologies that enable our modern lifestyles [1]. Modern passenger aircraft serve as good examples of the remarkable integration and control of a vast array of different physical systems (mechanical, electrical, aerodynamical, optical, chemical, structural and human) that allow us to not only realize the dream of flight, but to make it practical for travel and accessible to many (see figs. 1.1 and 1.2). At its core, feedback control engineering describes how dynamical systems should be connected when some part of the output of a system to be controlled (henceforth called the "plant") is fed back to a system that is driving it, in order to help achieve a desired control objective (see fig. 1.3). Much progress has been made in the last two centuries to work out both the principles and realizations of feedback control systems for macroscopic systems, but as our attention shifts to the control of systems at the micro- and nano-scale where coherent and quantum effects become important, the need to modify our existing theoretical tools and methodologies to accommodate inherent differences in system dynamics becomes clear.

Feedback control schemes for macroscopic systems rely on measurement-based feedback, where the state of the system to be controlled is monitored by measuring one or more of its outputs, and then feedback is applied via actuators to control the system based on the measurements made. Measurement-based feedback is also an effective approach for the control of quantum systems, and has been studied from

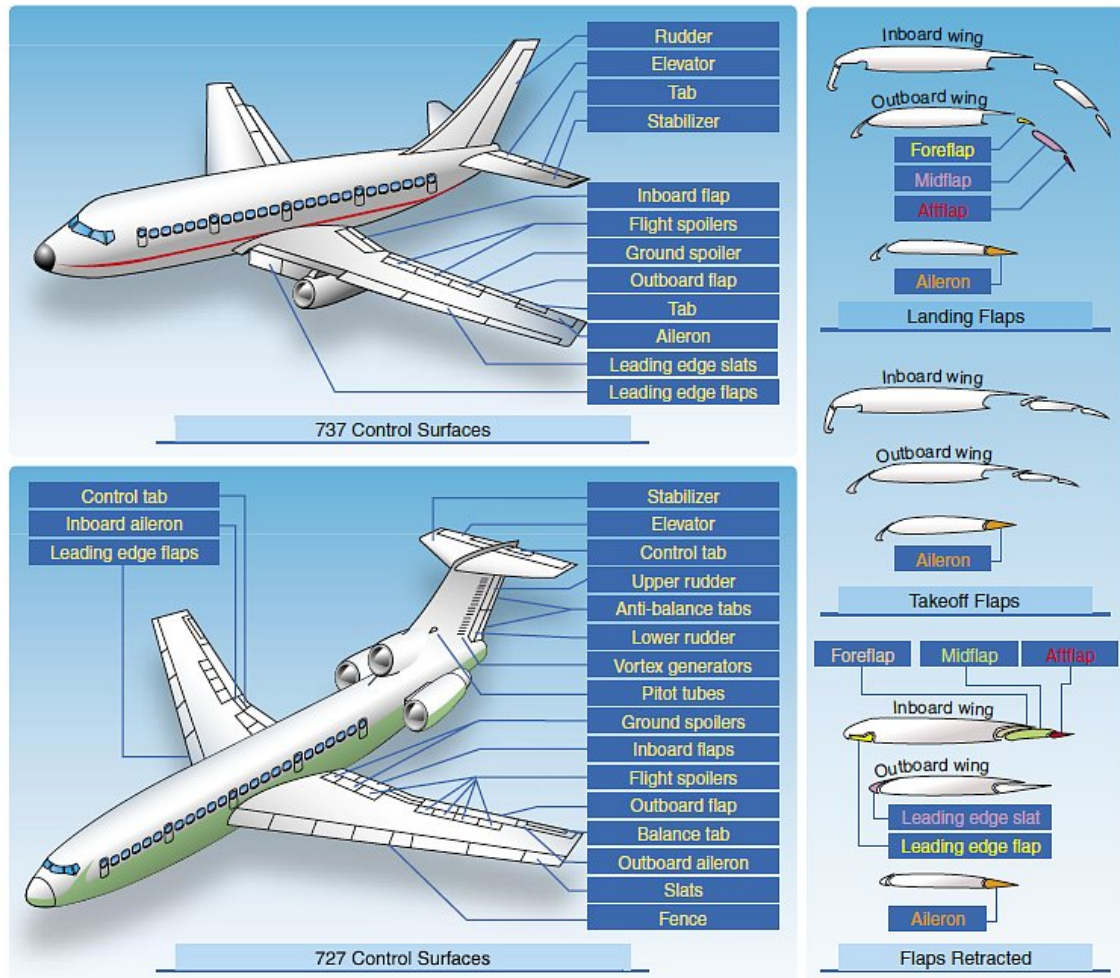


Figure 1.1: Aircraft control surfaces on a couple of representative modern jetliners, a sampling of the many systems that are integrated into the master control system operated by the pilots. Image courtesy of [www.ahrtp.com](http://www.ahrtp.com).

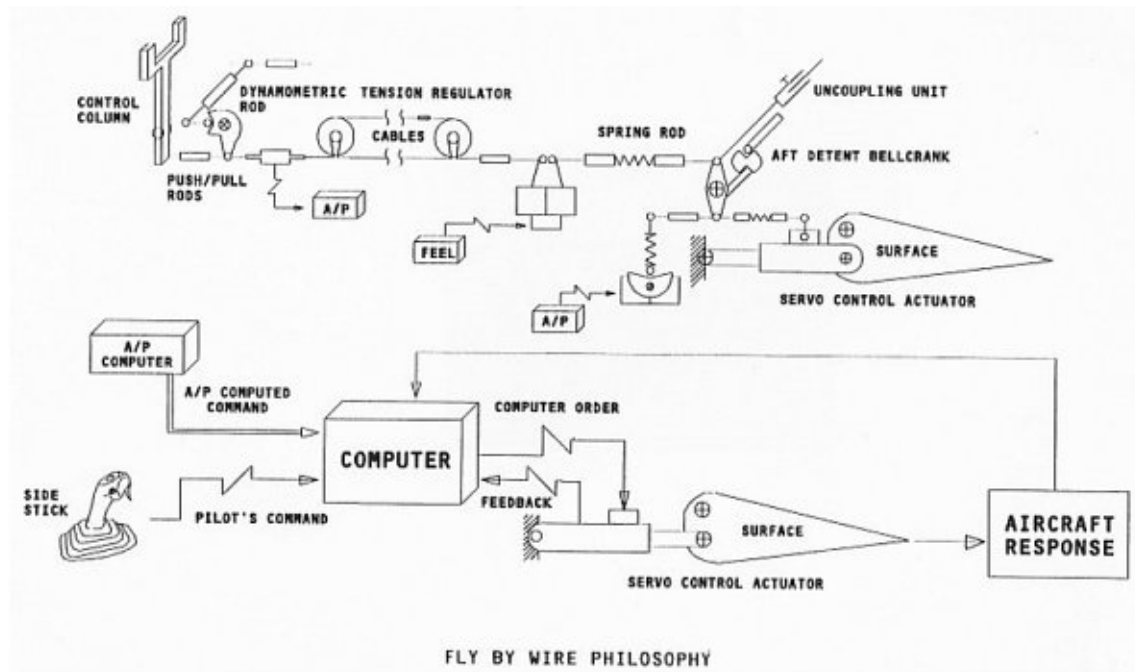


Figure 1.2: Underlying control structure for aircraft control surfaces. Note the inclusion of both open loop (direct input from the pilot) and closed loop (feedback) control. Ideally, the pilot input is also part of the feedback loop in that the humans flying the plane should take the sensor readings into account and make adjustments for a safe and comfortable flight. Image courtesy of [www.ahrtp.com](http://www.ahrtp.com).

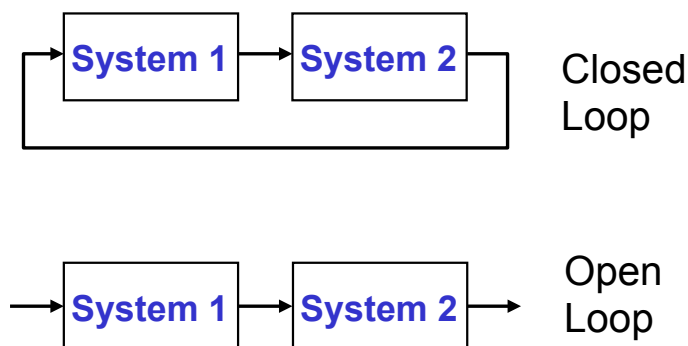


Figure 1.3: Two basic system control configurations. On the bottom, the output of system 1 is fed into system 2 to drive it, but there's no feedback to system 1 (open loop control). On top, the output of system 2 is fed back into system 1, thereby forming a feedback loop (closed loop control).

both the perspective of a theoretical framework [2, 3, 4, 5], as well as realization in the laboratory [6, 7, 8, 9, 10]. However, such schemes will always introduce some noise associated with the effects of quantum back-action during measurements [11, 12], and while the effects of the back-action may be accounted for in the control scheme [10], there is still the need to amplify the quantum signals to classical, macroscopic levels during processing in the feedback loop. This presents significant limitations in the design of the controllers, not just in terms of the absolute performance that they can achieve, but also in terms of their power requirements, processing speed and the degree to which they can be integrated into an architecture that consists of an ensemble of nanoscale systems [13].

One important control scheme that circumvents some of the difficulties involved in measurement-based feedback schemes is that of *coherent* control, where part of the system output is sent to the controller for processing and fed back to the system without measurement, so that the controller is driven by signals that share the same correlations as those inherent to the plant, and additional noise associated with measurements is not introduced [14, 15, 16]. In addition to the potential of outperforming measurement based schemes in low excitation regimes [17, 18] and lowering power utilization [19], coherent feedback schemes readily enable the use of similar, nanoscale systems for controller implementation and thus represent a suitable methodology to use in the design of integrated, embedded autonomous controllers [20, 21]. This is desirable not only for applications involving quantum information processing and error correction, but also those in which coherent information is processed over substantial distances (e.g. remote sensing) so that rapid signal propagation and low loss become important [22].

While many important problems of interest in this field involve systems with nonlinear dynamics [20, 21, 19], the behavior of linear systems remains an important underpinning of our understanding of quantum and coherent control. By linear, we mean that the system dynamics can be described by a set of quantum stochastic differential equations [23, 24, 25] that are linear in the state variables and quantum correlated noises. The study of linear systems has facilitated the development of the quantum analogs of powerful control paradigms in classical control theory including

$H^\infty$  and LQG control [26, 27], and provides a natural platform to contrast ideal, quantum-limited performance of coherent controllers with their classical counterparts [17, 18]. To date, a few landmark implementations of coherent feedback controllers for linear systems have been realized, and have provided some basic intuition about the performance and limitations of this control scheme for problems including coherent broadband disturbance rejection [15] and enhancement of optical field quadrature squeezing [16]. Up until now, however, the feedback loops in these controllers have been missing an important design element that is generally necessary to optimize controller performance (in both classical and coherent scenarios): *gain*.

Gain in the feedback loop allows a wide variety of modifications to be made to the closed loop dynamics of a system, including changing system stability behavior, and plays a central role in the prescription for a systematic approach to constructing arbitrary dynamical systems from fundamental building blocks [1, 28]. In this work, we examine the behavior of coherent control in a pair of coupled degenerate optical parametric oscillators (OPOs) joined together in a feedback loop configuration, where the output of one OPO (the "plant") is fed into a second OPO (the "controller") for processing, and then returned to the plant through a different port (see fig. 1.4). When the controller OPO is pumped, it acts as a quantum noise limited phase sensitive amplifier in the feedback loop and can exhibit gain for the right phase matching conditions between the pump and signal beams. We explore the effects of gain in the context of two problems: narrowband coherent disturbance rejection (as well as amplification), and modification of system stability behavior. Although to some extent the physical behavior of the closed loop system can be intuited from the well-known behavior of the individual OPOs in an open loop configuration, closing the loop introduces a strong dependence on an additional system phase (the phase accumulated around the feedback loop, henceforth referred to as the coherent feedback phase  $\Phi_{\text{FB}}$ ) that significantly impacts the system dynamics and the effects of gain. Moreover, accurate simulation of the closed loop system that accounts for the finite bandwidth of the controller, relative phases between signal and pump, feedback phase, cavity detunings, and parameter fluctuations due to ambient technical noise is a challenging task. Thus, the experiment is crucial to help pinpoint the parameter regimes of



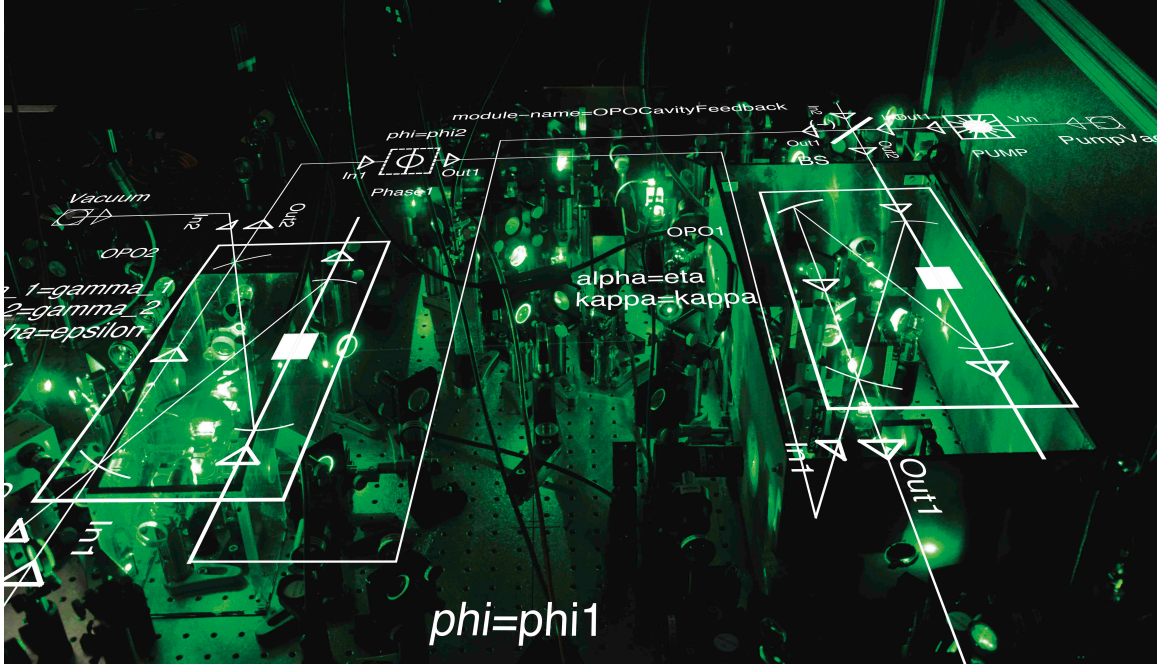


Figure 1.4: Overlay of functional schematic over experimental setup, which consists of 2 OPOs in a feedback loop configuration to implement a coherent feedback system with gain. The OPO on the left serves as the "plant" cavity, while the OPO on the right as the "controller", with the feedback and pump beam paths visible on the overlay traces (see Chapter 3 for more details). The green glow comes from the second harmonic pump beams injected into each OPO. High quality photography courtesy of Mike Zhang and Armand Niederberger, immaculate overlay courtesy of Nik Tezak.

interest for control problems as discussed above and guide theoretical development for practical realizations of coherent controllers.

The rest of this thesis is organized as follows: Chapter 2 details a theoretical framework that governs the behavior of general linear quantum stochastic dynamical systems and some predictions for the specific system at hand. Chapter 3 describes the experimental apparatus, the specs of the components involved and technical challenges encountered in building and stabilizing its behavior. Chapter 4 presents the results of system characterization, its performance in achieving narrowband disturbance rejection and modifying system stability, as well future experiments to clarify system limitations and new regimes of behavior. The 3 appendices are meant to give some helpful details of the experimental setup to aid the next researcher(s) in

working with the apparatus or designing similar systems. Appendix A covers the design methodology used for the OPO bowtie ring cavities. Appendix B shows the explicit details of the homemade analog electronic circuits used for locking servos, high voltage amplifiers and photodetection. Finally, Appendix C contains some advice for optimizing the nonlinear optical processes (second harmonic generation and degenerate parametric amplification) in the crystals with respect to beam alignment, phase matching and crystal deterioration.

# Chapter 2

## Theory

In this Chapter we discuss the theory appropriate for general linear quantum stochastic dynamical systems as well the specifics relevant for our coupled optical parametric oscillator (OPO) system of interest in the feedback configuration. As mentioned in the previous Chapter, the system dynamics are well described via the formalism of quantum stochastic differential equations (QSDEs) [23, 24, 25, 29] and considerable work has been done to augment this theoretical framework with concepts from control and systems engineering [30, 31, 28, 27, 26] for application to networks of linear quantum optical systems. Here, we utilize some of the standard tools developed in the previous work, namely the "SLH" description for the governing dynamics of each system component and the series and concatenation products for joining them to form more complex systems. The reader is referred to the above references for the background needed to understand the notation used below.

### 2.1 ABCD models

For the special case where the internal degrees of freedom  $\{a_j, a_j^\dagger\}$  are given by a collection of quantum harmonic oscillators  $[a_j, a_k^\dagger] = \delta_{jk}$  with a Hamiltonian quadratic

in the mode operators

$$H = \mathbf{a}^\dagger \boldsymbol{\Omega}_- \mathbf{a} + \frac{1}{2} \mathbf{a}^\dagger \boldsymbol{\Omega}_+ \mathbf{a}^* + \frac{1}{2} \mathbf{a}^T \boldsymbol{\Omega}_+^* \mathbf{a} \quad (2.1)$$

$$\text{where } \boldsymbol{\Omega}_-^\dagger = \boldsymbol{\Omega}_- \in \mathbb{C}^{N \times N}, \quad \boldsymbol{\Omega}_+ = \boldsymbol{\Omega}_+^T \in \mathbb{C}^{N \times N}, \quad (2.2)$$

a scalar valued scattering matrix  $\mathbf{S} \in \mathbb{C}^{M \times M}$  and a linear coupling vector

$$\mathbf{L} = \mathbf{C}_- \mathbf{a} + \mathbf{C}_+ \mathbf{a}^*, \quad (2.3)$$

$$\text{where } \mathbf{C}_-, \mathbf{C}_+ \in \mathbb{C}^{M \times N} \quad (2.4)$$

the equations of motion of the mode operators are linear. For this system with input noises  $\mathbf{dB}$  and in particular this form of  $\mathbf{S}$  and  $\mathbf{L}$  we have the following quantum stochastic differential equation for the internal mode operators

$$d\mathbf{a} = \left( -i[\mathbf{a}, H] - \frac{1}{2}[\mathbf{a}, \mathbf{L}^\dagger] \mathbf{L} + \frac{1}{2}[\mathbf{a}, \mathbf{L}^T] \mathbf{L}^* \right) dt - [\mathbf{a}, \mathbf{L}^\dagger] \mathbf{S} d\mathbf{B} + [\mathbf{a}, \mathbf{L}^T] d\mathbf{B}^* \mathbf{S}^* \quad (2.5)$$

$$= \left[ -i\boldsymbol{\Omega}_- \mathbf{a} - i\boldsymbol{\Omega}_+ \mathbf{a}^* - \frac{1}{2} \mathbf{C}_-^\dagger (\mathbf{C}_- \mathbf{a} + \mathbf{C}_+ \mathbf{a}^*) + \frac{1}{2} \mathbf{C}_+^T (\mathbf{C}_-^* \mathbf{a}^* + \mathbf{C}_+^* \mathbf{a}) \right] dt \quad (2.6)$$

$$- \mathbf{C}_-^\dagger \mathbf{S} d\mathbf{B} + \mathbf{C}_+^T \mathbf{S}^* d\mathbf{B}^* \quad (2.7)$$

$$= \left[ \left( -i\boldsymbol{\Omega}_- - \frac{1}{2} \mathbf{C}_-^\dagger \mathbf{C}_- + \frac{1}{2} \mathbf{C}_+^T \mathbf{C}_+^* \right) \mathbf{a} + \left( -i\boldsymbol{\Omega}_+ - \frac{1}{2} \mathbf{C}_-^\dagger \mathbf{C}_+ + \frac{1}{2} \mathbf{C}_+^T \mathbf{C}_-^* \right) \mathbf{a}^* \right] dt \quad (2.8)$$

$$- \mathbf{C}_-^\dagger \mathbf{S} d\mathbf{B} + \mathbf{C}_+^T \mathbf{S}^* d\mathbf{B}^* \quad (2.9)$$

It turns out that this equation is valid both as an Ito QSDE and a Stratonovich QSDE, because all noise increments have scalar coefficients. Using the doubled-up notation  $\check{\mathbf{a}} = \begin{pmatrix} \mathbf{a} \\ \mathbf{a}^* \end{pmatrix}$  and  $\check{\Delta}(\mathbf{X}, \mathbf{Y}) = \begin{pmatrix} \mathbf{X} & \mathbf{Y} \\ \mathbf{Y}^* & \mathbf{X}^* \end{pmatrix}$  from [31, 28] we can combine the

equations of motion for  $\mathbf{a}$  and  $\mathbf{a}^*$  into a single one:

$$d\check{\mathbf{a}} = \check{\Delta}(\mathbf{A}_-, \mathbf{A}_+) \check{\mathbf{a}}dt + \check{\Delta}(\mathbf{B}_-, \mathbf{B}_+) d\check{\mathbf{B}} \quad (2.10)$$

$$= \mathbf{A}\check{\mathbf{a}}dt + \mathbf{B}d\check{\mathbf{B}} \quad (2.11)$$

$$\mathbf{A}_- = -i\boldsymbol{\Omega}_- - \frac{1}{2}\mathbf{C}_-^\dagger \mathbf{C}_- + \frac{1}{2}\mathbf{C}_+^T \mathbf{C}_+^* \quad (2.12)$$

$$\mathbf{A}_+ = -i\boldsymbol{\Omega}_+ - \frac{1}{2}\mathbf{C}_-^\dagger \mathbf{C}_+ + \frac{1}{2}\mathbf{C}_+^T \mathbf{C}_-^* \quad (2.13)$$

$$\mathbf{B}_- = -\mathbf{C}_-^\dagger \mathbf{S} \quad (2.14)$$

$$\mathbf{B}_+ = \mathbf{C}_+^T \mathbf{S}^* \quad (2.15)$$

Similarly, the input output relation can be expressed as

$$d\check{\mathbf{B}}' = \check{\Delta}(\mathbf{C}_-, \mathbf{C}_+) \check{\mathbf{a}}dt + \check{\Delta}(\mathbf{S}, \mathbf{0}) d\check{\mathbf{B}} \quad (2.16)$$

$$= \mathbf{C}\check{\mathbf{a}}dt + \mathbf{D}d\check{\mathbf{B}} \quad (2.17)$$

From this we can easily read off

$$\mathbf{A} = \check{\Delta}(\mathbf{A}_-, \mathbf{A}_+) \in \mathbb{C}^{2N \times 2N} \quad (2.18)$$

$$= \check{\Delta}(-i\boldsymbol{\Omega}_-, -i\boldsymbol{\Omega}_+) - \frac{1}{2}\check{\Delta}(\mathbf{C}_-^\dagger, -\mathbf{C}_+^T) \check{\Delta}(\mathbf{C}_-, \mathbf{C}_+) \quad (2.19)$$

$$= \check{\Delta}(-i\boldsymbol{\Omega}_-, -i\boldsymbol{\Omega}_+) - \frac{1}{2}\mathbf{C}^\flat \mathbf{C} \quad (2.20)$$

$$\mathbf{B} = \check{\Delta}(\mathbf{B}_-, \mathbf{B}_+) = -\check{\Delta}(\mathbf{C}_-^\dagger, -\mathbf{C}_+^T) \check{\Delta}(\mathbf{S}, \mathbf{0}) = -\mathbf{C}^\flat \mathbf{D} \in \mathbb{C}^{2N \times 2M} \quad (2.21)$$

$$\mathbf{C} = \check{\Delta}(\mathbf{C}_-, \mathbf{C}_+) \in \mathbb{C}^{2M \times 2N} \quad (2.22)$$

$$\mathbf{D} = \check{\Delta}(\mathbf{S}, \mathbf{0}) \in \mathbb{C}^{2M \times 2M} \quad (2.23)$$

If we write the boson field increments as  $d\check{\mathbf{B}} = \check{\mathbf{b}}dt$ , we can rewrite the equations of motion as

$$\dot{\check{\mathbf{a}}} = \mathbf{A}\check{\mathbf{a}} + \mathbf{B}\check{\mathbf{b}} \quad (2.24)$$

$$\check{\mathbf{b}}' = \mathbf{C}\check{\mathbf{a}} + \mathbf{D}\check{\mathbf{b}} \quad (2.25)$$

Instead of starting with an SLH model, one could also start with an ABCD model and try to synthesize a corresponding SLH model in terms of interconnected beamsplitter, cavity, and parametric oscillator models. As one might expect from the general redundancy in our doubled-up notation related to the fact that we must always preserve the canonical commutation relations for oscillator and field degrees of freedom, there exist some constraints on these matrices [28, 27].

## 2.2 Coherent inputs

Adding coherent inputs is straightforward. For a constant coherent input vector (one entry for each channel/port)  $\mathbf{w} \in \mathbb{C}^M$ , the Hamiltonian and the coupling vector need to be adjusted to

$$H \rightarrow H + \frac{1}{2i} \left[ \left( \mathbf{a}^\dagger \mathbf{C}_-^\dagger + \mathbf{a}^T \mathbf{C}_+^\dagger \right) \mathbf{S} \mathbf{w} - \mathbf{w}^\dagger \left( \mathbf{S}^\dagger \mathbf{C}_- \mathbf{a} + \mathbf{S}^\dagger \mathbf{C}_+ \mathbf{a}^* \right) \right] \quad (2.26)$$

$$= H + \frac{1}{2i} \left[ \mathbf{a}^\dagger \left( \mathbf{C}_-^\dagger \mathbf{S} \mathbf{w} - \mathbf{C}_+^T \mathbf{S}^* \mathbf{w}^* \right) - \left( \mathbf{w}^\dagger \mathbf{S}^\dagger \mathbf{C}_- - \mathbf{w}^T \mathbf{S}^T \mathbf{C}_+^* \right) \mathbf{a} \right] \quad (2.27)$$

$$\mathbf{L} \rightarrow \mathbf{L} + \mathbf{S} \mathbf{w} \quad (2.28)$$

This effectively modifies the system degree equations of motion to be

$$\dot{\mathbf{a}} \rightarrow \dot{\mathbf{a}} - \left( \mathbf{C}_-^\dagger \mathbf{S} \mathbf{w} - \mathbf{C}_+^T \mathbf{S}^* \mathbf{w}^* \right), \quad (2.29)$$

which is formally equivalent to simply displacing the noise fields  $\mathbf{b} \rightarrow \mathbf{b} + \mathbf{w}$  as one might have expected. As we will later see, the coupling vector for our concrete system model consists only of annihilation operators. Therefore, we will from now on set  $\mathbf{C}_+ = \mathbf{O}$ .

## 2.3 Dynamic and steady state properties of the system

Since our system is linear we can explicitly solve for the time dependence of the internal and external degrees of freedom

$$\check{\mathbf{a}}(t) = e^{t\mathbf{A}}\check{\mathbf{a}}(0) + e^{t\mathbf{A}} \int_0^t dt' e^{-t'\mathbf{A}} \mathbf{B}\check{\mathbf{b}}(t') \quad (2.30)$$

$$\check{\mathbf{b}}'(t) = \mathbf{C}e^{t\mathbf{A}} \int_0^t dt' e^{-t'\mathbf{A}} \mathbf{B}\check{\mathbf{b}}(t') + \mathbf{D}\check{\mathbf{b}}(t) + \mathbf{C}e^{t\mathbf{A}}\check{\mathbf{a}}(0) \quad (2.31)$$

If the system is Hurwitz-stable [32] the contributions from the internal degrees of freedom's initial state decay exponentially. Following [33] we can also define the Laplace-transforms as

$$\check{\mathbf{a}}[s] \equiv \int_0^\infty e^{-st} \check{\mathbf{a}}(t) dt \quad (2.32)$$

$$\check{\mathbf{b}}[s] \equiv \int_0^\infty e^{-st} \check{\mathbf{b}}(t) dt \quad (2.33)$$

$$\check{\mathbf{b}}'[s] \equiv \int_0^\infty e^{-st} \check{\mathbf{b}}'(t) dt. \quad (2.34)$$

This allows us to write down a transfer function for the external fields, where we ignore the contribution from the initial internal state

$$\check{\mathbf{b}}'[s] = \mathbf{\Xi}(s)\check{\mathbf{b}}[s] + \mathbf{C}(s - \mathbf{A})^{-1}\check{\mathbf{a}}(0) \quad (2.35)$$

$$\approx \mathbf{\Xi}(s)\check{\mathbf{b}}[s] \quad (2.36)$$

where the transfer function is easily obtained as

$$\mathbf{\Xi}(s) = [\mathbf{D} + \mathbf{C}(s\mathbf{1}_{2N} - \mathbf{A})^{-1}\mathbf{B}] \quad (2.37)$$

$$= [\mathbf{1}_{2M} - \mathbf{C}(s\mathbf{1}_{2N} - \mathbf{A})^{-1}\mathbf{C}^\dagger] \check{\Delta}(\mathbf{S}, \mathbf{0}) \quad (2.38)$$

If we also define the Fourier transformed fields as

$$\tilde{\mathbf{b}}(\omega) \equiv \frac{1}{\sqrt{2\pi}} \int_{-\infty}^{\infty} e^{i\omega t} \check{\mathbf{b}}(t) dt \quad (2.39)$$

$$\tilde{\mathbf{b}}'(\omega) \equiv \frac{1}{\sqrt{2\pi}} \int_{-\infty}^{\infty} e^{i\omega t} \check{\mathbf{b}}'(t) dt \quad (2.40)$$

$$(2.41)$$

then it turns out that the Laplace representation transfer function can be extended to complex  $s = -i\omega$  parameters

$$\tilde{\mathbf{b}}'(\omega) = \Xi(-i\omega) \tilde{\mathbf{b}}(\omega), \quad (2.42)$$

which implies that

$$\tilde{\mathbf{b}}'(\omega) = \mathbf{G}(\omega) \tilde{\mathbf{b}}(\omega) + \mathbf{g}(\omega) \tilde{\mathbf{b}}(-\omega)^*, \quad (2.43)$$

where the gain matrices are given by the upper two blocks of the transfer function matrix  $\Xi(-i\omega)$ . Note that this frequency-domain transfer function is of the form

$$\Xi(-i\omega) = \begin{pmatrix} \mathbf{g}(\omega) & \mathbf{G}(\omega) \\ \mathbf{G}^*(-\omega) & \mathbf{g}^*(-\omega) \end{pmatrix}. \quad (2.44)$$

The negative frequency of the adjoint field operators is due to the fact that

$$\frac{1}{\sqrt{2\pi}} \int_{-\infty}^{\infty} e^{i\omega t} \mathbf{b}^*(t) dt = \frac{1}{\sqrt{2\pi}} \left( \int_{-\infty}^{\infty} e^{-i\omega t} \mathbf{b}(t) dt \right)^* = \tilde{\mathbf{b}}(-\omega)^*, \quad (2.45)$$

and thus:

$$\tilde{\mathbf{b}}(\omega) = \begin{pmatrix} \tilde{\mathbf{b}}(\omega) \\ \tilde{\mathbf{b}}(-\omega)^* \end{pmatrix} \quad (2.46)$$



## 2.4 The squeezing spectrum

Squeezing is a phenomenon in which the uncertainty or the variance in one field quadrature is decreased at the cost of adding uncertainty to the orthogonal quadrature. The optical parametric oscillator can produce squeezed states of light. If we now define a output quadrature operator for a specific port  $j$  as

$$X_j^\theta(t) = e^{i\theta}b'_j(t) + e^{-i\theta}b'^{\dagger}_j(t), \quad (2.47)$$

$$\Leftrightarrow \tilde{X}_j^\theta(\omega) = e^{i\theta}\tilde{b}'_j(\omega) + e^{-i\theta}\tilde{b}'^\dagger_j(-\omega), \quad (2.48)$$

then it is possible to use the transfer functions above to derive an expression for the power spectral density of the output fields:

$$\mathcal{P}_j^\theta(\omega) = \lim_{T \rightarrow \infty} \frac{1}{T} \left\langle \int_0^T e^{i\omega t} X_j^\theta(t) dt \int_0^T e^{-i\omega t'} X_j^\theta(t') dt' \right\rangle, \quad (2.49)$$

which can be shown to be implicitly given by

$$\langle \tilde{X}_j^\theta(\omega) \tilde{X}_j^\theta(\omega') \rangle = \mathcal{P}_j^\theta(\omega) \delta(\omega + \omega') \quad (2.50)$$

Using the above results, it takes on the following form for vacuum inputs [33]:

$$\mathcal{P}_j(\omega, \theta) = 1 + \mathcal{N}_j(-\omega) + \mathcal{N}_j(\omega) + e^{-2i\theta} \mathcal{M}_j(\omega) + e^{2i\theta} \mathcal{M}_j(\omega)^*, \quad (2.51)$$

$$\text{where } \mathcal{N}_j(\omega) \equiv (\mathbf{g}(\omega) \mathbf{g}(\omega)^\dagger)_{jj}, \quad (2.52)$$

$$\mathcal{M}_j(\omega) \equiv (\mathbf{G}(\omega) \mathbf{g}(-\omega)^T)_{jj} \quad (2.53)$$

Constant coherent inputs to the system  $\mathbf{w} \in \mathbb{C}^M$  will only affect the squeezing spectrum at DC by adding a  $\delta$  peak with an amplitude depending on the coherent input amplitudes. This corresponds to the transformation

$$\check{\mathbf{b}}(t) \rightarrow \check{\mathbf{b}}(t) + \check{\mathbf{w}} \quad (2.54)$$

or in Fourier-Space

$$\tilde{\mathbf{b}}(\omega) \rightarrow \tilde{\mathbf{b}}(\omega) + \check{\mathbf{w}}\delta(\omega) \quad (2.55)$$

$$(2.56)$$

and consequently

$$\tilde{\mathbf{b}}'(\omega) \rightarrow \tilde{\mathbf{b}}'(\omega) + \Xi(-i\omega)\check{\mathbf{w}}\delta(\omega) \quad (2.57)$$

$$= \tilde{\mathbf{b}}'(\omega) + \Xi(0)\check{\mathbf{w}}\delta(\omega) = \tilde{\mathbf{b}}'(\omega) + \check{\Delta}(\mathbf{G}(0), \mathbf{g}(0))\check{\mathbf{w}}\delta(\omega) \quad (2.58)$$

Therefore, the  $\theta$ -quadrature of the  $j$ -th output field is shifted as

$$\tilde{X}_j^\theta(\omega) \rightarrow \tilde{X}_j^\theta(\omega) + e^{-i\theta} (\Xi(0)\check{\mathbf{w}})_j \delta(\omega) \quad (2.59)$$

$$+ e^{i\theta} (\Xi(0)\check{\mathbf{w}})_{j+M} \delta(\omega) \quad (2.60)$$

$$= \tilde{X}_j^\theta(\omega) + v_j(\theta, \mathbf{w}, \mathbf{w}^*)\delta(\omega) \quad (2.61)$$

And thus the power spectral density receives an additional DC contribution:

$$S_\theta(\omega) \rightarrow S_\theta(\omega) + v_j^2(\theta, \mathbf{w}, \mathbf{w}^*)\delta(\omega) \quad (2.62)$$

The generalization to a time dependent coherent field is possible as well.

## 2.5 System variables

Regarding the expectations of system variables, we remind ourselves that all the above results are only valid if the system is stable, which is the case whenever  $\mathbf{A}$  is Hurwitz-stable, i.e., all eigenvalues have strictly negative real part. From the previous section we know that the expected output field amplitude in the presence of constant coherent input fields  $\mathbf{w}$  is given by

$$\langle \check{\mathbf{b}}' \rangle_{\text{ss}} = \Xi(0)\check{\mathbf{w}} = [\mathbf{D} - \mathbf{CA}^{-1}\mathbf{B}] \check{\mathbf{w}}. \quad (2.63)$$

The expectation value of the internal mode operators is given by

$$\langle \check{\mathbf{a}} \rangle_{\text{ss}} = -\mathbf{A}^{-1} \mathbf{B} \check{\mathbf{w}}. \quad (2.64)$$

The intra-cavity photon number expectations can be obtained from the diagonal elements of

$$\mathbf{N} \equiv \langle \check{\mathbf{a}} \check{\mathbf{a}}^\dagger \rangle \quad (2.65)$$

which obeys an ODE that can be derived via the Ito-rules for the input fields. The fields in turn are completely specified through the  $\mathbf{F}$  matrix, which is implicitly defined via

$$\mathbf{F} dt \equiv d\check{\mathbf{B}} d\check{\mathbf{B}}^\dagger, \quad (2.66)$$

and for pure vacuum inputs we have

$$\mathbf{F}_{\text{vac}} = \begin{pmatrix} \mathbf{1}_M & \mathbf{0} \\ \mathbf{0} & \mathbf{0} \end{pmatrix}, \quad (2.67)$$

while for input fields in different thermal states characterized by a mean photon number  $n_1, n_2, \dots, n_M$ , we would have

$$\mathbf{F}_{\text{therm}} = \begin{pmatrix} \text{diag}(1 + n_1, 1 + n_2, \dots, 1 + n_M) & \mathbf{0} \\ \mathbf{0} & \text{diag}(n_1, n_2, \dots, n_M) \end{pmatrix}, \quad (2.68)$$

where the vacuum case is recovered for  $n_1 = n_2 = \dots = n_M = 0$ . This leads to:

$$\dot{\mathbf{N}} = \mathbf{A} \mathbf{N} + \mathbf{N} \mathbf{A}^\dagger \quad (2.69)$$

$$+ \mathbf{B} \check{\mathbf{w}} \langle \check{\mathbf{a}}^\dagger \rangle + \langle \check{\mathbf{a}} \rangle \check{\mathbf{w}}^\dagger \mathbf{B}^\dagger + \mathbf{B} \mathbf{F} \mathbf{B}^\dagger \quad (2.70)$$

In steady state we can replace  $\langle \tilde{\mathbf{a}} \rangle$  with its steady-state value (cf. Equation (2.64)), which leads to the following Lyapunov equation

$$\mathbf{0} = \mathbf{A}\mathbf{N}_{ss} + \mathbf{N}_{ss}\mathbf{A}^\dagger - \mathbf{B}\check{\mathbf{w}}\check{\mathbf{w}}^\dagger\mathbf{B}^\dagger\mathbf{A}^{\dagger-1} - \mathbf{A}^{-1}\mathbf{B}\check{\mathbf{w}}\check{\mathbf{w}}^\dagger\mathbf{B}^\dagger + \mathbf{B}\mathbf{F}\mathbf{B}^\dagger \quad (2.71)$$

$$= \mathbf{A}(\mathbf{N}_{ss} - \mathbf{N}_w) + (\mathbf{N}_{ss} - \mathbf{N}_w)\mathbf{A}^\dagger + \mathbf{Q}, \quad (2.72)$$

where we have introduced the constant matrices:

$$\mathbf{Q} = \mathbf{B}\mathbf{F}\mathbf{B}^\dagger \quad (2.73)$$

$$\mathbf{N}_w = \mathbf{A}^{-1}\mathbf{B}\check{\mathbf{w}}\check{\mathbf{w}}^\dagger\mathbf{B}^\dagger\mathbf{A}^{\dagger-1} = \langle \check{\mathbf{a}} \rangle_{ss} \langle \check{\mathbf{a}}^\dagger \rangle_{ss} \quad (2.74)$$

This quite intuitive result shows that a non-zero coherent input field simply leads to an additive contribution  $\mathbf{N}_w$  to the second order moments. Also note that if both  $\mathbf{\Omega}_+$  and  $\mathbf{C}_+$  are zero, the Lyapunov equation decouples and one can instead solve an analogous equation for the matrix  $\langle \mathbf{a}^\dagger \mathbf{a} \rangle$  instead.

## 2.6 Output power

For an SLH model with the ABCD matrices defined as above and with coherent inputs  $(\mathbf{S}, \mathbf{L}, H) \triangleleft (\mathbf{1}, \mathbf{w}, 0)$  the expected output power  $P_j$  from port  $j$  is implicitly given by the expectation value of the corresponding gauge process increment  $P_j dt = \langle d\Lambda'_{jj} \rangle$ . This expectation is given by

$$P_j dt = \left\langle \frac{(\mathbf{S}^* d\mathbf{\Lambda} \mathbf{S}^T)_{jj}}{dt} \right\rangle + \left\langle L_j^\dagger L_j \right\rangle dt \quad (2.75)$$

$$= (\mathbf{D}(\mathbf{F} + \check{\mathbf{w}}\check{\mathbf{w}}^\dagger)\mathbf{D}^\dagger)_{M+j, M+j} dt + (\mathbf{C}\mathbf{N}\mathbf{C}^\dagger)_{M+j, M+j} dt \quad (2.76)$$

$$+ (\mathbf{D}\check{\mathbf{w}}\langle \check{\mathbf{a}}^\dagger \rangle \mathbf{C}^\dagger)_{M+j, M+j} dt + (\mathbf{C}\langle \check{\mathbf{a}} \rangle \check{\mathbf{w}}^\dagger \mathbf{D}^\dagger)_{M+j, M+j} dt \quad (2.77)$$

In steady state, we can again replace the amplitude expectation and we find

$$\mathbf{D}\check{\mathbf{w}}\langle \check{\mathbf{a}}^\dagger \rangle_{ss} \mathbf{C}^\dagger + \mathbf{C}\langle \check{\mathbf{a}} \rangle_{ss} \check{\mathbf{w}}^\dagger \mathbf{D}^\dagger = \mathbf{D}\check{\mathbf{w}}\check{\mathbf{w}}^\dagger \mathbf{B}^\dagger \mathbf{A}^{\dagger-1} \mathbf{C}^\dagger - \mathbf{C}\mathbf{A}^{-1} \mathbf{B}\check{\mathbf{w}}\check{\mathbf{w}}^\dagger \mathbf{D}^\dagger \quad (2.78)$$

We can also split apart the internal second order moments as above  $\mathbf{N}_{ss} = (\mathbf{N}_{ss} - \mathbf{N}_w) + \mathbf{N}_w$ , where the first part is computed via a Lyapunov equation and the second part is given by a simple expression featuring only the input displacement and the model matrices. With this, we find

$$P_j = (\mathbf{D}\mathbf{F}\mathbf{D}^\dagger)_{M+j,M+j} + (\mathbf{C}(\mathbf{N}_{ss} - \mathbf{N}_w)\mathbf{C}^\dagger)_{M+j,M+j} + (\mathbf{\Xi}(0)\check{\mathbf{w}}\check{\mathbf{w}}^\dagger\mathbf{\Xi}(0)^\dagger)_{M+j,M+j} \quad (2.79)$$

In this form, the first two contributions are the combined (squeezed) vacuum/thermal photon number contributions while the last part is the only contribution due to the coherent input amplitude.

## 2.7 The linear optical parametric oscillator model

Finally, we discuss a concrete physical model that is central to this work: An OPO cavity consists of an optical resonator (in our case a bowtie cavity) with a PPLN crystal that couples a narrow-linewidth pump beam at a frequency  $2\omega$  to electromagnetic modes of lower frequencies via three-wave mixing. Generally, this enables the scattering of a single pump photon into two other photons with frequencies  $\omega_1, \omega_2$  that sum up to the original  $2\omega$  to satisfy conservation of energy. In the special case of degenerate three-wave mixing, the final photons have the same energy  $\omega_1 = \omega_2$ , this is the case for the OPOs considered here. In the following we refer to the cavity mode with frequency  $\omega$  as the *signal mode* to distinguish it from the pump.

The cavity is chosen such that it has a fairly narrow linewidth (on the order of tens of MHz) for the signal mode, whereas it is *much* larger for the pump. In fact the mirror transmissivity for the pump wavelength is so large that it is not technically well-defined to speak of a single pump mode in the cavity, but it will nonetheless turn out to be useful to model it that way later on. There exists a threshold for the pump input power at which the roundtrip power gain in the signal mode due to pump  $\rightarrow$  signal photon conversion becomes equal to the roundtrip power loss through the cavity mirrors. Above this threshold, the system starts lasing at the signal mode

frequency. For the most part, we assume that we are operating in a sub-threshold parameter regime where the pump beam amplitude is practically unaffected by the signal mode. We can then neglect the dynamics of the pump entirely. As we will see this leads to a quadratic Hamiltonian in the signal mode operators and thus to linear equations of motion.

$$\mathbf{S} = \mathbf{1}_3 \quad (2.80)$$

$$\mathbf{L} = \begin{pmatrix} \sqrt{\kappa_1}a + \alpha \\ \sqrt{\kappa_2}a \\ \sqrt{\kappa_L}a \end{pmatrix} \quad (2.81)$$

$$H = \Delta a^\dagger a + \frac{1}{2i} (\epsilon^* a^2 - \epsilon a^{\dagger 2}) + \frac{\sqrt{\kappa_1}}{2i} (\alpha a^\dagger - \alpha^* a) \quad (2.82)$$

In this case we find the following Ito QSDE for the signal mode operators

$$\dot{a} = -(\kappa_T/2 + i\Delta)a + \epsilon a^\dagger - \sqrt{\kappa_1}\alpha - \sqrt{\kappa_1}dA_1 - \sqrt{\kappa_2}dA_2 - \sqrt{\kappa_L}dA_L \quad (2.83)$$

$$\dot{a}^\dagger = -(\kappa_T/2 - i\Delta)a^\dagger + \epsilon^* a - \sqrt{\kappa_1}\alpha^* - \sqrt{\kappa_1}dA_1^\dagger - \sqrt{\kappa_2}dA_2^\dagger - \sqrt{\kappa_L}dA_L^\dagger \quad (2.84)$$

or writing the QSDE in vectorized form

$$\begin{pmatrix} da \\ da^\dagger \end{pmatrix} = \begin{pmatrix} -(\kappa_T/2 + i\Delta) & \epsilon \\ \epsilon^* & -(\kappa_T/2 - i\Delta) \end{pmatrix} \begin{pmatrix} a \\ a^\dagger \end{pmatrix} dt \quad (2.85)$$

$$+ \begin{pmatrix} -\sqrt{\kappa_1} & -\sqrt{\kappa_2} & -\sqrt{\kappa_T} & 0 & 0 & 0 \\ 0 & 0 & 0 & -\sqrt{\kappa_1} & -\sqrt{\kappa_2} & -\sqrt{\kappa_T} \end{pmatrix} \begin{pmatrix} dA_1 + \alpha dt \\ dA_2 \\ dA_3 \\ dA_1^\dagger + \alpha^* dt \\ dA_2^\dagger \\ dA_3^\dagger \end{pmatrix} \quad (2.86)$$

$$= \mathbf{A}\check{\mathbf{a}}dt + \mathbf{B}(\check{\mathbf{d}}\mathbf{A} + \check{\mathbf{w}}dt) \quad (2.87)$$

It can be formally solved as

$$\check{\mathbf{a}} = e^{t\mathbf{A}}\check{\mathbf{a}}_0 + (e^{t\mathbf{A}} - \mathbf{1}_2) \mathbf{A}^{-1}\mathbf{B}\check{\mathbf{w}} + \int_0^t e^{(t-t')\mathbf{A}}\mathbf{B}\check{\mathbf{d}}\check{\mathbf{A}}_{t'} dt' \quad (2.88)$$

The eigenvalues of  $\mathbf{A}$  are given by  $\lambda_{\pm} = -\kappa_T/2 \pm \sqrt{|\epsilon|^2 - \Delta^2}$ , so the linearized system is stable for

$$\kappa_T > 2|\epsilon|, \quad (2.89)$$

where we have set  $\Delta = 0$ , because above threshold the system can spontaneously start lasing at the shifted cavity frequency, i.e. the single-mode approximation may be invalidated. In steady state, the signal mode amplitude is given by

$$\langle \check{\mathbf{a}} \rangle_{\text{ss}} = -\mathbf{A}^{-1}\mathbf{B}\check{\mathbf{w}} = \begin{pmatrix} \frac{2\sqrt{\kappa_1}(2i\alpha\Delta - 2\epsilon\alpha^* - \alpha\kappa_T)}{4\Delta^2 - 4|\epsilon|^2 + \kappa_T^2} \\ -\frac{2\sqrt{\kappa_1}(2\alpha\epsilon^* + \alpha^*(2i\Delta + \kappa_T))}{4\Delta^2 - 4|\epsilon|^2 + \kappa_T^2} \end{pmatrix} \quad (2.90)$$

On resonance and for  $\alpha \in \mathbb{R}$  (which we are free to fix since only relative phases matter) we find

$$\langle \mathbf{a} \rangle_{\text{ss}, \alpha \in \mathbb{R}, \Delta=0} = \begin{pmatrix} \frac{-2\sqrt{\kappa_1}\alpha(2\epsilon + \kappa_T)}{\kappa_T^2 - 4|\epsilon|^2} \\ \frac{-2\sqrt{\kappa_1}\alpha(2\epsilon^* + \kappa_T)}{\kappa_T^2 - 4|\epsilon|^2} \end{pmatrix} \quad (2.91)$$

As a function of the pump phase, the amplitude is maximized (minimized) in magnitude when  $\epsilon \in \mathbb{R}$  and  $\epsilon > 0$  ( $\epsilon < 0$ ). In this case, the pump leads to a linear amplification or deamplification by a factor of  $\frac{\kappa_T}{\kappa_T - 2\epsilon}$  with respect to the case without pump.

## 2.8 Steady state photon number

For a coherently displaced, thermal input to the first port with coherent amplitude  $\alpha$  and thermal variance coefficient  $k_n$  (note that setting  $k_n$  simply corresponds to only

sending in a coherent input), the steady state photon number of the OPO is given by

$$\langle a^\dagger a \rangle_{\text{ss}} = \frac{k_n \kappa_1 (\kappa_1 + \kappa_2 + \kappa_3) + 2|\epsilon|^2}{(\kappa_1 + \kappa_2 + \kappa_3)^2 - 4|\epsilon|^2} \quad (2.92)$$

$$+ \frac{4\alpha^2 \kappa_1 |2i\Delta + 2\epsilon + \kappa_1 + \kappa_2 + \kappa_3|^2}{(4\Delta^2 + (\kappa_1 + \kappa_2 + \kappa_3)^2)^2 + 16|\epsilon|^4 + 8|\epsilon|^2 (4\Delta^2 - (\kappa_1 + \kappa_2 + \kappa_3)^2)} \quad (2.93)$$

We can already see from this that the thermal noise contribution is independent of the detuning, which is an intuitive result, since the thermal noise is broadband. On resonance  $\Delta = 0$  and for real  $\epsilon$  (pump 180° out of phase with input) this simplifies to

$$\langle a^\dagger a \rangle_{\text{ss}, \alpha \in \mathbb{R}, \Delta=0, \epsilon=\pm|\epsilon|} = \frac{k_n \kappa_1 (\kappa_1 + \kappa_2 + \kappa_3) + 2\epsilon^2}{(\kappa_1 + \kappa_2 + \kappa_3)^2 - 4\epsilon^2} + \frac{4\alpha^2 \kappa_1}{((\kappa_1 + \kappa_2 + \kappa_3) - 2\epsilon)^2}, \quad (2.94)$$

We see from this that a non-zero pump amplitude will always increase the thermal noise photon contribution, whereas it can reduce the photon number due to a coherent input, depending on the relative phase of  $\epsilon$  with the external driving. For  $\alpha, \epsilon = 0$ , we retrieve the result of the open-loop empty cavity with thermal input [17, 18]

$$\langle a^\dagger a \rangle_{\text{ss}, \alpha=0, \Delta=0, \epsilon=0} = \frac{k_n \kappa_1}{\kappa_1 + \kappa_2 + \kappa_3} = \frac{k_n \kappa_1}{\kappa_T} \quad (2.95)$$

With trivial feedback from port  $2 \rightarrow 3$ , the total linewidth can be modified to [19]

$$\kappa_T(\phi) = \kappa_1 + |\sqrt{\kappa_3} + e^{i\phi} \sqrt{\kappa_2}|^2 \quad (2.96)$$

The roundtrip feedback phase, denoted as  $\phi$  for brevity in this chapter (and as  $\Phi_{\text{FB}}$  in Chapter 4) is critical in determining the effect of coherent feedback in the system.

## 2.9 Transmission spectrum/transfer function

We now turn to a brief discussion of the transmission spectrum in the special case of a single mirror  $\kappa_2 = \kappa_3 = 0$ ,  $\kappa_1 = \kappa$ . In this case the frequency domain transfer



functions  $\mathbf{G}(\omega)$  and  $\mathbf{g}(\omega)$  are given by

$$\mathbf{G}(\omega) = -\frac{\frac{\kappa^2}{4} + (\Delta + \omega)^2 + |\epsilon|^2}{(\frac{\kappa}{2} - i(\omega + \Delta))^2 - |\epsilon|^2} \quad (2.97)$$

$$\mathbf{g}(\omega) = -\frac{\epsilon\kappa}{(\frac{\kappa}{2} - i(\omega + \Delta))^2 - |\epsilon|^2} \quad (2.98)$$

If we take the above result and rescale  $\epsilon \rightarrow k\epsilon, \kappa \rightarrow k\kappa$  and take the  $k \rightarrow \infty$  limit, we find the static squeezer limit for the single port OPO:

$$b'(t) = -\cosh(r)b(t) - \frac{\epsilon}{|\epsilon|} \sinh(r)b^\dagger(t), \quad (2.99)$$

$$b'^\dagger(t) = -\cosh(r)b^\dagger(t) - \frac{\epsilon^*}{|\epsilon|} \sinh(r)b(t), \quad (2.100)$$

where the squeezing parameter is given by  $r = \log \frac{1 + \frac{2|\epsilon|}{\kappa}}{1 - \frac{2|\epsilon|}{\kappa}}$ . For  $\epsilon/\kappa \rightarrow 0$  we find  $r \rightarrow 0$  and we recover an adiabatically eliminated cavity model that acts on the scattered field by imparting a  $\pi$  phase shift. Furthermore, for  $|\epsilon| \rightarrow \kappa/2$  the squeezing parameter diverges logarithmically which suggests that close to threshold one may produce arbitrarily squeezed states.

## 2.10 Concrete OPO models for our setup

The actual setup consists of two OPO cavities in a mutual feedback configuration. We distinguish between a Plant cavity  $P$  and a controller cavity  $C$ . Light emanated from one of the Plant mirrors bounces off (and couples into) a controller mirror and is then fed back to a second Plant mirror. We neglect the time delay along the feedback path, but allow for an accumulated roundtrip phase  $\phi$ . After feedback, the light reflected from the second plant mirror passes into a homodyne detector  $D$ . We account for (linear) losses in the optical pathways and mirror couplings  $P \rightarrow C$ ,  $C \rightarrow P$  and  $P \rightarrow D$  as well as the intra-cavity losses due to the mirrors and losses in the PPLN crystals.

The bare plant model  $P = (\mathbf{S}_P, \mathbf{L}_P, H_P)$

$$\mathbf{S}_P = \mathbf{1}_5 \quad (2.101)$$

$$\mathbf{L}_P = \begin{pmatrix} \sqrt{\gamma_1}a \\ \sqrt{\gamma_2}a \\ \sqrt{\gamma_3}a \\ \sqrt{\gamma_4}a \\ \sqrt{\gamma_L}a \end{pmatrix} \quad (2.102)$$

$$H_P = \Delta a^\dagger a + \frac{1}{2i} (\epsilon^* a^2 - \epsilon a^{\dagger 2}) \quad (2.103)$$

The bare controller model  $C = (\mathbf{S}_C, \mathbf{L}_C, H_C)$

$$\mathbf{S}_C = \mathbf{1}_2 \quad (2.104)$$

$$\mathbf{L}_C = \begin{pmatrix} \sqrt{\kappa}a \\ \sqrt{\kappa_L}a \end{pmatrix} \quad (2.105)$$

$$H_C = \delta b^\dagger b + \frac{1}{2i} (\eta^* b^2 - \eta b^{\dagger 2}) \quad (2.106)$$

Due to the trivial scattering matrices we can decompose both models into concatenations of single port SLH models for each port  $P = \boxplus_{j=1}^5 P_j$ ,  $C = C_1 \boxplus C_2$ , where we can include the Hamiltonian with any one of them.

The network model we now wish to consider is as follows: The beam emitted from the first mirror of  $P$  is fed into the first mirror of  $C$  after it is attenuated by linear loss  $L_1$ . The beam reflected off this first controller mirror is then fed back to the second port of  $P$  after it is attenuated by a second linear loss  $L_2$ . Finally, the light reflected off the second plant mirror is detected in a homodyne detector after it undergoes a third linear loss  $L_3$ . The losses linear  $L_j$  can be modeled as beamsplitters, i.e., neglecting the counter-propagating fields, they have two inputs and two outputs. Without losses the simplified network expression is given by

$$(P_2 \triangleleft \phi \triangleleft C_1 \triangleleft P_1) \boxplus P_3 \boxplus P_4 \boxplus P_5 \boxplus C_2, \quad (2.107)$$

which is straightforward to understand. Including the losses clutters the expressions quite a bit. To better understand this, we visualize the lossless network in Figure 2.1 (decomposing  $P$  and  $C$  into concatenations allows us to convert the feedback into series products) and several equivalent (up to permutations of the ports) expressions for the lossy model are graphically represented in Figure 2.2.

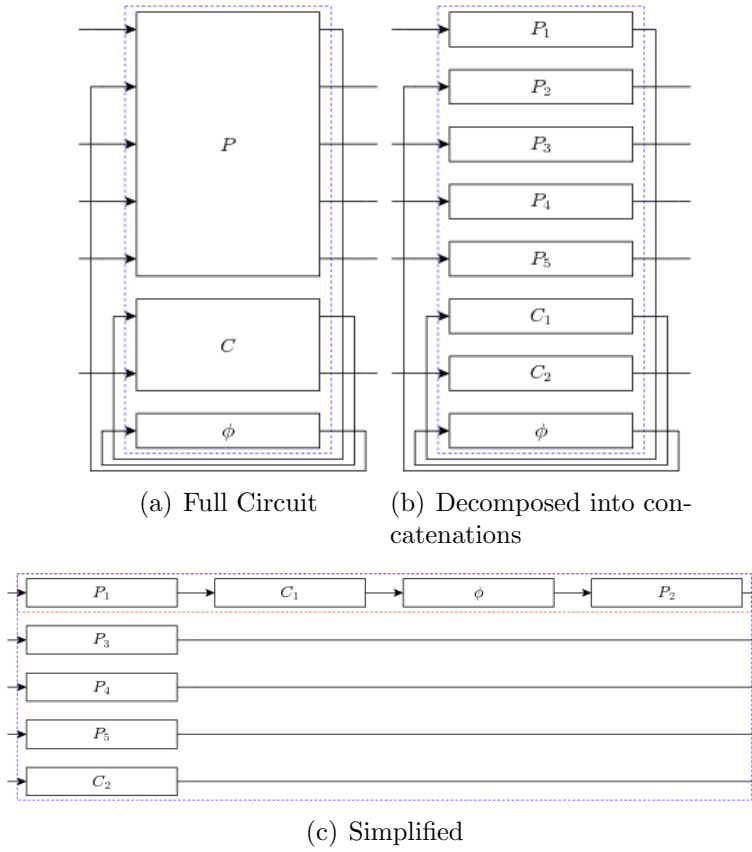


Figure 2.1: Equivalent ways to diagram the circuit expression

The parameters for the whole network are given by

$$\mathbf{S} = \begin{pmatrix} e^{i\phi} \sqrt{1-l_1} \sqrt{1-l_2} \sqrt{1-l_3} & -e^{i\phi} \sqrt{l_1} \sqrt{1-l_2} \sqrt{1-l_3} & -\sqrt{l_2} \sqrt{1-l_3} & -\sqrt{l_3} & 0 & 0 & 0 & 0 \\ e^{i\phi} \sqrt{l_3} \sqrt{1-l_1} \sqrt{1-l_2} & -e^{i\phi} \sqrt{l_1} \sqrt{l_3} \sqrt{1-l_2} & -\sqrt{l_2} \sqrt{l_3} & \sqrt{1-l_3} & 0 & 0 & 0 & 0 \\ e^{i\phi} \sqrt{l_2} \sqrt{1-l_1} & -e^{i\phi} \sqrt{l_1} \sqrt{l_2} & \sqrt{1-l_2} & 0 & 0 & 0 & 0 & 0 \\ \sqrt{l_1} & \sqrt{1-l_1} & 0 & 0 & 0 & 0 & 0 & 0 \\ 0 & 0 & 0 & 0 & 1 & 0 & 0 & 0 \\ 0 & 0 & 0 & 0 & 0 & 1 & 0 & 0 \\ 0 & 0 & 0 & 0 & 0 & 0 & 1 & 0 \\ 0 & 0 & 0 & 0 & 0 & 0 & 0 & 1 \end{pmatrix} \quad (2.108)$$

$$\mathbf{L} = \begin{pmatrix} (\sqrt{\gamma_1} \sqrt{1-l_1} \sqrt{1-l_2} \sqrt{1-l_3} e^{i\phi} + \sqrt{\gamma_2} \sqrt{1-l_3}) a + \sqrt{\kappa} \sqrt{1-l_2} \sqrt{1-l_3} e^{i\phi} b \\ (\sqrt{\gamma_1} \sqrt{l_3} \sqrt{1-l_1} \sqrt{1-l_2} e^{i\phi} + \sqrt{\gamma_2} \sqrt{l_3}) a + \sqrt{\kappa} \sqrt{l_3} \sqrt{1-l_2} e^{i\phi} b \\ \sqrt{\gamma_1} \sqrt{l_2} \sqrt{1-l_1} e^{i\phi} a + \sqrt{\kappa} \sqrt{l_2} e^{i\phi} b \\ \sqrt{\gamma_1} \sqrt{l_1} a \\ \sqrt{\gamma_3} a \\ \sqrt{\gamma_4} a \\ \sqrt{\gamma_L} a \\ \sqrt{\kappa_L} b \end{pmatrix} \quad (2.109)$$

$$H = \left( \Delta + \sqrt{\gamma_1 \gamma_2 (1-l_1)(1-l_2)} \sin(\phi) \right) a^\dagger a + \delta b^\dagger b \quad (2.110)$$

$$+ \frac{1}{2i} \left( \eta^* b^2 - \eta b^{\dagger 2} \right) + \frac{1}{2i} \left( \epsilon^* a^2 - \epsilon a^{\dagger 2} \right) \quad (2.111)$$

$$+ \frac{\sqrt{\kappa}}{2i} \left[ \left( \sqrt{\gamma_2 (1-l_2)} e^{i\phi} - \sqrt{\gamma_1 (1-l_1)} \right) a b^\dagger - \left( \sqrt{\gamma_2 (1-l_2)} e^{-i\phi} - \sqrt{\gamma_1 (1-l_1)} \right) a^\dagger b \right] \quad (2.112)$$

The physical parameters in our experiment are given in Table 2.1. Inspecting the Hamiltonian we see that the feedback achieves two things: It introduces a feedback phase dependent detuning of the Plant mode  $a$  and it couples the Plant and Controller modes with a coupling constant that also depends on the feedback roundtrip phase. The final Hamiltonian can be written as a quadratic form in the mode operators. We

Symbol	Value	Description
$\gamma_1$	$4 \times 4.5\text{MHz}/2\pi = 18\text{MHz}/2\pi$	Plant mirror 1 (start of feedback loop)
$\gamma_2$	$8 \times 4.5\text{MHz}/2\pi = 36\text{MHz}/2\pi$	Plant mirror 2 (end of feedback loop)
$\gamma_3$	$.34 \times 4.5\text{MHz}/2\pi \approx 2\text{MHz}/2\pi$	Plant mirror 3 (coherent input)
$\gamma_4$	$.1 \times 4.5\text{MHz}/2\pi \approx .45\text{MHz}/2\pi$	Plant mirror 4 (to photodetector for feedback lock)
$\gamma_L$	$1 \times 4.5\text{MHz}/2\pi \approx 4.5\text{MHz}/2\pi$	Combined additional Plant losses
$ \epsilon $	$\leq 4 \times 4.5\text{MHz}/2\pi = 18\text{MHz}/2\pi$	Plant pump power gain
$\Delta$	$\pm \text{a few MHz}$	Plant cavity detuning with respect to the external coherent driving
$\kappa$	$18.7 \times 4.5\text{MHz}/2\pi \approx 84\text{MHz}/2\pi$	Controller mirror (for feedback)
$\kappa_L$	$1 \times 4.5\text{MHz}/2\pi \approx 4.5\text{MHz}/2\pi$	Combined additional Controller losses
$ \eta $	$\leq 4 \times 4.5\text{MHz}/2\pi = 18\text{MHz}/2\pi$	Plant pump power gain
$\delta$	$\pm \text{a few MHz}$	Controller cavity detuning with respect to the external coherent driving
$\phi$	$0 - 2\pi$	Feedback roundtrip phase
$l_1$	5%	Power loss between Plant mirror 1 and Controller mirror
$l_2$	10%	Power loss between Controller mirror and Plant mirror 2
$l_3$	5%	Power loss between Plant mirror 2 and homodyne detector

Table 2.1: Physical model parameters

again use a doubled up notation for the mode operators  $\check{a} = \begin{pmatrix} a \\ b \\ a^\dagger \\ b^\dagger \end{pmatrix}$ .

$$H = \frac{1}{2} \check{a}^\dagger \mathbf{R} \check{a} + C, \quad \text{where } \mathbf{R} = \begin{pmatrix} \Delta(\phi) & g(\phi)^* & i\epsilon & 0 \\ g(\phi) & \delta & 0 & i\eta \\ -i\epsilon^* & 0 & \Delta(\phi) & g(\phi) \\ 0 & -i\eta^* & g(\phi)^* & \delta \end{pmatrix}, \quad (2.113)$$

$$\text{with } \Delta(\phi) \equiv \Delta + \sqrt{\gamma_1 \gamma_2 (1 - l_1)(1 - l_2)} \sin(\phi), \quad (2.114)$$

$$g(\phi) \equiv \frac{\sqrt{\kappa}}{2i} \left( \sqrt{\gamma_2 (1 - l_2)} e^{i\phi} - \sqrt{\gamma_1 (1 - l_1)} \right), \quad (2.115)$$

$$C = -\frac{\Delta(\phi) + \delta}{2} \in \mathbb{R} \quad (2.116)$$

Note that despite its hermiticity we cannot simply diagonalize  $\mathbf{R} = \mathbf{U}^\dagger \text{diag}(\lambda_1, \dots, \lambda_4) \mathbf{U}$  to obtain new uncoupled mode operators  $\check{a}' = \mathbf{U} \check{a}$ , because this will not automatically preserve the canonical commutation relations, i.e., in general we would find

$$[\check{a}', \check{a}'^\dagger] \neq [\check{a}, \check{a}^\dagger] = \begin{pmatrix} \mathbf{1}_2 & \mathbf{0} \\ \mathbf{0} & -\mathbf{1}_2 \end{pmatrix} \quad (2.117)$$

For details check [31, 28]. A special case, in which this *is* possible is in the absence of squeezing  $\eta = \epsilon = 0$ . In this case we have

$$H = \begin{pmatrix} a^\dagger & b^\dagger \end{pmatrix} \mathbf{\Omega}_- \begin{pmatrix} a & b \end{pmatrix}, \text{ where } \mathbf{\Omega}_- = \begin{pmatrix} \Delta(\phi) & g(\phi)^* \\ g(\phi) & \delta \end{pmatrix}, \quad (2.118)$$

we can rewrite  $\mathbf{\Omega}_-$  in terms of the Pauli matrices  $\mathbf{\Omega}_- = \frac{\Delta(\phi) + \delta}{2} + \vec{n} \cdot \vec{\sigma}$ , where  $\vec{n} = \left( \Re g(\phi) \quad \Im g(\phi) \quad \frac{\Delta(\phi) - \delta}{2} \right)^T$ . This implies that the spectrum is just given by

$$\lambda_{\pm} = \frac{\Delta(\phi) + \delta}{2} \pm \sqrt{|g(\phi)|^2 + \left( \frac{\Delta(\phi) - \delta}{2} \right)^2} \quad (2.119)$$

We see that regardless of the actual or feedback-imposed detuning, we get a mode splitting due to the coupling of the two cavity modes. When both cavities have the same (effective) center frequency  $\delta = \Delta(\phi)$  we have  $\lambda_+ - \lambda_- = 2|g(\phi)|$ . From the definition of  $g$  we see that this becomes maximal for  $\phi = \pi$ , in which case

$$|g(\pi)| = \frac{\sqrt{\kappa}}{2} \left( \sqrt{\gamma_1(1 - l_1)} + \sqrt{\gamma_2(1 - l_2)} \right) \quad (2.120)$$

With the physical parameters as given in Table 2.1 we can expect a maximum mode-splitting of about  $45\text{MHz}/2\pi \approx 7\text{MHz}$ . Finally, we give our model in the ABCD parametrization for later use. We know that the ABCD matrices can be expressed in



We know that  $\mathbf{C}^\dagger \mathbf{C} = \check{\Delta}(\mathbf{C}_-^\dagger \mathbf{C}_-, \mathbf{0})$ , where the non-trivial part is given by

$$\mathbf{C}_-^\dagger \mathbf{C}_- = \begin{pmatrix} \gamma_T + 2\sqrt{(1-l_1)(1-l_2)\gamma_1\gamma_2}\cos\phi & \sqrt{(1-l_1)\gamma_1\kappa} + e^{i\phi}\sqrt{(1-l_2)\gamma_2\kappa} \\ \sqrt{(1-l_1)\gamma_1\kappa} + e^{-i\phi}\sqrt{(1-l_2)\gamma_2\kappa} & \kappa_T \end{pmatrix}, \quad (2.130)$$

where  $\gamma_T = \gamma_1 + \gamma_2 + \gamma_3 + \gamma_4 + \gamma_L$  and  $\kappa_T = \kappa + \kappa_L$ . Therefore the system matrix is given by  $\mathbf{A} = \check{\Delta}(\tilde{\mathbf{A}}, -i\mathbf{\Omega}_+)$ , where

$$\tilde{\mathbf{A}} = \begin{pmatrix} -i\Delta - \frac{\gamma_T}{2} - \Gamma e^{-i\phi} & -\sqrt{\kappa\gamma_2(1-l_2)}e^{i\phi} \\ -\sqrt{\gamma_1\kappa(1-l_1)} & -i\delta - \frac{\kappa_T}{2} \end{pmatrix}, \quad (2.131)$$

$$-i\mathbf{\Omega}_+ = \begin{pmatrix} \epsilon & 0 \\ 0 & \eta \end{pmatrix}, \quad (2.132)$$

$$\Gamma = \sqrt{\gamma_1\gamma_2(1-l_1)(1-l_2)} \quad (2.133)$$

## 2.11 The setup as an LQG problem

Although the experimental results presented in Chapter 4 are strictly for the case of coherent inputs, here we continue to generalize to the inclusion of thermal (broad-band) inputs, which will be useful for comparison with previous work [17, 18] as well as future experiments. From the final form of the elements of the  $\mathbf{A}$  matrix we can see that the roundtrip phase  $\phi$  controls the phase of the inter-cavity mode coupling coefficients as well as the decay rate and the detuning of the plant cavity mode. This roundtrip phase is associated with the optical pathlength in the feedback loop. We also expect the Controller mirror itself to impart an additional phase shift on the beam and when we are pumping the Controller OPO, we expect a phase dependent attenuation or amplification of the roundtrip signal [17, 18]. We treat the Plant as a simple cavity by setting its pump parameter to zero, since we have seen in section 2.8 that the plant pump cannot help reject a thermal input. The input port is the second effective port after feedback, i.e. the one with coupling  $\gamma_3$ . The monitored output port is the next one with coupling  $\gamma_4$ .



We now discuss the different types of control possible in our setup, starting with the "trivial controller" where the beam only reflects off Controller input mirror. In this case, to make the discussion simpler, we some set losses to zero:  $\gamma_4 = \gamma_L = 0, l_1 = l_2 = l_3 = 0$ . The open loop Plant model then has two ports, but with the feedback it effectively becomes a single port system again. The ABCD model is then given by:

$$\mathbf{A}_{\text{tfb}} = \check{\Delta}(-\gamma_T/2 - \sqrt{\gamma_1\gamma_2}e^{i\phi}, 0) \quad (2.134)$$

$$\mathbf{B}_{\text{tfb}} = \check{\Delta} \left[ \begin{pmatrix} -\sqrt{\gamma_1} - \sqrt{\gamma_2}e^{i\phi} & -\sqrt{\gamma_3} & -\sqrt{\gamma_4} & -\sqrt{\gamma_L} \end{pmatrix}, \mathbf{0} \right] \quad (2.135)$$

$$\mathbf{C}_{\text{tfb}} = \check{\Delta} \left[ \begin{pmatrix} \sqrt{\gamma_1}e^{i\phi} + \sqrt{\gamma_2} \\ \sqrt{\gamma_3} \\ \sqrt{\gamma_4} \\ \sqrt{\gamma_L} \end{pmatrix}, \mathbf{0} \right] \quad (2.136)$$

$$\mathbf{D}_{\text{tfb}} = \check{\Delta} \left[ \begin{pmatrix} e^{i\phi} & 0 & 0 & 0 \\ 0 & 1 & 0 & 0 \\ 0 & 0 & 1 & 0 \\ 0 & 0 & 0 & 1 \end{pmatrix}, \mathbf{0} \right] \quad (2.137)$$

The trivial feedback effectively maps the five-port model to a four-port model with  $\phi$ -dependent couplings and detuning. As we have seen above, for a thermal input with noise coefficient  $k_n$ , the steady state photon number for  $\phi \in \{0, \pi\}$  is given by

$$\langle n \rangle_{\text{ss}}(\phi) = \frac{\gamma_3 k_n}{\gamma_T(\phi)}, \quad (2.138)$$

where  $\gamma_T(\phi) = \gamma_T + 2\sqrt{\gamma_1\gamma_2}\cos(\phi)$ .

Intuitively, the simple (empty) cavity controller should perform worse than trivial feedback controller because of the frequency dependent phase shift it imparts on the signal (see Chapter 4 for an additional discussion), and in fact this was confirmed in previous numerical studies [17, 18] when the cavity mirror reflectivities were left as variable parameters during controller optimization (i.e. the trivial feedback case was actually the optimal empty cavity controller!). The previous numerical work also considered the case of an infinite bandwidth OPO controller (i.e. static squeezer),

but the apparatus built and tested here is very much in the regime of a narrowband controller (relative to the noise bandwidth). As it turns out, the steady state photon number expressions are too complicated to be tractable for analytic analysis, and their numerical simulation remains an area for further research. Instead, having built the apparatus, we did a brief experiment (discussed in Chapter 4) and found that the narrowbandedness of the controller presents a significant limitation to its ability to reject broadband noise (however, the controller is effective for narrowband disturbances, which will be subject of the rest of the thesis).

At this juncture, I would also like to point out that a significant amount of work was done to investigate the effects on the squeezing spectra produced from the OPOs connected in the coherent feedback configuration, as well as the possibility of an emergent limit cycle behavior when the combined system is well above threshold. Although very germane to the area of coherent control engineering, this work will be presented elsewhere at a future date, hopefully in conjunction with some additional experimental results.

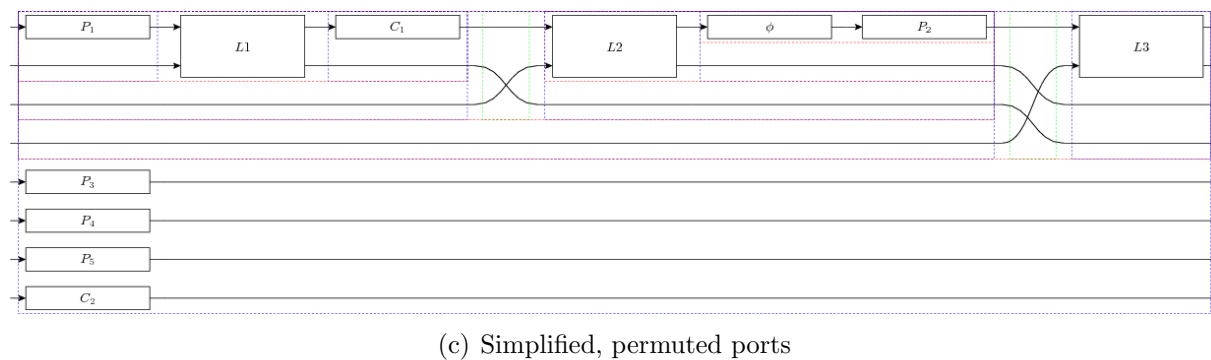
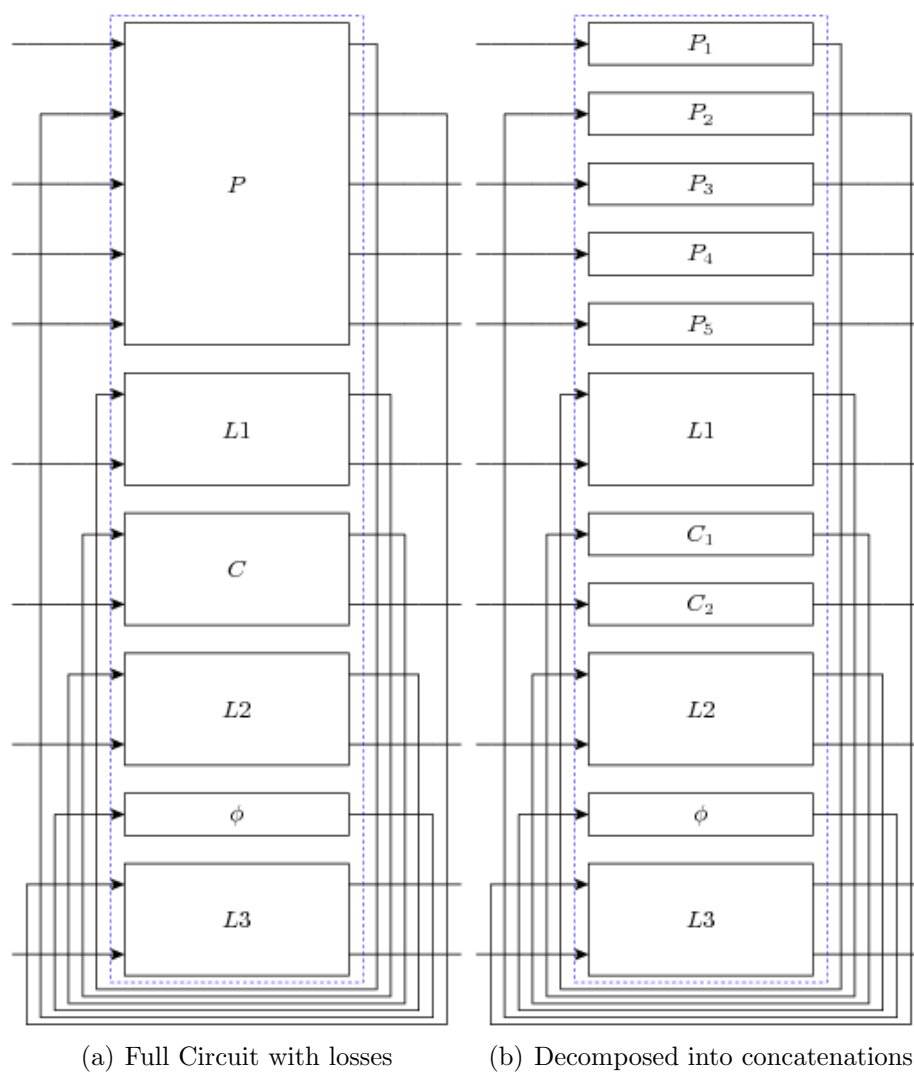


Figure 2.2: Simplification of the lossy circuit expression.

# Chapter 3

## Experimental Setup

In this Chapter we describe the experimental apparatus in depth, including its components, locking stabilization schemes, and operation (see fig. 3.1, which shows a functional diagram of the entire apparatus and approximate relative location of the components; we'll next proceed with a discussion of the individual subsystems before returning to it. Pictures of the apparatus can be found in fig. 3.2). Further information on the details regarding cavity design, electronics and nonlinear optical crystals can be found in the Appendices.

### 3.1 Master laser and beam generation

The master laser in the experiment from which all beams (signal, pump, locking and local oscillator) derive is an Mephisto MOPA from InnoLight (the laser will be henceforth referred to as the "MOPA") operating in CW mode at a wavelength of 1064.4 nm and a nominal output power of 10 W (see fig. 3.3). The laser is configured in a Master Oscillator Power Amplifier (MOPA) arrangement where the output of a spectrally narrow ( $\sim$  kHz linewidth) non-planar ring oscillator (NPRO) YAG laser is amplified by a pair of additional diode-pumped YAG crystals before output from the laser head; the nominal max power from the master oscillator is 1 W, and the amplifier crystals bring this up to 10 W. The output wavelength is set by the temperature of the master oscillator crystal, and care was chosen to set it to a nominal value to avoid

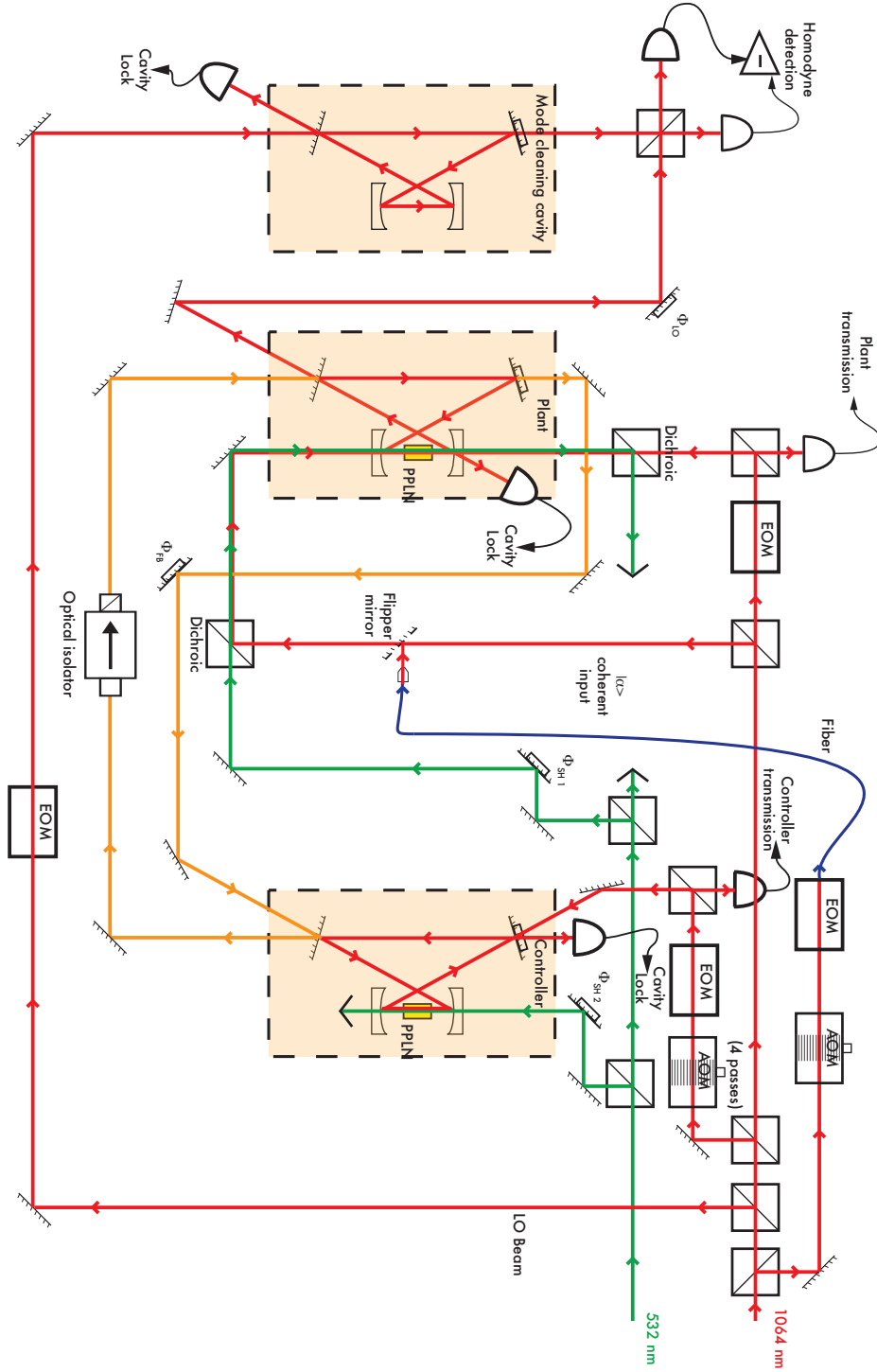


Figure 3.1: Functional diagram of entire apparatus, showing injection, feedback, pump and detection paths. Waveplates, modematching lenses and backwards beam diagnostic detectors omitted for clarity. Go Charles!

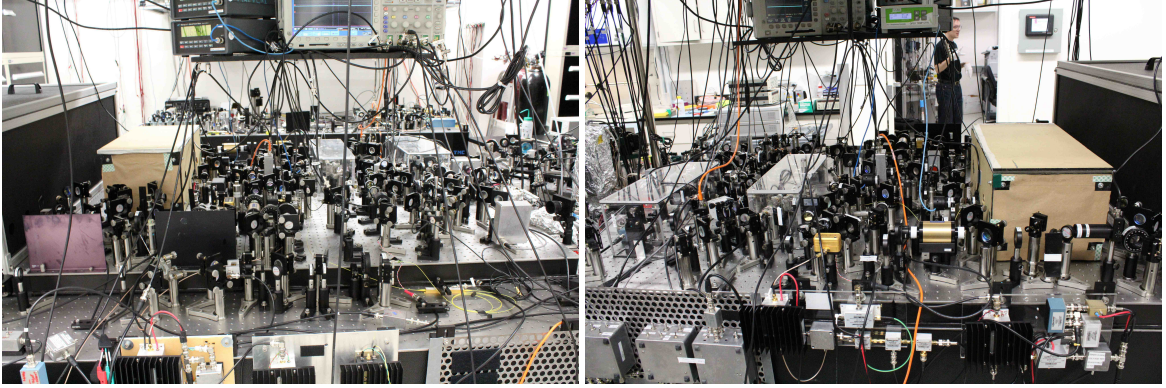


Figure 3.2: Front (left) and rear (right) views of the apparatus. Author makes cameo appearance. With respect to the diagram shown in fig. 3.1, the "front" corresponds to looking from the right of the diagram, while the "back" corresponds to looking from the left.

modehopping (the set value used in the experiment was  $24.53\text{ }^{\circ}\text{C}$ , and wavelength and stability monitored by fiber coupling part of the output beam into a Burleigh Wavemeter). Although it's certainly possible to run the laser at an output power of less than 10 W by reducing either the master oscillator or amplifier laser diode current, doing so significantly alters the output beam size (most likely due to spatial gain saturation in the amplifier crystals), and thus it's desirable to keep this constant to avoid changes in the beam parameters throughout the rest of the apparatus. The current in the master oscillator controller is set a little below the max output at 2.2 A, while the current is maxed out in the amplifier controller to  $\approx 43\text{ A}$ . The laser is water cooled by a ThermoCube recirculating water chiller rated to a thermal load of 400 W with a centrifugal pump, chosen to minimize flow induced vibrations while providing large enough flow rate to keep the MOPA from overheating. The coolant used is an 85% distilled water, 15% ethanol by volume mixture to prevent bacteria growth in the coolant lines, and the coolant set temperature is  $25.0\text{ }^{\circ}\text{C}$ . The interior of the MOPA head also requires dehumidification, and this is done by a desiccant cartridge screwed in to the center of the rear (fig. 3.3) that requires changing every 1 to 2 weeks or so. Even when the laser temperature and currents are properly stabilized by the controllers, a slow ( $\sim\text{ Hz}$  or less) drift in output power on the order of up to a % at times is present, and the laser also exhibits higher frequency relaxation



Figure 3.3: Front (left) and rear (right) of the MOPA, the master laser used in the experiment. Black desiccant cartridge visible at center of rear; center indicator is dark blue when the cartridge is fresh, exchange cartridge when it turns light purple.

oscillations at 700 kHz (readily visible by viewing part of the MOPA output on a spectrum analyzer via a detector with sufficient bandwidth). For the purposes of this experiment, the slow drifts aren't problematic, but they could be servo-ed out via the current modulation analog input port on the MOPA if necessary.

Unfortunately, unlike the beams of other comparable high power solid state lasers manufactured by other companies, the output beam of the MOPA is highly divergent and a pair of lenses are used to collimate the beam before it enters a high power optical isolator (IO-10-1064-VHP from Thorlabs). The initial lenses are tilted to avoid sending surface reflections of the beam back into the laser (at the expense of adding a small amount of ellipticity to it), and the isolator also serves as the "master" beam-splitter for the beams in the experiment: the main transmitted beam has  $\approx 9.1$  W of power and is used to pump the frequency doubling crystal (a 2 cm long magnesium oxide doped periodically poled lithium niobate (MgO:PPLN) crystal mounted in an oven, both from Covision), while the rejected beams are further split and used as the input to the system, for locking the cavities, and for the local oscillator in the homodyne detection setup discussed below (see fig. 3.4). The frequency doubling crystal generates the second harmonic pump beam at 532.2 nm, and this doubling method has the advantage in that it achieves automatic frequency locking between the signal (fundamental 1064.4 nm) beams and half the second harmonic beam frequency. If

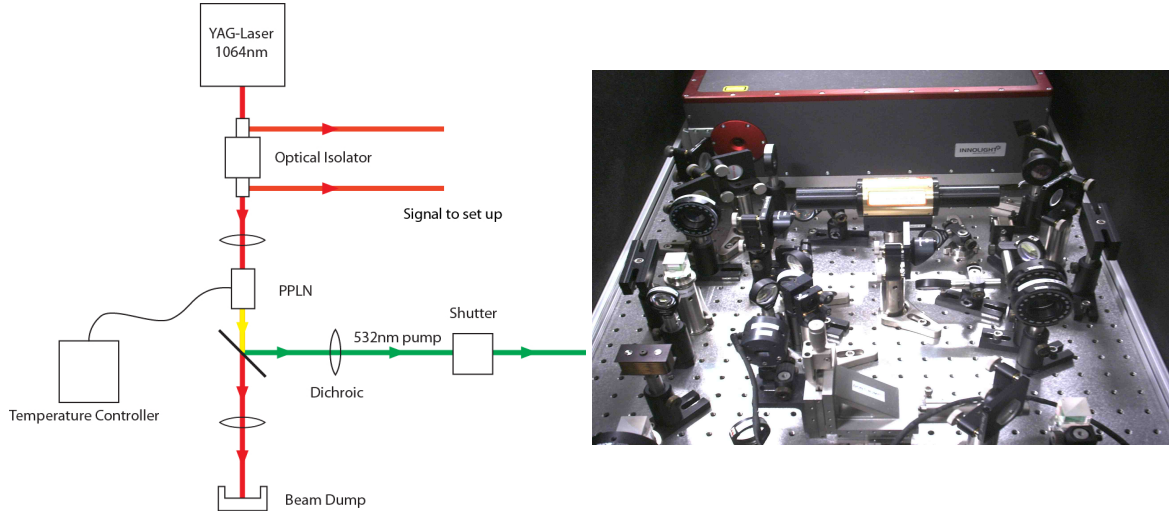


Figure 3.4: Diagram (left) and photograph (right) of the frequency doubling setup. The high power optical isolator (beige in color) also serves as the "master" beam splitter for the signal beams and the "pump" to generate the second harmonic beam (which is itself the "pump" for the OPOs as discussed below). The doubling crystal is housed inside the black oven mounted on the translation stage near the bottom of the picture.

a different laser (e.g. a Verdi from Coherent) were used as to pump the degenerate OPOs as described below, its frequency would also have to be locked to double the fundamental MOPA frequency, which would require yet another servo mechanism in the apparatus (as we discuss below, there are already a considerable number of these).

The doubling crystal itself contains 5 poled regions, each designed to phase match at a different temperature, and for a relatively weakly focused beam (spot size  $\sim 55 \mu\text{m}$ ) on a single pass through the crystal, the amount of second harmonic power generated by the main beam is ideally a little over 1 W for the higher temperature ( $\sim 60^\circ\text{C}$  and above) gratings (the details of this process, obtaining more power, and crystal issues are discussed in Appendix C; see fig. 3.5). The entire doubling setup is housed in a black plastic box (with a frame made of 80/20 material) to prevent stray light from the infrared and green beams from being a hazard to the people and equipment in the surrounding area, and an Oriel 76992 shutter (capable of withstanding up to 2 W CW power at 532 nm) is used to toggle the pump output from the box on and off. Throughout the apparatus, razorblade stack beam blocks



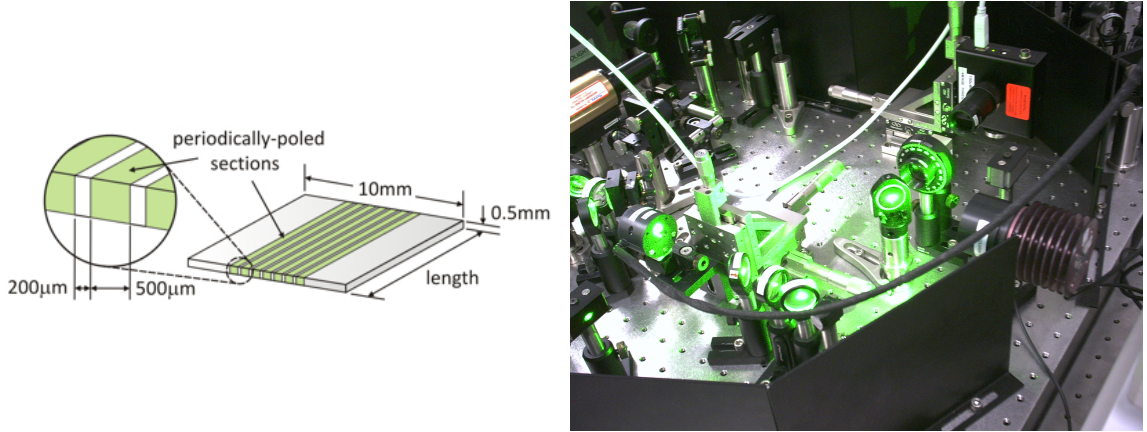


Figure 3.5: PPLN crystal schematic, showing the different poled regions (left). Photograph of the generation of the second harmonic pump beam, visible as a thin green line (right), with the power being measured by the Thorlabs PM50 thermal power meter.

(Thorlabs LB1) are used to block beams of 0.1 W or more in power, with care taken to make sure the beams aren't focusing onto the stacks.

## 3.2 OPO specs, pump coupling, and feedback loop

As mentioned in Chapter 1, the coherent feedback setup consists of a pair of degenerate OPOs, one nominally behaving as a "plant" (henceforth referred to as "OPO2") and one as a "controller" (henceforth referred to as "OPO1"; the number indicates the order in which they were built). Each OPO consists of a bowtie ring cavity of two curved and two flat mirrors, with a crystal identical to the doubling crystal (also housed in an identical oven) centered between the two curved mirrors (see figs. 3.6 and 3.7). NB: the reflectivities and transmissivities listed below are given in terms of % optical power. For OPO1, the mirrors are chosen such that only one of the mirrors (the input flat mirror, a 1 in. diameter YAG output coupler from VLOC) has relatively high transmission ( $\approx 18.5\%$ ), and the rest are high reflectors (the 7 mm diameter curved mirrors from PMS have reflectivities  $\sim 99.99\%$ , remaining 1 in. diameter flat from CVI Laser has a reflectivity of  $\approx 99.93\%$ ). This is done so that the amount of squeezing from this OPO approaches that for an ideal squeezer with

only a single input/output port, which is important for coherent cascade or feedback configurations that try to optimize the amount of squeezing (and although this is not strictly necessary for the measurements presented in the next Chapter, it makes the apparatus more suitable for exploring these directions in the near future). The loss per pass through the crystal at the fundamental wavelength is  $\sim 1\%$ , and most of this seems to be coming from back scattering off the crystal input and output facets (the crystals could use better AR coatings!) rather than absorption in the crystal, which actually causes some trouble with the cavity locking schemes as discussed below. For OPO2, two of the mirrors have relatively high transmission ( $\approx 8\%$  and  $\approx 4\%$  for 1 in. diameter flat output couplers from JouleOptik) to facilitate reasonable coupling to the coherent feedback path, while the curved mirrors have higher reflectivity, but not as high as those in OPO1 ( $\approx 99.66\%$  and  $\approx 99.90\%$  for 0.5 in. diameter mirrors from LayerTech and the Byer-Fejer group, respectively) to allow the injected coherent "disturbance" and locking beams to enter more easily. The curved mirrors have a radius of  $\approx 10$  cm to optimize the design size of the OPO and the coupling of the cavity mode to the crystal, as discussed in Appendix A. The angles of reflection in the bowtie cavities are chosen to be small to minimize the amount of astigmatism of the cavity modes, and the actual values measured by imaging the cavity outputs on a Spiricon beam imaging camera confirm the ellipticities of these beams to be small ( $\sim 5\%$ ). To accommodate these small angles and to avoid traversing the crystal more than once per cavity roundtrip (which would incur additional losses), the face of the Covision ovens that house the crystals is opened up and the bowtie path lies in a plane such that the paths between the flat mirrors and curved mirrors are both straight, but the former lies  $\sim 1$  cm above the other. When using the lowest temperature gratings ( $\sim 40^\circ$  and  $60^\circ\text{C}$ ) on the crystal, opening the oven faces does not significantly affect the temperature stability of the crystal. Both OPOs are surrounded by acrylic boxes to prevent air currents from causing substantial drift in the cavity length (but the boxes have small holes to let the beams through).

For each OPO, the dual-coated curved mirrors are highly transmissive at the pump wavelength ( $\approx 93\%$ ), to allow for good pump beam coupling to the crystal. For OPO1, the pump is directly coupled through the curved mirror along its own optical path,

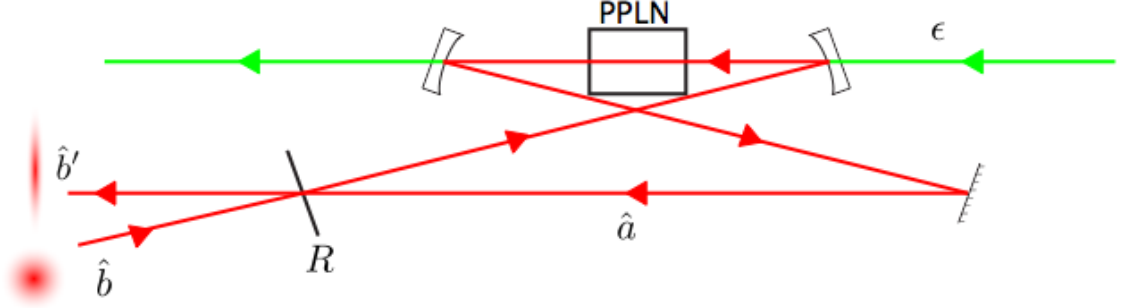


Figure 3.6: Degenerate OPO functional schematic. A coherent state  $\hat{b}$  is injected into one of the partially transmissive mirrors (reflectivity  $R$ ) and circulates in the cavity as mode  $\hat{a}$ , while interacting with the PPLN crystal being pumped by a second harmonic beam with coupling efficiency  $\epsilon$ . Due to the phase sensitive nature of the degenerate parametric interaction, the output field  $\hat{b}'$  is squeezed along a direction determined by the phase of the pump beam.

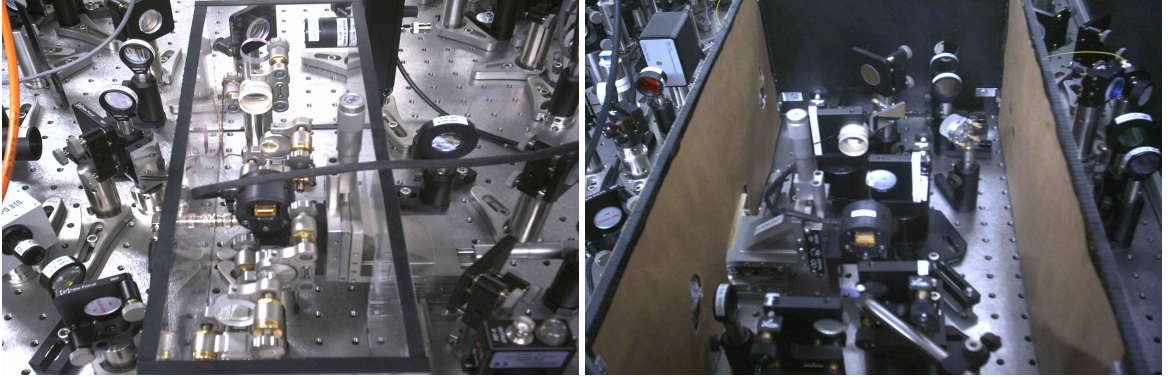


Figure 3.7: Pictures of the two OPOs: OPO2, the plant (left), and OPO1, the controller (right). The box surrounding OPO2 is smaller and contains only the cavity, while that surrounding OPO1 is larger and includes the pump beam coupling optics. This unfortunately makes tweaking up the pump alignment more difficult for OPO1, but the wider box allows additional components (for e.g. a removable beam block) to be more readily inserted into the cavity.

while for OPO2 the pump is combined with the coherent input at a dichroic mirror and then injected into the curved mirror (fig. 3.1). As is discussed in Appendix C, for a fundamental (i.e. signal) cavity mode with a given beam waist in the crystal, there exists an optimal beam waist for the pump to maximize the pump-signal coupling in the crystal (for a degenerate parametric process the pump waist should be smaller by a factor of  $\sqrt{2}$  and should occur at the same position as the signal waist [34]). However, because the pump beam is not resonant with the cavity (so we can't readily use the standard trick of monitoring beam transmission to check its mode matching, as is discussed below), a good trick to figuring out what the beam parameters should be is to send in a fundamental beam of high enough intensity to generate a visible second harmonic beam, measure its parameters, and then choose the pump mode matching lenses and their positions roughly by Gaussian beam optics. Then, we send in a signal beam, and try to optimize the parametric amplification while aligning the pump to it (we must then typically move the lenses, and perhaps try different lenses to get the focal position correct *and* size of the pump beam correct, while tweaking the mirrors to keep the two beams overlapped). Improving the pump coupling incrementally can be very difficult when a lot of noise or drift is present in the cavity length, and thus doing this with the box on and surrounding noise sources as suppressed as possible is advised! Once reasonably well coupled, the pump alignment is sensitive enough that mechanical drift in the optics over the course of a few hours can cause the coupling efficiency to drop significantly, and thus it must be re-tweaked to maintain optimal coupling.

The two OPOs are connected in a feedback configuration such that the output of the 4% outcoupler of OPO2 is sent to the 18.5% outcoupler in OPO1, reflects off it, and is returned to the 8% coupler of OPO2 (fig. 3.1). It's important that different ports (i.e. mirrors) on OPO2 are used on the feedback path, as using the same mirror would then cause a 3rd ring cavity to form along the feedback path, and the coupling to this intermediate cavity which would introduce additional dynamics at the cavity decay rate timescale and the effective coherent controller in the feedback loop would be a different system. As discussed in the next section, the roundtrip feedback phase is controlled by a pair of protected silver mirrors from Thorlabs (P01

coated) mounted on piezoelectric actuators, and an optical isolator (IO-5-1064-VHP, also from Thorlabs) is also placed on the path to prevent the backscattered forwards light (as well as the leaking injected backwards beam used for cavity locking) from propagating around the loop and causing interference effects. To align the feedback loop, we first align an injected forwards signal beam into the plant cavity (done via the  $R \approx 99.66\%$  curved mirror) and confirm that it's well mode matched, lock the OPO2 cavity, then align the output of the 4% outcoupler to the input of OPO1 and confirm that it's well mode matched, lock the OPO1 cavity, and then finally align the reflected beam off OPO2 into the 8% outcoupler of OPO1 and confirm that it's also well mode matched. This last step of the feedback alignment is done by sweeping the feedback phase and monitoring the height of the peaks (and depths of the troughs) of the OPO2 transmission signal and tweaking the mirrors to adjust the contrast. However, it's important to note that the alignment position which maximizes this contrast for coupling into the OPO1 cavity is generally different from that which maximizes the contrast for the case of "trivial" feedback, where a beam block is placed inside the OPO1 cavity and the light simply reflected off the outcoupler. As discussed in Chapter 2, this is because the optical transfer function that determines the height and depth of the OPO2 transmission signal as the feedback phase is swept is complicated beyond the simple "change in cavity linewidth" interpretation valid for the "trivial" feedback case, and nominally making the coupling back to OPO2 a little worse may actually increase the peak contrast. For the data presented in the next Chapter, the alignment was done to maximize peak contrast for the "trivial" feedback case, and then the beam block was removed and light allowed to couple into the OPO1 cavity, but it should be noted that the "optimal" way to align the feedback from OPO1 is still a direction worth investigating.

### 3.3 Locking schemes

Next, we describe the locking schemes used to stabilize the cavity lengths and relative phases of the beams. Both schemes use the same basic idea that consists of phase modulation on an input optical signal, detection of either a reflected or transmitted

beam from the cavity, and mixing the photodetector signal with an electronic local oscillator (LO) at the modulation frequency to obtain an error signal which is then used by an electronic servo to stabilize the path length. This idea, known as the Pound-Drever-Hall method, is very well detailed in refs. [35, 36]; here, we focus on the specific details as they apply to our apparatus.

The cavity locking in each OPO is achieved by first sending a signal beam (at the fundamental wavelength of 1064.4 nm) through a free-space coupled electro-optic modulator (EOM, broadband model 4004 from NewFocus) that is driven by a voltage controlled oscillator (VCO) at a radiofrequency ( $\approx 47$  MHz for OPO1 and 35 MHz for OPO2) (see fig. 3.8). This creates optical sidebands on the beam at  $+$  and  $-$  the phase modulation frequency, and the modulated beam is then sent backwards into one of the mirrors on each OPO (the high reflector flat on OPO1, the the  $R \approx 99.90\%$  curved mirror on OPO2). The reflected beam is then detected by a detector with large enough bandwidth to see the sidebands (a NewFocus 1811 for OPO1 and MenloSystems APD for OPO2), and the detector output sent to a mixer that multiplies this signal with part of the output from the VCO. The output of the mixer is filtered to block twice the VCO frequency and the resulting error signal is sent to a homemade electronic servo controller (design shown in Appendix B) that then actuates the piezo on one of the cavity mirrors (the high reflector flat on OPO1, the 4% outcoupler on OPO2) to lock the cavity on resonance with the fundamental wavelength. This technique of using a backwards beam at the same frequency as the forwards beam avoids some of the difficulties encountered when using other beams with different wavelength (e.g. a HeNe beam or part of the pump beam) for cavity locking, as both forward and backward beams share the same cavity frequency response and the error signals are easy to work with (the wavelengths mentioned above are very weakly resonant and generate small error signals). However, the downside in this particular setup (which is primarily due to the less than ideal coatings on the crystal facets) is that the backscattered light from the forwards beam interferes with the backwards beam and messes up the error signal at high forward powers (note that since the error signal is proportional to the temporal *derivative* of the photodetector signal, even small changes in this signal can significantly affect the error signal). For OPO1, to avoid

this problem, which is significant at even moderately low forward powers of 10's of  $\mu\text{W}$ , the backwards locking beam is detuned from the forwards beam by exactly 1 cavity free-spectral range (FSR) by quadruple passing it through an acousto-optic modulator (AOM, 2 W model from NEOS; each pass through the shifts the frequency by  $\approx 112$  MHz, and a detuning equal to the FSR of OPO1,  $\approx 450$  MHz, is reached after 4 passes, see 3.1). Thus the two beams ideally don't interfere with each other, and in fact that's the case at those forward power levels. However, it turns out that at high forward power (10's of mW or more), it's likely that other nonlinear processes in the crystal generate enough power at the locking beam frequency to once again cause trouble for the error signal, and thus this scheme limits the amount of forward power that can circulate in OPO1 before the lock fails. For OPO2, it turns out that the higher transmission of the curved mirror through which the backwards beam gets injected gives a larger backwards circulating power and the forward power that can be tolerated before the lock fails is significantly larger (at least  $\sim \text{mW}$ ), thus this beam isn't detuned from the forward beam frequency and is simply injected into the cavity. Again, however, the scheme fails at large forward powers. This suggests that a good locking scheme for the system in a very high forward power regime (e.g. pumped well above the lasing threshold) might be to use beams at frequencies far enough away from the phase matching frequency bandwidth of the crystal ( $\sim 40$  GHz or so) to avoid interaction with the forward beam, but close enough so that the reflectivities of the cavity mirrors aren't too different, and have it such that these beams can be detuned (say via AOMs) such that their resonance coincides with a forward beam resonance for the same cavity length.

The phase locking scheme for locking the relative phase of the pump beam to the signal beam in each OPO is very similar to the cavity locking scheme, with the main differences being that the pump phase (instead of the signal phase) is phase modulated, and at a frequency ( $\sim 30$  kHz) that is *lower* than the linewidth of the cavity ( $\sim 10$  MHz). This is done by reflecting the pump beam off a small (7 mm diameter) protected silver mirror (P01 coating from Thorlabs) mounted on a short range piezoelectric stack (AE0203D04F from Thorlabs) and dithering the mirror position at the desired modulation frequency (the mirror/stack combination has resonances

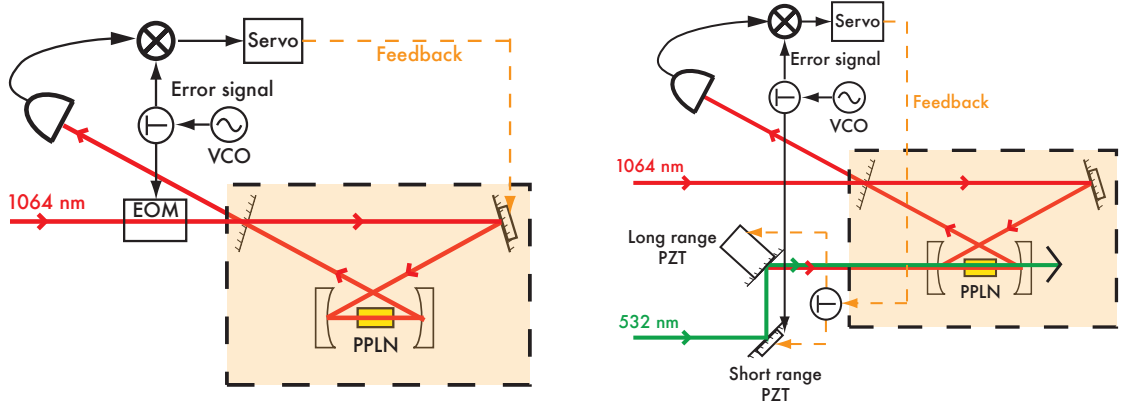


Figure 3.8: OPO cavity locking (left) and pump beam phase locking (right) schemes. Although not shown in the diagrams, there is a low pass filter to block the signal at twice the modulation frequency generated during mixing before the servo, a high voltage amplifier on the output of the servo to drive the piezos, and additional low pass filters before the piezos. The actual phase locking scheme in the apparatus works via the detection of a *transmitted* (instead of reflected) signal, see fig. 3.1 for an anatomically correct picture.

at 35 kHz and above when mounted on optical mounts that are much heavier). The reason the frequency is lower is that now the sidebands make it through the cavity, allowing the Pound-Drever-Hall method to work via detection of a transmitted (instead of reflected) beam, which is useful given the way the signal is injected into the coherent feedback loop for both OPOs (fig. 3.1). The long range piezo stack (PAS009 from Thorlabs with a 0.5 diameter in. P01 mirror mounted on it) is also used in conjunction with the short range stack in the pump path to facilitate phase locking for extended periods of time (closing the curtains around the apparatus also helps).



### 3.4 Detuned coherent input and optical noise generation

Instead of injecting a coherent amplitude at the fundamental frequency, the apparatus is also configured to send a detuned coherent beam or noisy, "thermal" beam (or some combination of both!) into the signal input port of OPO2. The way this works is as follows.

Part of the fundamental beam is sent through an AOM (from NEOS, operational from 25 to 40 MHz) and detuned away from the cavity resonances, and then it's phase modulated by a fiber coupled EOM (Photline NIR-MPX-LN-10, with up to 10 GHz bandwidth, henceforth referred to as the "Photline") to generate sidebands that lie at the desired detuning (see fig. 3.1). With the flipper mirror in place (actually a NewFocus 9807 adjustable mirror mount mated to a removable magnetic base, Thorlabs NX1F), the detuned beam (one of the sidebands) is sent into the injection port of OPO2. The max amount of power transferred to each of the sidebands is considerable (34% of the original beam power, see [35]), allowing the detuned beam to have considerable power, and it's this detuned beam that's used to characterize the narrowband nature of the controller as shown in the next Chapter. Because this beam passes through the Photline, it turns out that there is a considerable amount of phase drift present (due to changes in refractive index of the fiber) in the output beam, and the long range piezos are very useful to keep this beam phase locked relative to the pump beams when desired.

A noisy, "thermal" beam can also be generated in this beam's place by driving the Photline with broadband electronic noise from a function generator (here, we used a Tektronix 3102 AFG, as well as a 1 W RF amp from Minicircuits was used to boost the electronic noise power). The noise generates a continuum of optical sidebands that span a frequency range equal to the noise bandwidth on either side of the main beam frequency, and these sidebands behave as optical noise (simulating a "thermal" state of the electromagnetic field) by simultaneously injecting a continuum of coherent states with randomized phase at different frequencies. The noise can be wider than the bandwidth of the cavity, or narrower and centered at a desired detuning by first

low passing the noise from the function generator to reduce the bandwidth to a desired amount, and then mixing it with an additional electronic signal at the desired detuned frequency (multiplication in the time domain = convolution in the frequency domain, so a detuned "lump" of optical noise is generated).

### 3.5 Homodyne detection

Here we briefly discuss a part of the apparatus that was not directly involved in the measurements presented in the next Chapter, but that will be very useful for squeezing measurements and as well as further experiments involving broadband noise rejection with coherent feedback.

Part of the main signal beam (that is not detuned from the OPO cavities) is split off to act as a local oscillator (LO) for an optical balanced homodyne measurement of the output of OPO2 (see fig. 3.1). The LO beam is first "cleaned" by sending it through a mode matching cavity that has identical properties as the OPO cavities (save that it lacks the PPLN crystal at the center), which removes the spatial noise on the beam so that it will be well mode matched to the OPO signal output. The LO is then combined with the signal beam on a 50/50 beamsplitter and the output beams are measured by a pair of ETX-500T (from JDS Uniphase) photodiodes arranged in subtracting configuration in order to detect the noise variance of the electric field in the signal beam (see [37], Chapter 18 for a detailed description of this scheme). Because the photodiodes were not AR coated, a substantial reflection ( $\approx 12\%$ ) was present off the facet of each photodiode. This would severely limit the quantum efficiency in the detection process (and thus the amount of squeezed noise variance that could be detected), but fortunately the reflected beams can be nearly retroreflected via prisms (Thorlabs PS971-C) onto the detectors at a slight angle so that most of the reflected light can still be detected, but the reflected beams don't back propagate throughout the apparatus to cause undesired interference effects. Including the effects of absorption in the passivation layer on the photodiodes, the overall quantum efficiency of the detectors with the reflected beams is  $\approx 97\%$ , an excellent value for measuring squeezing values significantly less than 10 dB, which is what is generated

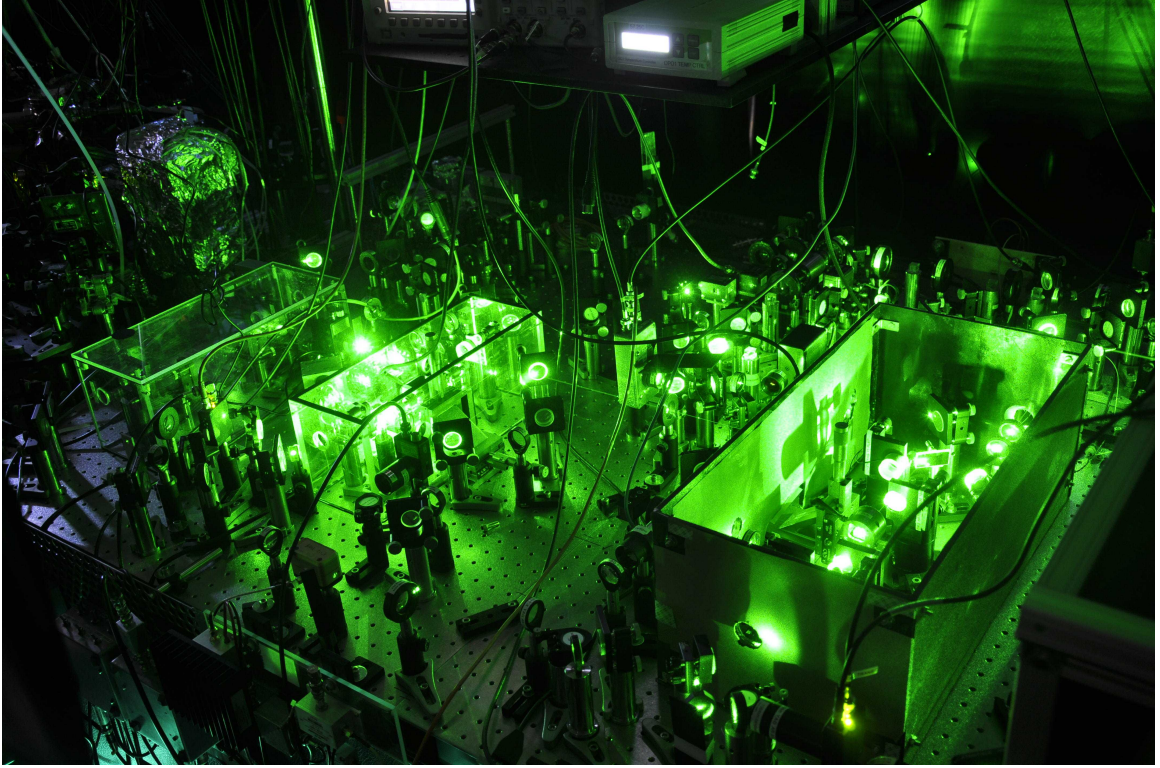


Figure 3.9: Pumping both OPOs with a significant amount of pump power, which should enable generation of interesting squeezing spectra and perhaps limit cycle behavior.

by the OPOs in the apparatus. Squeezing measurements from each individual OPO were performed that were easy to interpret and showed the amounts predicted by theory, but difficulties (discussed at the end of the next Chapter) were present that made measuring and interpreting squeezing from the system in the coherent feedback configuration difficult. However, when both OPOs are pumped with a significant amount of pump power (see fig. 3.9), and feedback phase locked to an appropriate value, interesting squeezing spectra should be visible, as well as a change in system dynamics that shows a large amplitude oscillation of power between pump and signal beams (limit cycle behavior).

# Chapter 4

## Experimental Results

In this Chapter we present experimental results central to the investigation of the coherent feedback setup used for narrowband disturbance rejection and stability modification of the "plant" OPO. Here, we will revert to calling the plant OPO the "Plant" for short (i.e. OPO2 in the previous chapter), and the controller OPO the "Controller" (i.e. OPO1 in the previous chapter).

### 4.1 OPO characterization

We first characterize the behavior of the OPOs to determine their individual properties before connecting them in the feedback loop configuration (see figs. 4.1 and 4.2). To do so, a coherent input at the signal wavelength (1064.4 nm) at moderately low power ( $\sim 1 \mu\text{W}$ ) is injected into each OPO, the cavity locked, and the pump beam turned on and its phase swept relative to that of the signal beam. As this phase is swept (typically by several multiples of  $2\pi$  as the piezoelectric stack is displaced by a few wavelengths), the signal alternates between amplification and de-amplification: the relative phase of the two beams determines the phase matching condition for energy transfer between the two beams. At a given pump power, for *low* signal power relative to the pump beam power (so pump depletion is negligible), the expected amounts of maximum amplification and de-amplification follow the theoretical curves [38]:

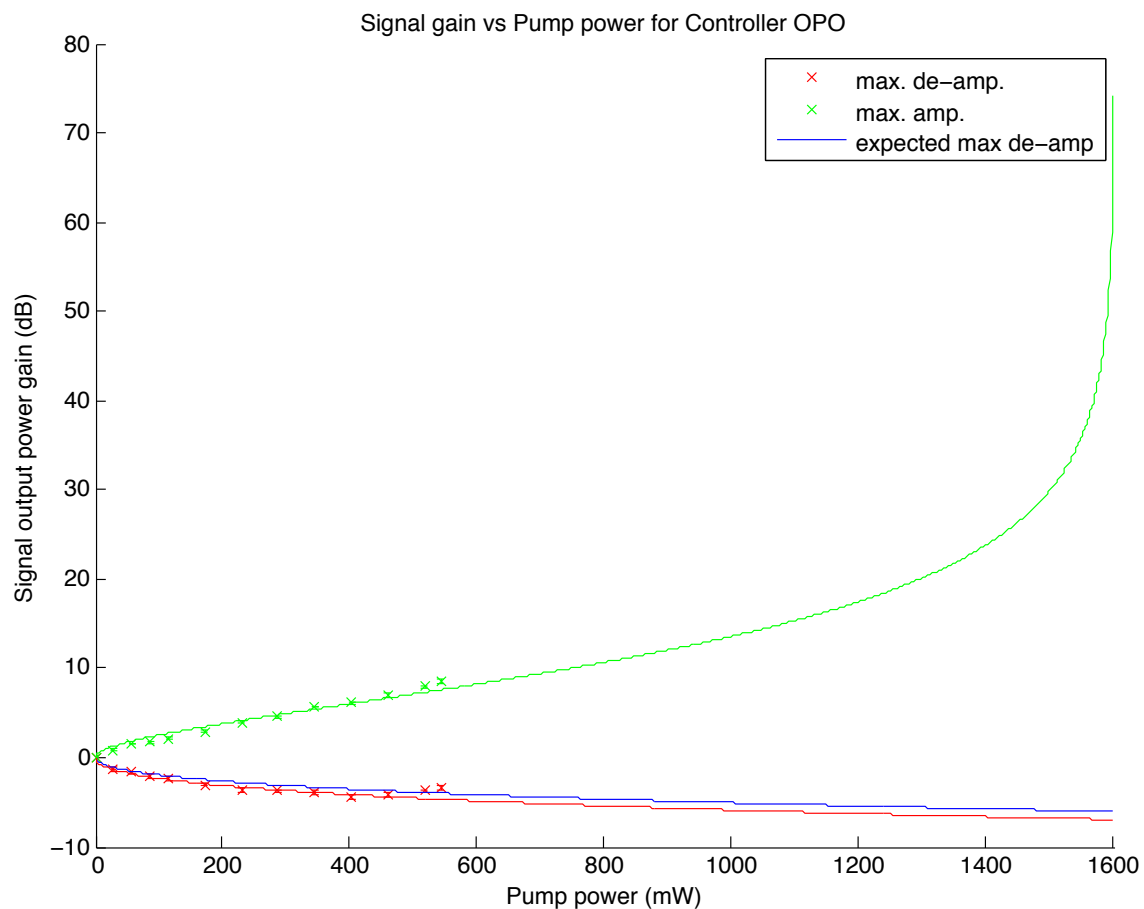


Figure 4.1: Signal gain vs pump power for OPO1 (Controller). Green and red lines display fits to data, blue line displays de-amplification fit corresponding to the expected amount given the amplification (green) data. Predicted threshold power  $\approx 1.6$  W.

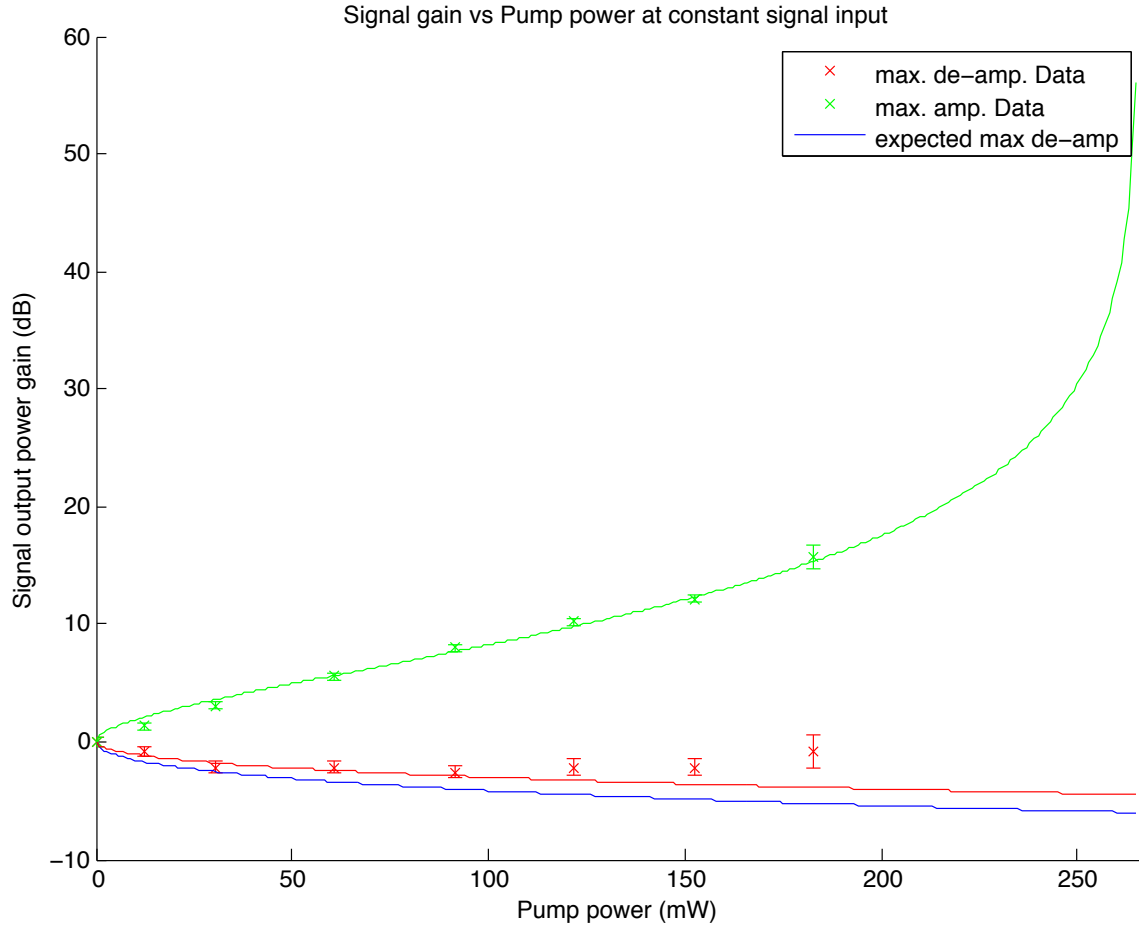


Figure 4.2: Signal gain vs pump power for OPO2 (Plant). Green and red lines display fits to data, blue line displays de-amplification fit corresponding to the expected amount given the amplification (green) data. Predicted threshold power  $\approx 260$  mW, agrees to within 10% of actual measured values.

$$G_+ = \left( \frac{1}{1 - \sqrt{P/P_{\text{thr}}}} \right)^2 \quad (4.1)$$

for amplification and

$$G_+ = \left( \frac{1}{1 + \sqrt{P/P_{\text{thr}}}} \right)^2 \quad (4.2)$$

for de-amplification, where  $G_+$  and  $G_-$  are the power gains,  $P$  is the pump beam power and  $P_{\text{thr}}$  is the threshold pump power. Thus, we can determine the threshold pump power for each OPO by fitting the data, which also gives us an idea of how well the pump beam is coupled to each OPO. If the coupling of the pump beams were equal, we would expect a Controller threshold to be about  $2$  to  $3 \times$  that of the Plant given the  $\sim 1.5 \times$  higher cavity decay rate in the controller [39], but instead we find it to be a still a bit higher than this expected value, indicating poorer pump coupling in the Controller. Nevertheless, the coupling is good enough to realize gains of several dB for the available pump power, which is enough to substantially affect the dynamics of the Plant in the feedback loop configuration as we discuss below. As noted in the previous Chapter, the pump coupling to the OPOs changes significantly over a few hours due to thermal-mechanical drift in the optics, and a re-tweaking of the alignment is needed to reproduce the behavior shown in figs. 4.1 and 4.2.

## 4.2 Narrowband disturbance rejection and amplification

We next examine the properties of the closed loop system when a coherent (narrow-band) input is injected into the Plant input port. To help develop some intuition for what's going on, we first consider the case where the input is on resonance with the (locked) OPO cavities and the case where the Controller is *not* pumped (i.e. there is only loss in the feedback loop, and no gain).

We find that, as expected, as the coherent feedback phase  $\Phi_{\text{FB}}$  is swept over a range

of a little more than  $2\pi$  and the transmission output port of the Plant is monitored with a photodetector, the detection signal alternates between minima and maxima corresponding to destructive and constructive interference in the plant cavity (see fig. 4.3), and thus suppression and enhancement of photon number. We see that the case of "trivial" feedback (when the feedback beam is reflected off the Controller input coupler without entering the cavity) already produces a substantial effect, due to a broadening and narrowing of the cavity effective linewidth ([19] and equation 2.96 in Chapter 2). The case of "empty cavity" feedback (non-pumped Controller) doesn't provide much better suppression (still about a factor of 2), but it does provide better enhancement, and the intuition behind this can be roughly thought of as the fact that the reflectance of the cavity on resonance is actually higher (due to optical impedance mismatch of its mirrors, see Appendix A for an example with similar cavity mirrors) than the input coupling mirror alone, and thus there is less loss in the feedback path and the fed back beam ostensibly has a larger effect.

Next, we examine the case in which the Controller is pumped (so now there's gain in the feedback loop; see fig. 4.4). With  $\Phi_{\text{FB}}$  locked to the values that either maximize or minimize the photon number and the pump phase swept relative to the signal phase, we see that the effects of gain are indeed to enhance the effect of coherent feedback, and the photon number can be further enhanced or suppressed with it. As noted above, sweeping the pump phase causes the Controller to alternate between providing gain or even more loss; this phase can also be locked if desired, but the main point is that the gain provides a critical degree of freedom that adjusts the strength of the feedback and allows the coherent controller to tailored towards the application at hand.

We can also see the strong influence of  $\Phi_{\text{FB}}$  on the response of the system to gain by looking at the pump powers required to substantially effect the photon number when  $\Phi_{\text{FB}}$  is locked (see figs. 4.5 and 4.6) and the pump phase swept. For the case when  $\Phi_{\text{FB}}$  is locked to maximize photon number, we see that it only requires a very small amount of pump power to significantly effect the photon number in the cavity (values shown for pump powers up until the point when the  $\Phi_{\text{FB}}$  lock fails, probably due to significant change in the signal amplitude during locking). For the



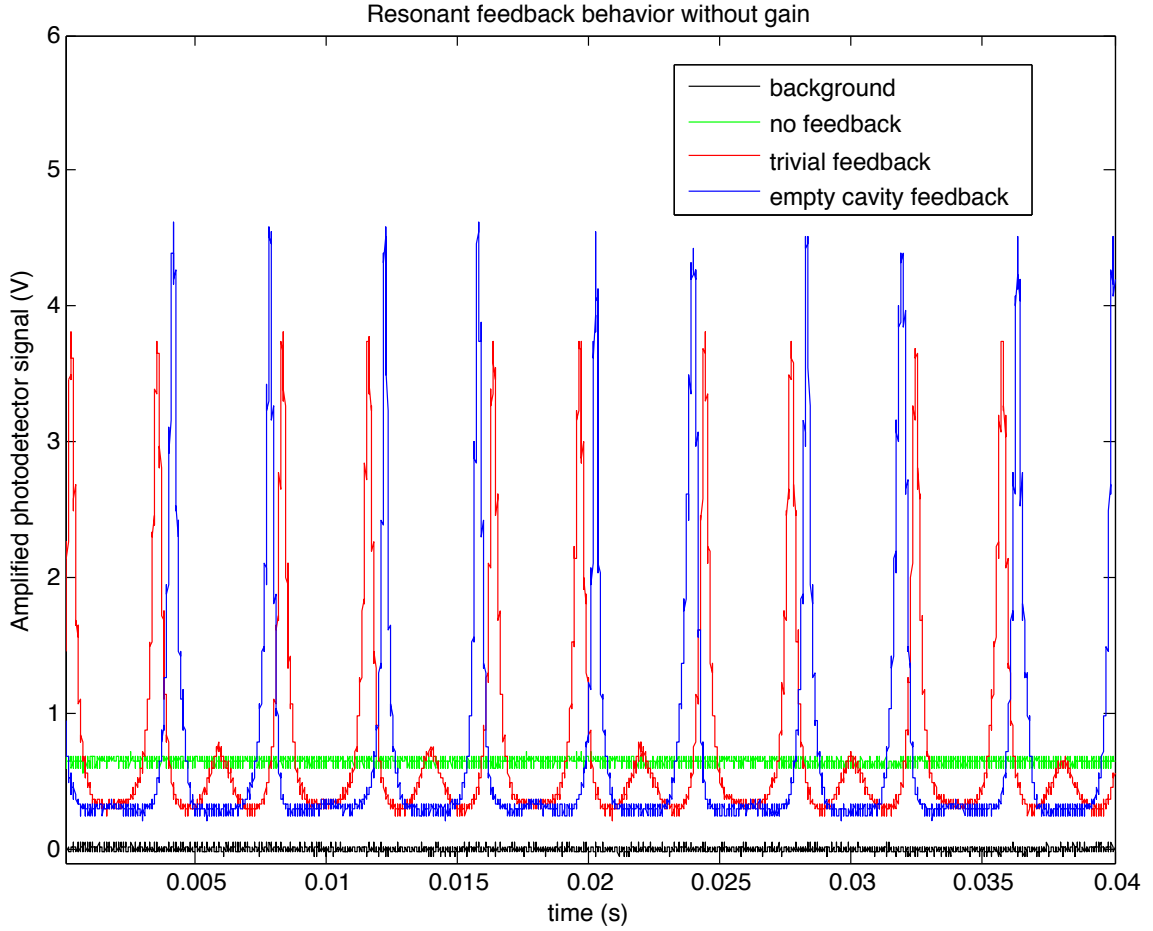


Figure 4.3: Effects of resonant coherent feedback on the Plant photon number without gain in the feedback loop. Coherent feedback phase swept sinusoidally at 115 Hz. Black corresponds to no Plant input, green to the equilibrium photon number without feedback, red the case of "trivial" feedback, and blue the case of "empty cavity" feedback. This and the following traces taken on a Tektronix 3052 Oscilloscope.

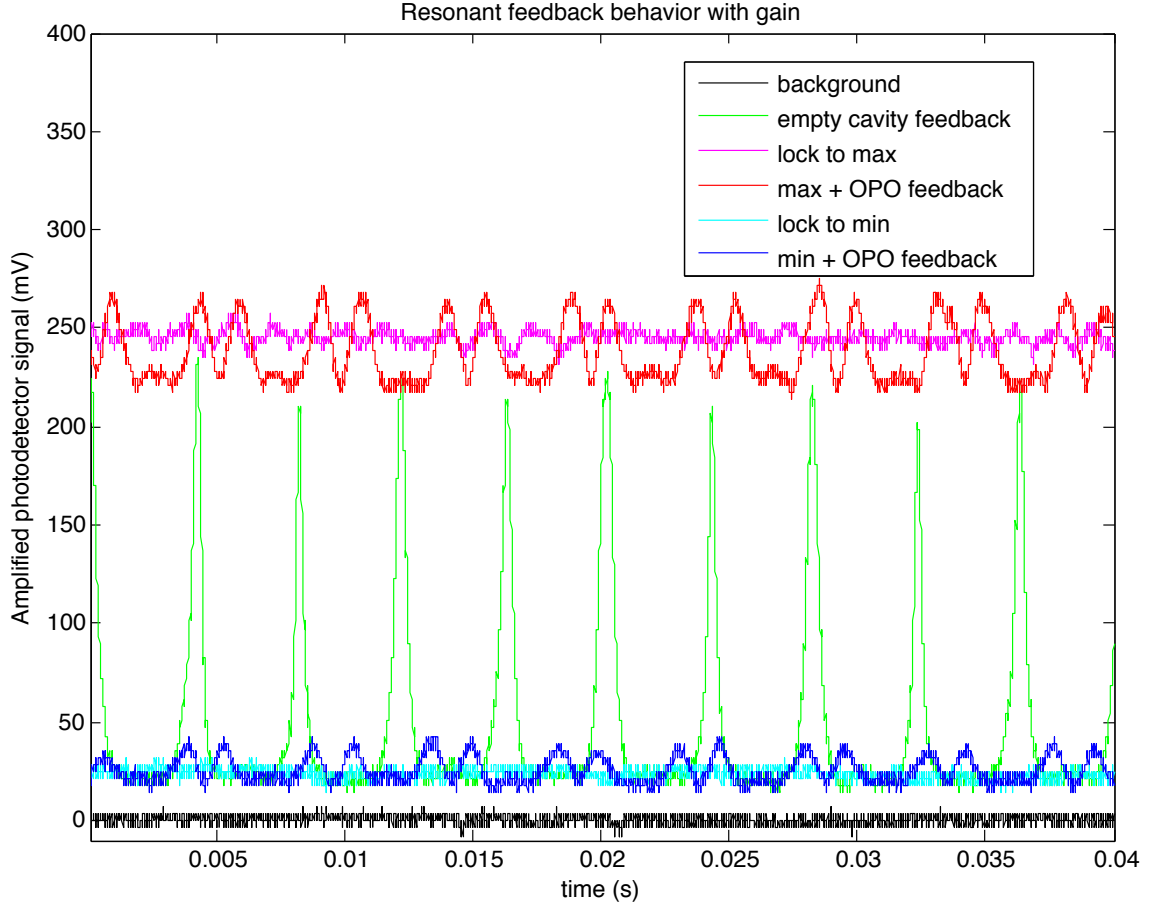


Figure 4.4: Effects of resonant coherent feedback on the Plant photon number with gain in the feedback loop. Coherent feedback phase  $\Phi_{FB}$  swept sinusoidally at 115 Hz for comparison (green) then locked for the remainder of the traces. Purple corresponds to  $\Phi_{FB}$  locked to maximize photon number, red with the Controller pump on and pump phase swept relative to signal phase, light blue with  $\Phi_{FB}$  locked to minimize photon number, and blue with once again with the Controller pump on and pump phase swept. The apparent offset between the peak of the green trace and purple trace and trough of the green trace and light blue trace are due to drifts in the  $\Phi_{FB}$  lock, which is very sensitive to mechanical/acoustic disturbances. The pump power for the blue trace is significantly larger than that for the red trace, see the following figures and explanation in the text.

case when  $\Phi_{\text{FB}}$  locked to minimize photon number, substantially more pump power is required to achieve the same fractional changes in the Plant photon number. We might obtain a more insightful explanation for this in the future, but for now we note that this behavior makes sense as the reduced cavity loss for the Plant in the former configuration are likely to make it more sensitive to small changes in gain the feedback loop, in a manner similar to how small changes in pump power have a larger effect on the gain of an OPO with narrower linewidth than one with a broader linewidth. It turns out that further suppression of the photon number much beyond the values shown in fig. 4.6 is actually rather difficult; although it should work in principle, the stability of the  $\Phi_{\text{FB}}$  lock limits the extent to which it can be done (see fig. 4.7).

Thus, the system seems to perform as expected on resonance and increases disturbance rejection (or amplification) as expected when gain is applied. However, the effects of detuning the input beam off resonance are also important and illustrate the narrowbandedness of the controller. When the coherent input beam is detuned off the cavity resonance using the method described in the previous Chapter, we find that, in general, the effects of feedback decrease (see fig. 4.8). This makes sense, as both the Plant and Controller are finite bandwidth systems and coupling to them decreases off resonance. Photon number enhancement in the Plant seems to decrease monotonically with increasing detuning regardless of the feedback scheme used, while the suppression also seems to exhibit the same behavior, except for the case of trivial feedback (a detailed analysis in the future might reveal why, but for now we note general trends of this system are as expected).

Although not shown here, additional measurements done when broadband noise (100 MHz bandwidth) is injected into the system reveal that each coherent feedback scheme discussed above fails to achieve photon number (i.e. noise) suppression in the Plant. This isn't surprising for two reasons: we know the effects of feedback are reduced for frequencies detuned from the plant resonance, and additionally, each frequency component of the noise will receive a different phase shift upon reflection off the Controller, and thus the value of  $\Phi_{\text{FB}}$  for which it achieves maximal constructive/destructive interference in the plant will be different. Thus, it'll be impossible for all these frequency components add or cancel for the same  $\Phi_{\text{FB}}$ , and the effect of

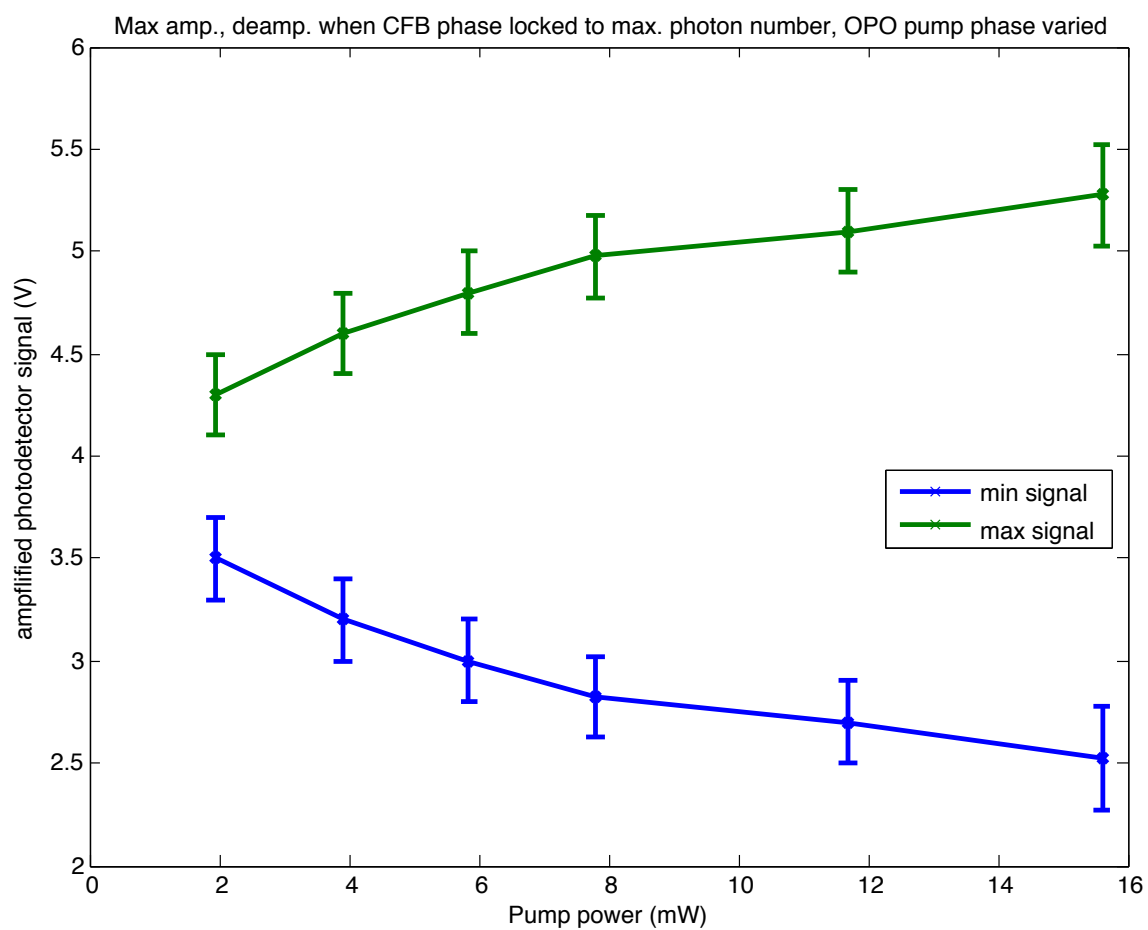


Figure 4.5: Maxima and minima of Plant output when  $\Phi_{FB}$  locked to maximize photon number. Error bars due to drifts in the  $\Phi_{FB}$  lock.

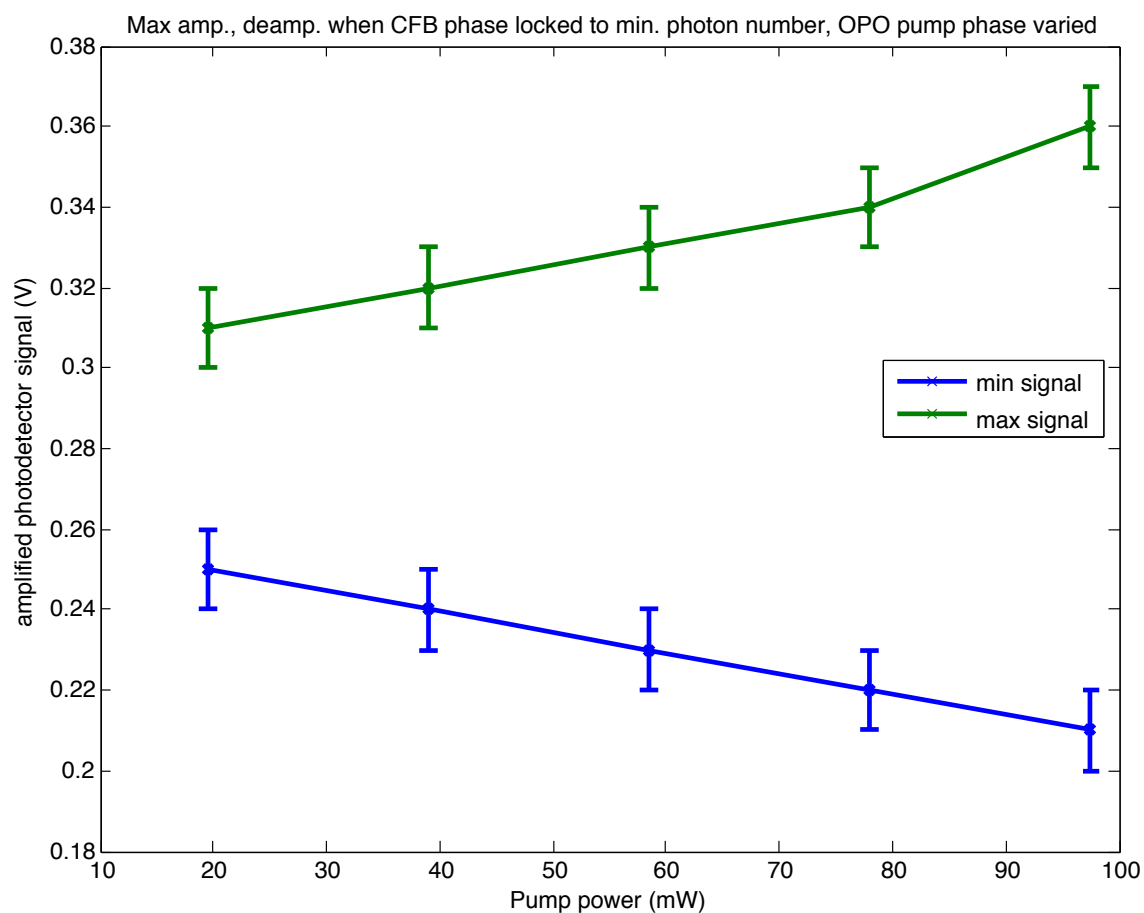


Figure 4.6: Maxima and minima of Plant output when  $\Phi_{FB}$  locked to minimize photon number. Error bars due to drifts in the  $\Phi_{FB}$  lock.

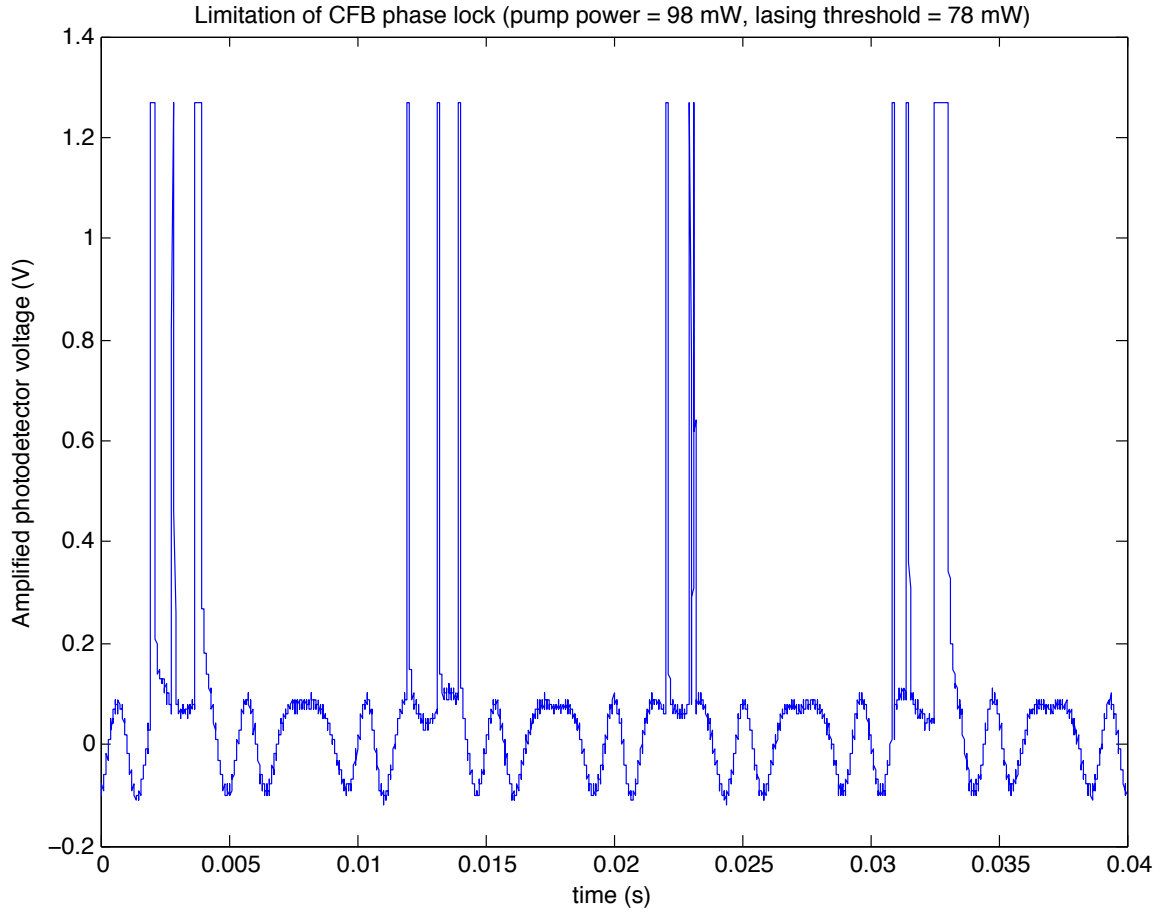


Figure 4.7: Trace showing maxima and minima of Plant output when  $\Phi_{\text{FB}}$  locked to minimize photon number but pump power high (above threshold for the closed loop system). We see that lasing is barely being suppressed by the  $\Phi_{\text{FB}}$  lock, and the lock fails for higher pump powers. Nevertheless, it shows the strong dependence of system dynamics and stability on  $\Phi_{\text{FB}}$ .

	Detuning			
Feedback Type	0 MHz	3 MHz	6 MHz	9 MHz
Trivial (min/max)	0.44/5.8	0.51/4.0	0.58/1.8	0.27/1.5
Empty cavity (min/max)	0.44/7.1	0.49/4.4	0.61/2.7	0.74/1.9
OPO pump = 98 mW (min/max)	0.33/lasing	0.49/4.9	0.61/3.0	0.74/2.0

Figure 4.8: Table showing the effects of input detuning on suppression and enhancement of the Plant photon number with different feedback schemes ("trivial" feedback, empty cavity feedback, and feedback with gain). Entries correspond to the ratio of the min/max photon number in that configuration (for  $\Phi_{\text{FB}}$  locked, pump phase swept) relative to the photon number with no feedback.

the feedback is washed out. Investigating the practical implementation of broadband coherent feedback schemes for noise rejection would be an interesting topic for future research.

### 4.3 System stability modification

We also examine the effects of the feedback loop on the system stability from perspective of reduction (or raising) the system lasing threshold. As mentioned in Chapter 2, we can consider the quadrature field operators of the Plant cavity mode as the canonical phase space operators of our quantum harmonic oscillator, and we note that a stable system (such as an OPO below threshold) will simply move toward the equilibrium value of the cavity field given the decay rate (and pump rate, if any) of the cavity, regardless of the initial state of the system. However, an OPO above threshold is an unstable system in that (in the ideal limit of no pump depletion) the amplitude of any initial state (including the vacuum) will increase without bound as long as the equations that govern its evolution hold. In practice, this stops as soon as the pump is depleted, but the concept is still important as the system dynamics

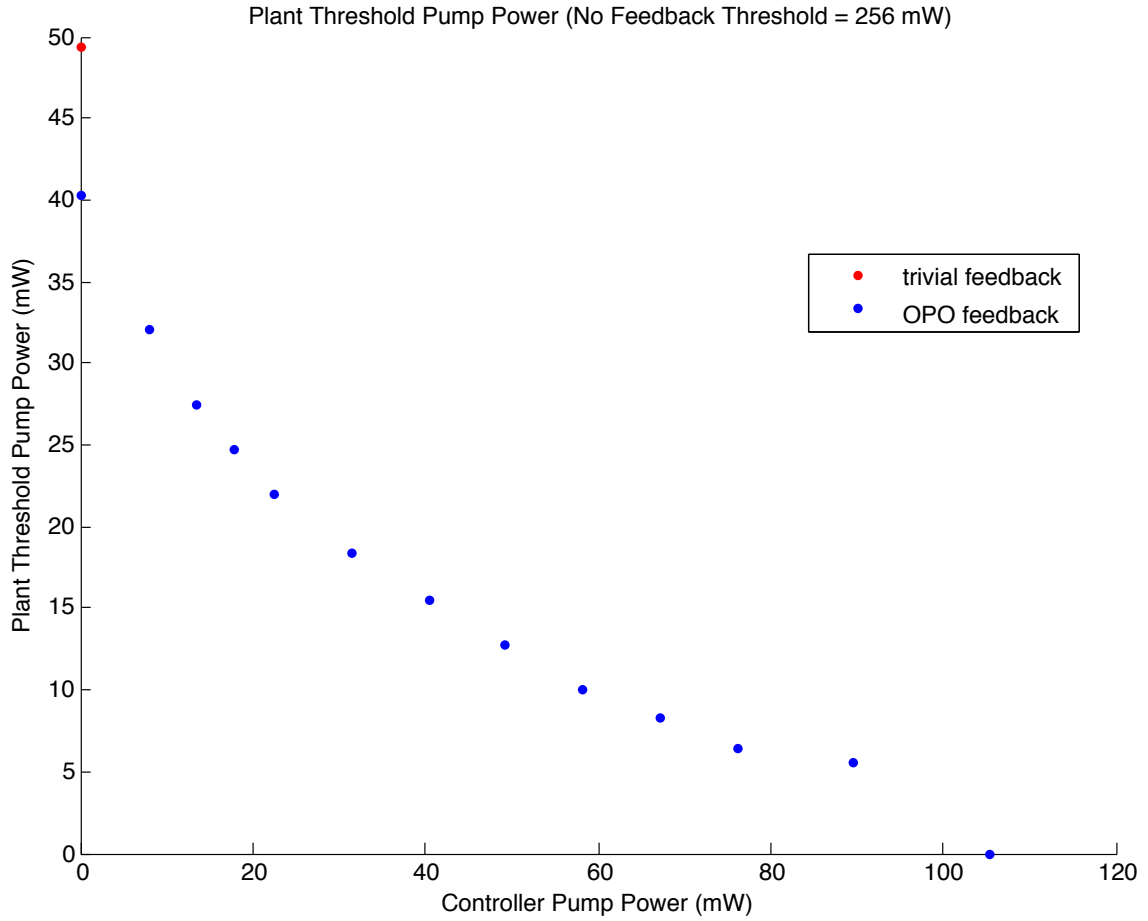


Figure 4.9: Threshold pump power for the Plant vs increasing pump power in the Controller when OPOs are connected in the closed loop configuration.

undergo a fundamental change and the state of the system is now drawn to the equilibrium manifold above threshold. When we connect the Plant to the feedback loop, we find that we significantly alter the pump power at which it is stable (see fig. 4.9), i.e. the pump power at which it lases.

We see that the Plant lasing threshold is reduced dramatically ( $5 \times$ ) when connected in even the "trivial" feedback configuration, as the effective cavity linewidth is substantially reduced at the corresponding value of  $\Phi_{FB}$ . The empty cavity feedback reduces the cavity losses even further, and as gain is added from the Controller, we see that the threshold continues to lower monotonically, until it vanishes altogether. This



makes sense, as the condition for lasing is that the roundtrip loss for the Plant cavity equals the roundtrip gain, and when the Controller gain is a few dB, all the power lost from the Plant cavity during a single roundtrip is restored at the 8% coupling mirror of the cavity. Alternatively, from symmetry in the feedback loop construction, we can view the Controller as the "plant" and the Plant as the "controller", and we note that the combined system should lase if we only pump the Controller (which it does).

Just as we can reduce the lasing threshold for the Plant by adding coherent feedback with the appropriate values of  $\Phi_{\text{FB}}$ , we can also raise it and suppress lasing by using the other values of  $\Phi_{\text{FB}}$  (which correspond to the case of photon number suppression in the Plant, when the power cavity losses are increased and power routed away from the feedback loop). The easiest demonstration of this is can be seen from pumping the Plant above threshold, sweeping  $\Phi_{\text{FB}}$  and seeing that lasing is suppressed for part of the sweep. Unfortunately, as of the time of this writing the pump power available in the doubling crystal has dwindled so much that the Plant can't be pumped above threshold, and thus we leave it to the next intrepid researcher to switch out the doubling crystal and demonstrate this (see below).

## 4.4 Future directions

We briefly mention some future directions that can be explored with the apparatus (that would also be useful to compare with the theory) at this point.

Right off the bat, we note that if the pump power were restored (in the final weeks of the experiment, the poled regions in the doubling crystal deteriorated rapidly and the pump power significantly reduced below the ideal 1 W value), we would immediately be able to see the phenomena of lasing suppression for the Plant as mentioned above, which would demonstrate the idea of stabilizing an otherwise unstable system with coherent feedback, the complement to what we observed above. If the phase locking of the pump beams and  $\Phi_{\text{FB}}$  were improved, we could not only get more precise data similar to what was shown above and to try to get quantitative agreement with the theory developed so far, but we could also to investigate the effects of the

coherent feedback loop on the squeezing generated by the OPOs (the current problem is that the piezo modulation depth required to get a clean error signal is large, large enough to generate extra noise that obscures the measured squeezing spectrum when the phases are locked; increasing the modulation frequency and using detectors with narrower bandwidth would boost the signal to noise on the error signal and hopefully require less modulation depth for locking). If the cavity lock schemes were changed to enable the OPOs to be stabilized well above threshold, we could try to obtain clean measurements of limit cycles (if present), and even if the cavity locks fail, if pump power were restored we could look for them nonetheless. Finally, we could place an acoustic noise shield around the setup (but not touching the optical table) that would reduce the noise and give all the locks an easier time.

# Appendix A

## Bowtie Cavity Design

The bowtie cavity design affords a simple way to construct a ring cavity with relatively small astigmatism in the cavity modes. Here we detail the design of a symmetric bowtie cavity with two consecutive curved mirrors and two consecutive flat mirrors. Many variations on this design "theme" are possible, but for our purposes this design's symmetry and simplicity make it relatively easy to both analyze and construct. We first analyze the ranges of mirror radii of curvature and lengths over which the cavity supports stable modes, and then show the effects of inclusion of a crystal and astigmatism due to reflection off the curved mirrors at near-normal incidence. We conclude with the cavity frequency response, which depends on the cavity length, mirror reflectivities and intracavity losses.

### A.1 Geometry and Stability Range

A ring cavity with one or more spherical mirrors may support stable Gaussian modes, and these will be the modes of interest in our design. The stability requirement for a given mode is that the Gaussian beam repeats itself after a cavity roundtrip (see for e.g. §4.5 of [37]), i.e.

$$q = \frac{Aq + B}{Cq + D} \tag{A.1}$$

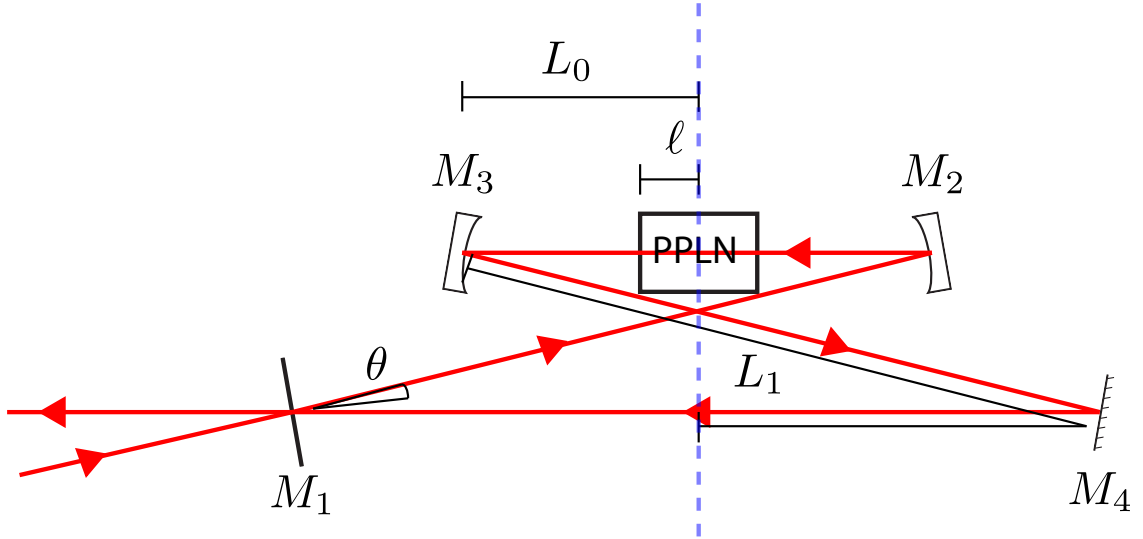


Figure A.1: Symmetric bowtie ring cavity with two flat mirrors ( $M_1$  and  $M_4$ ) two curved mirrors ( $M_2$  and  $M_3$ ). The resonant beam of interest (shown in red) enters and leaves the cavity predominantly via  $M_1$ , with the other mirrors being high reflectors at the cavity frequency. The cavity is symmetric about the dashed line, with the curved mirrors separated by a length  $2L_0$ , and the remaining cavity length  $2L_1$  (so the empty cavity roundtrip perimeter  $p = 2L_0 + 2L_1$ ). The crystal has length  $2\ell$  and index  $n$  (so, with the crystal, the cavity perimeter is  $p = 2(L_0 - \ell) + 2n\ell + 2L_1$ ), and the nominal small angle of incidence on all mirrors is  $\theta$ .

where  $q$  is the complex Gaussian beam parameter at any particular position along the beam path in the cavity, and the  $A$ ,  $B$ ,  $C$  and  $D$  parameters correspond to the entries of the cavity roundtrip  $ABCD$  matrix for that position. Intuitively, given the layout of the curved and flat mirrors of our cavity as shown in fig. A.1, we note that our stable cavity mode should be a Gaussian beam with a particular Rayleigh range in the region between the pair of curved mirrors, and then reflection off the first curved mirror changes the Rayleigh range (in accordance with the appropriate  $ABCD$  transformation for the mirror), and then beam continues to propagate until it reaches the second curved mirror, reflects and regains its initial Rayleigh range. To simplify our analysis, we note that if we truly have a symmetric cavity with the same radius of curvature  $R$  for both curved mirrors and symmetric mirror placement, then the beam waists will occur at exactly the midpoints between the the curved and the flat mirrors. At these positions, since the beam radius of curvature is infinite,  $q$  is purely imaginary ( $q = iz_R$ , where  $z_R$  is the Rayleigh range of the beam) and we can readily solve for the Rayleigh range of each beam from the above mode stability criterion: each must satisfy the quadratic equation

$$Cq^2 + (D - A)q - B = -Cz_R^2 + i(D - A)z_R - B = 0. \quad (\text{A.2})$$

First, we consider the beam waist between the curved mirrors, at a distance  $L_0$  from each curved mirror. The corresponding roundtrip  $ABCD$  matrix is just the product of the individual  $ABCD$  matrices corresponding to propagation to the first curved mirror, reflection from it, propagation up to the next curved mirror, reflection from it, and then back to the initial position (see for e.g. §2.1 of [37]):

$$\begin{bmatrix} A & B \\ C & D \end{bmatrix} = \begin{bmatrix} 1 & L_0 \\ 0 & 1 \end{bmatrix} \begin{bmatrix} 1 & 0 \\ -1/f & 1 \end{bmatrix} \begin{bmatrix} 1 & 2L_1 \\ 0 & 1 \end{bmatrix} \begin{bmatrix} 1 & 0 \\ -1/f & 1 \end{bmatrix} \begin{bmatrix} 1 & L_0 \\ 0 & 1 \end{bmatrix} \quad (\text{A.3})$$

where  $f = R/2$  is the focal length of each curved cavity mirror. Carrying out the multiplication, we find that

$$A = \frac{f^2 - 2(L_0 + L_1) + 2L_0L_1}{f^2}, \quad (\text{A.4})$$

$$B = \frac{2[(L_0 + L_1)f^2 - (L_0^2 + 2L_0L_1)f + L_0L_1^2]}{f^2}, \quad (\text{A.5})$$

$$C = \frac{2(L_1 - f)}{f^2}, \quad (\text{A.6})$$

$$D = \frac{f^2 - 2(L_0 + L_1) + 2L_0L_1}{f^2} = A. \quad (\text{A.7})$$

Thus,  $D - A = 0$  and the quadratic equation for  $z_R$  becomes

$$z_R^2 = \frac{-B}{C} = \frac{(f - L_0)(L_0f + L_1f - L_0L_1)}{f - L_1}. \quad (\text{A.8})$$

Since  $z_R$  needs to be real and positive for a stable mode (and thus so does  $z_R^2$ ), we can now find the relationships between  $f$ ,  $L_0$  and  $L_1$  that satisfy this from eqn. A.8. Note that, from the geometry in fig. A.1, even if the flat mirrors are brought close together so that the distance between them is less than that of the curved mirrors (i.e.  $L_0$ ), we'll always have  $L_0 < L_1$ ; the limiting case of  $L_1 \rightarrow L_0$  just corresponds to the symmetric curved mirror Fabry-Perot resonator. In fact, taking this limit in eqn. A.8 with yields  $L_1 \rightarrow L_0 = L$  yields  $z_R^2 = L(2f - L)$ , exactly the expression for the symmetric Fabry-Perot resonator with mirror separation  $2L$ , as expected (see for e.g. §4.3 of [37]).

We thus have three cases:  $f < L_0 < L_1$ ,  $L_0 < f < L_1$ , and  $L_0 < L_1 < f$ . We immediately see that the intermediate case,  $L_0 < f < L_1$ , does not yield stable solutions, as the numerator of eqn. A.8 is then always positive while the denominator is always negative, so the overall expression is negative. The final case,  $L_0 < L_1 < f$ , always yields stable solutions as both numerator and denominator are always positive. Note, however, that theoretical limit in which the Rayleigh range (and thus focused spot size) approaches zero (ignoring the diffraction limit) only occurs as the mirror spacings  $L_0$  and  $L_1$  themselves approach zero; thus, if we desire a very small focus spot size, we have to bring the mirrors very close together, which may be difficult

to achieve in practice (especially if we're trying to insert something like a crystal in between them on the optical table).

However, the first case  $f < L_0 < L_1$  gives us the ability to approach the very small spot size limit between the curved mirrors while keeping larger mirror spacings, comparable to the focal length of the curved mirrors: the zero of the numerator of eqn. A.8 occurs at  $L_0f + L_1f - L_0L_1 = 0$ , i.e.

$$L_1 = \frac{-L_0f}{f - L_0}, \quad (\text{A.9})$$

or alternatively

$$L_0 = \frac{-L_1f}{f - L_1}. \quad (\text{A.10})$$

From eqn. A.8, we see that if either  $L_0$  or  $L_1$  exceed the values above, the numerator becomes negative and the mode is then unstable. To find the individual upper limits on  $L_0$  and  $L_1$  in terms of  $f$ , we then note that a stable mode requires

$$L_0 < L_1 < \frac{-L_0f}{f - L_0}, \quad (\text{A.11})$$

and for this to be possible, we need

$$L_0 < \frac{-L_0f}{f - L_0}, \quad (\text{A.12})$$

which means that we need fundamentally need

$$L_0 < 2f, \quad (\text{A.13})$$

in order to have a stable solution at all, regardless of the value we would choose for  $L_1$ . For a given  $L_0 < f$ , the upper limit on  $L_1$  is then given by eqn. A.9. With the above information in hand, we can plot the parameter regime where a stable mode exists.

As we see from fig. A.2, as  $L_0$  increases from  $f$  to  $2f$ , the range of possible choices for  $L_1$  for a stable mode gets narrower and narrower, and eventually closes

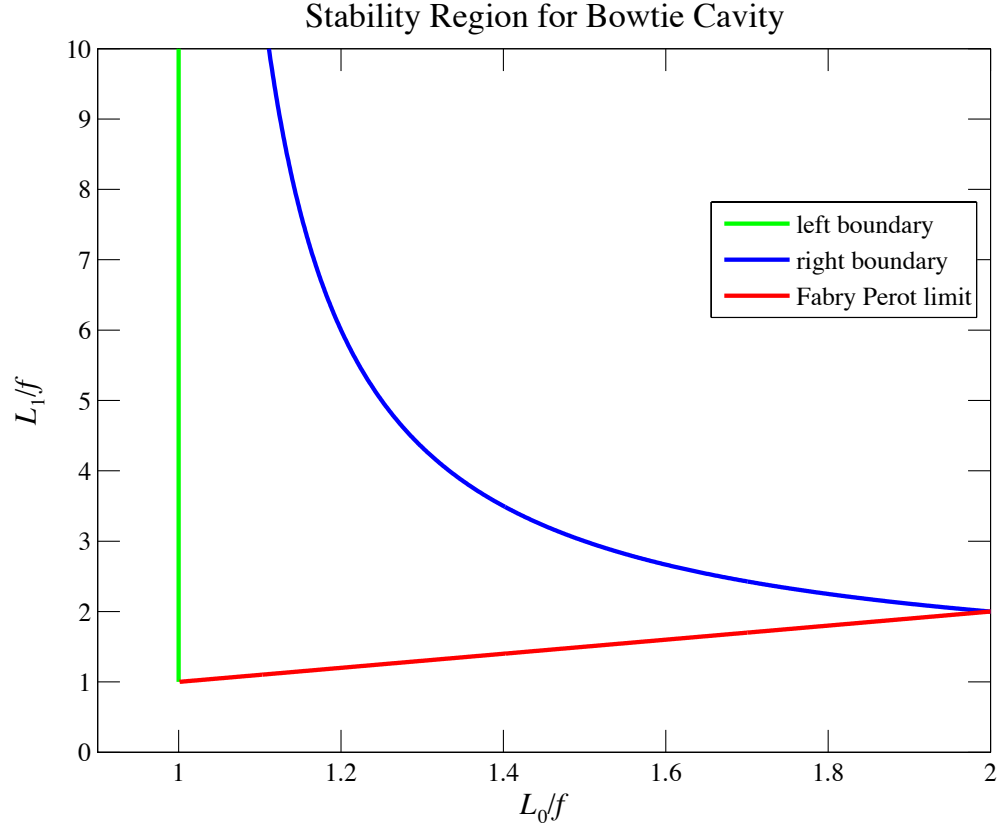


Figure A.2: Stability region for the bowtie cavity with  $f < L_0 < L_1$ : the resonator is stable between the left (green line), right (blue line) and lower (red line) boundaries. The lower boundary is the limiting case  $L_1 \rightarrow L_0$ , which corresponds to the symmetric curved mirror Fabry-Perot resonator. As either the left or the right boundary is approached, the focus spot size becomes very small, and  $L_1 \rightarrow \infty$  as  $L_0 \rightarrow f$  along the right boundary.



off altogether at  $L_0 = 2f$ . Near the left and right stability boundaries, the focus spot size becomes very small, and thus for a given length of either  $L_0$  or  $L_1$ , one can adjust remaining length to get close to the boundary and choose the spot size (as shown in another plot below). The lower boundary in fig. A.2 given by the line  $L_1 = L_0$  corresponds to the symmetric curved mirror Fabry-Perot resonator, and we note that the concentrically focused limit ( $L_0 = 2f = R$ ) is also the limit beyond which the Fabry-Perot resonator is unstable. As a reminder, as mentioned above, the left boundary occurs because the case  $L_0 < f < L_1$  is unstable.

Our analysis so far has been sufficient to determine both the stability regime of the bowtie cavity and the Rayleigh range (and thus focus spot size) between the two curved mirrors. From here, it's straightforward to calculate a few other important mode parameters, including the maximum spot size (which occurs at the curved mirrors) and the spot size between the flat mirrors (henceforth referred to as the "auxiliary" waist; the waist between the curved mirrors will be the "primary" waist). The maximum spot size can be found from simply propagating the Gaussian mode from the primary waist out a distance  $L_0$  to the curved mirror, i.e.

$$w_{\max} = w_0 \sqrt{1 + (L_0/z_R)^2}, \quad (\text{A.14})$$

where  $w_0$  is the spot size at the primary waist ( $= \sqrt{\lambda z_R/\pi}$ ,  $\lambda$  the mode wavelength in the ambient medium). The auxiliary waist spot size can be found by applying the exact same analysis to find the Rayleigh range as was done for the primary waist above, but with the roles of  $L_0$  and  $L_1$  switched, and we thus obtain

$$z_{R\text{aux}}^2 = \frac{(f - L_1)(L_0 f + L_1 f - L_0 L_1)}{f - L_0}, \quad (\text{A.15})$$

with  $z_{R\text{aux}}$  the Rayleigh range of the auxiliary waist, and the corresponding spot size  $w_{\text{aux}} = \sqrt{\lambda z_{R\text{aux}}/\pi}$ . As an example, for a bowtie cavity with  $f = 50$  mm (i.e. curved mirror radius of curvature  $R = 10$  cm) and  $L_1 = 265.5$  mm we plot the behavior the relevant cavity spot sizes versus  $L_0$ . This example is the basis for the design of our OPO bowtie cavities.

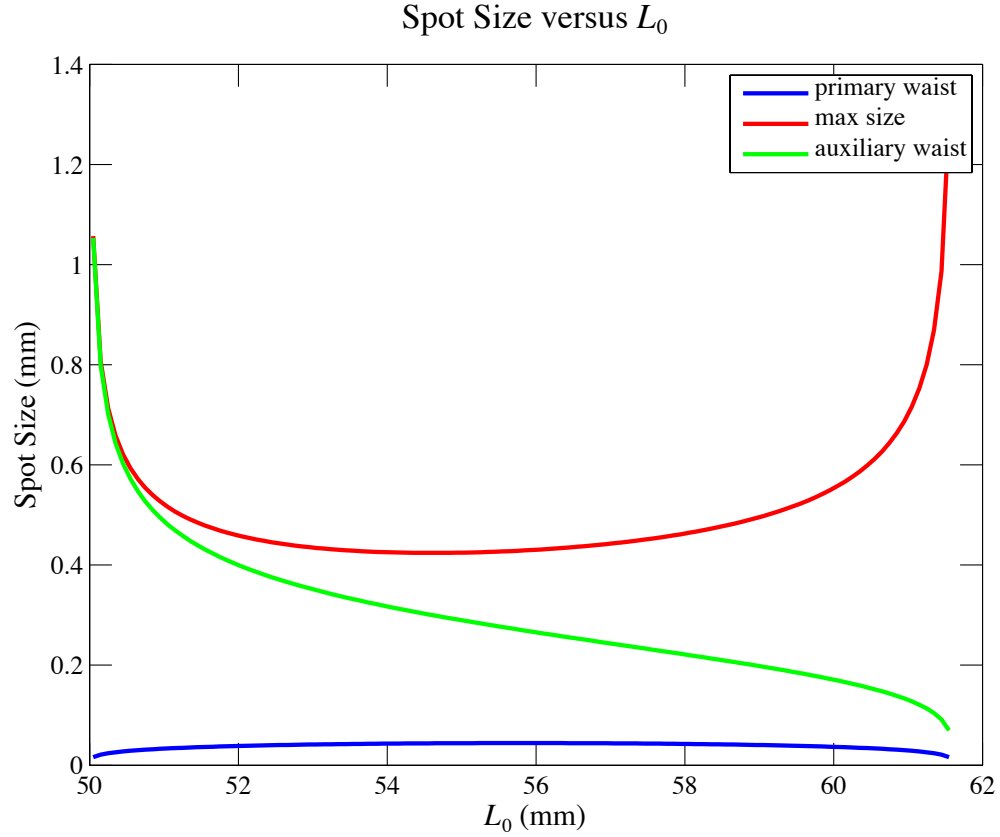


Figure A.3: Plot of relevant cavity spot sizes versus  $L_0$  for  $f = 50$  mm and  $L_1 = 265.5$  mm. The red, blue and green lines indicate the primary, max and auxiliary spot sizes respectively. At the edges of the stability boundary, the spot sizes either become very small or very large, and note that for this choice of  $L_1$ , the range of  $L_0$  over which the cavity is stable is a little over 1.1 cm; this range can be increased by decreasing  $L_1$ , but at the expense of making the average primary waist spot size larger over it.

## A.2 Effects of Intracavity Crystal and Astigmatism

We next consider effects that can change the properties of the cavity mode and its stability: the effects of placing a crystal inside the cavity mode path, as well as astigmatism due to reflection off the curved mirrors at a non-zero angle of incidence.

As seen in fig. A.1, we let  $\ell$  be half the length of crystal, assume that it's centered between the curved mirrors, and has an index of refraction  $n$  (typical nonlinear crystals operating at the visible and near IR have an index of  $\sim 2$  at those wavelengths). We also assume that the crystal input and output facets are flat and normal to the mode propagation direction. Using the appropriate individual  $ABCD$  matrices for Gaussian beam propagation in a homogeneous medium with index  $n$  and transmission through the interface, we once again find the overall cavity roundtrip  $ABCD$  matrix from the primary waist:

$$\begin{aligned} \begin{bmatrix} A & B \\ C & D \end{bmatrix} &= \begin{bmatrix} 1 & \ell \\ 0 & 1 \end{bmatrix} \begin{bmatrix} 1 & 0 \\ 0 & 1/n \end{bmatrix} \begin{bmatrix} 1 & L_0 - \ell \\ 0 & 1 \end{bmatrix} \begin{bmatrix} 1 & 0 \\ -1/f & 1 \end{bmatrix} \\ &\quad \begin{bmatrix} 1 & 2L_1 \\ 0 & 1 \end{bmatrix} \begin{bmatrix} 1 & 0 \\ -1/f & 1 \end{bmatrix} \begin{bmatrix} 1 & L_0 - \ell \\ 0 & 1 \end{bmatrix} \begin{bmatrix} 1 & 0 \\ 0 & n \end{bmatrix} \begin{bmatrix} 1 & \ell \\ 0 & 1 \end{bmatrix}, \end{aligned} \quad (\text{A.16})$$

and we find that

$$A = \frac{f^2 - 2(L'_0 + L_1) + 2L'_0 L_1}{f^2}, \quad (\text{A.17})$$

$$B = \frac{2n[(L'_0 + L_1)f^2 - (L'^2_0 + 2L'_0 L_1)f + L'_0 L_1^2]}{f^2}, \quad (\text{A.18})$$

$$C = \frac{2(L_1 - f)}{nf^2}, \quad (\text{A.19})$$

$$D = \frac{f^2 - 2(L'_0 + L_1) + 2L'_0 L_1}{f^2} = A. \quad (\text{A.20})$$

where

$$L'_0 = L_0 + \ell \left( \frac{1}{n} - 1 \right). \quad (\text{A.21})$$

We see that the roundtrip  $ABCD$  matrix has a very similar form (though not identical, as there are factors of  $n$  appearing in  $B$  and  $C$ ) to the case of the empty cavity, except that  $L'_0$  is now the "effective" length from the curved mirror to the center of the crystal, and the change in length relative to the empty cavity value is  $\Delta L_0 = L'_0 - L_0 = \ell(1/n - 1)$  (a negative value with  $n > 1$ , i.e. the "effective" length is actually shorter). Note that  $L'_0 \rightarrow L_0$  if we take  $n \rightarrow 1$  (crystal index approaches air) or  $\ell \rightarrow 0$  (crystal length goes to zero), as expected. In the same manner as before, we solve the quadratic equation for the Rayleigh range of the mode *in* the crystal:

$$z_R^2 = \frac{-B}{C} = \frac{n^2(f - L'_0)(L'_0 f + L_1 f - L'_0 L_1)}{f - L_1}, \quad (\text{A.22})$$

and note the additional factor of  $n^2$  appears relative to empty cavity expression for  $z_R^2$  (the reason is that the wavelength in the crystal is down by a factor of  $n$  relative to the free space value; and thus substituting  $z_R = n\pi w_0^2/\lambda$ , the primary waist spot size in the crystal will be same as that for the corresponding empty cavity). We can now employ the same analysis as before to determine the cavity lengths over which the mode is stable, as well as the mode spot size in the crystal and other relevant beam parameters to determine the effect of the crystal on the cavity mode. An important point to note is that if an empty cavity is operating near the edge of stability with  $L_0$  near its minimum value (for e.g. in order to achieve a small spot size at the primary waist), then inserting the crystal into the cavity path can decrease the effective distance to the curved mirror such that mode then becomes unstable. Thus, the effect of the crystal should be taken into account; for e.g. with a 2 cm long PPLN crystal (so  $\ell = 1$  cm and  $n \approx 2.2$  at 1064 nm and 532 nm), we have that  $\Delta L_0 \approx 5.5$  mm. If our cavity has the design and properties as shown in fig. A.3, then we need to choose the empty cavity length  $L_0$  such that  $L_0 > 55.5$  mm if we want the mode to be stable with and without the crystal.

Next, we consider the astigmatic properties of the cavity mode. Astigmatism in

the bowtie cavity arises from the fact that the Gaussian mode reflects off the curved mirrors at non-normal incidence, and the effect is that an initially circular Gaussian beam will (when reflected) have a different Rayleigh range for the transverse direction parallel to the plane of incidence (called the tangential plane) than the direction perpendicular to it (called the sagittal plane) (see for e.g. §6.9 of [40]). In other words, if  $\theta$  is the angle of incidence on a curved mirror as shown in fig. A.1, then the "effective" focal length of mirror now becomes

$$f_t = \frac{f}{\cos \theta} \quad (\text{A.23})$$

in the tangential direction and

$$f_s = f \cos \theta \quad (\text{A.24})$$

in the sagittal direction, where  $f$  is the focal length of the mirror at normal incidence. Since these lengths are different for the two different transverse directions, we need to consider the stability of the cavity for both, i.e. replace  $f$  by  $f_t$  and  $f_s$  in turn in eqn. A.22. If  $\theta$  is large enough (and especially if the cavity is operating near the edge of the stability boundary) it's possible that the cavity will become unstable in either of the two transverse directions, i.e. the mode becomes unstable. Aside from the issue of mode stability, as mentioned before, the more astigmatic the mode, the more problematic it can be when used in subsequent processes whose efficiency depend significantly on matching it with other Gaussian beams with potentially different astigmatism (e.g. parametric amplification, homodyne detection and squeezed state injection into another cavity). Thus, in general it's desirable to minimize the cavity astigmatism, as well as use modes with as close an astigmatism as possible for processes where mode matching is important. In our bowtie cavity prototype example, we have that  $\theta \approx 4^\circ$ , which then changes the "effective" focal lengths by  $\sim 0.25\%$ , which is a small change, but one to be mindful of very near the stability boundary of the cavity.

In closing this section, we mention that by analogy we can apply the same analysis to determine the mode stability for an asymmetric bowtie cavity, or a ring cavity with

a different number and/or arrangement of mirrors, as long as we use the appropriate  $ABCD$  matrices to propagate the beam between each element of the cavity. The general case may have considerably more complicated expressions and numbers of terms involved (for e.g. in the asymmetric case astigmatism leads to different waist positions for each transverse direction of the mode, in addition to different Rayleigh ranges), and thus it's desirable when possible to keep the design symmetric, both for ease of intuition and for debugging problems during cavity construction.

### A.3 Cavity Frequency Response

The bowtie cavity frequency response depends on the cavity length, mirror reflectivities and intracavity losses. Here, we follow the analysis done in §11.3 of [41] done for a Fabry-Perot cavity, but generalize it to our four mirror bowtie cavity. The analysis is done neglecting any transverse variation in cavity properties, i.e. the mirrors and crystal facets are assumed to be planar with infinite transverse size and the cavity modes therefore planewaves; the result will give an excellent approximation of the longitudinal mode (i.e. TEM00) frequencies in the high longitudinal mode number regime for the actual cavity, which is the regime we're interested in. If desired, the "exact" longitudinal and higher order transverse mode frequencies can be found by accounting for the corresponding Guoy phase shifts in the Gaussian mode in each length of the ring cavity (see for e.g. §19.3 of [41]), but for our purposes an initial picture of the longitudinal mode response is sufficient.

Our cavity mirrors  $M_1$  through  $M_4$  (as shown in fig. A.1) have corresponding power reflectivities  $R_1$  through  $R_4$  and power transmittivities  $T_1$  through  $T_4$ . The corresponding electric field amplitude reflectivities and transmittivities are  $r_1 = \sqrt{R_1}$  and  $t_1 = \sqrt{T_1}$  and so on, i.e. the complex field amplitudes written below (denoted by tildes, e.g.  $\tilde{E}$ ) are at reference planes chosen such that  $r_j$  and  $t_j$  ( $j = 1, 2, 3, 4$ ) are real numbers; we are always free to choose this, and we'll treat each mirror as a dielectric slab per §11.1 of [41]. The roundtrip intracavity power loss due everything except transmission through the mirrors (i.e. losses due to absorption and scattering in the crystal and mirrors) is given by  $1 - F^2$ , where  $F < 1$  is a real multiplicative

factor on the circulating field amplitude due to these losses.

If we apply the self consistent condition that the circulating field at a reference plane just inside the input mirror  $M_1$  is due to the sum of the field incident on the input mirror and the circulating power from the previous cavity roundtrip, we can write it as

$$\tilde{E}_c = it_1 \tilde{E}_i + rF \exp(-i\omega p/c) \tilde{E}_c, \quad (\text{A.25})$$

where  $\tilde{E}_c$  is the circulating field amplitude,  $\tilde{E}_i$  the incident field amplitude at a *different* reference plane just before the input mirror,  $\omega$  the incident field angular frequency,  $r = r_1 r_2 r_3 r_4$  the product of the mirror amplitude reflectivities,  $p = 2(L_0 - \ell) + 2n\ell + 2L_1$  the cavity perimeter,  $c$  the speed of light in air/vacuum and  $i = \sqrt{-1}$ . After a little algebra, the ratio of the circulating power to the incident power can be found to be

$$\left| \frac{\tilde{E}_c}{\tilde{E}_i} \right|^2 = \frac{T_1}{1 + r^2 F^2 - 2rF \cos(\omega\tau)} \quad (\text{A.26})$$

where  $\tau = p/c$  is the cavity roundtrip time. Thus we see the circulating power is a periodic function of frequency, and the cavity mode frequencies (when the cavity roundtrip length equals a positive integer number of optical wavelengths, henceforth called resonances) are those at which circulating power reaches its maximum every  $\omega = 2\pi N/\tau = 2\pi N \cdot \text{FSR}$ , where  $N$  the a positive integer labeling each cavity mode and  $\text{FSR} = 1/\tau = c/p$  is the cavity free-spectral range, i.e. the spacing between adjacent modes in frequency. Note for cavities with  $p \sim 0.5$  m as in this experiment, with  $c \approx 3 \times 10^8$  m/s the FSR is  $\sim 0.5$  GHz, meaning that for the optical wavelengths ( $\sim 1 \mu\text{m}$ , corresponding to a frequency of  $\sim 300$  THz) that we're interested in,  $N \sim 6 \times 10^5 \gg 1$ , i.e. we're in the high mode number regime.

Now, we consider the frequency change off each resonance peak such that the circulating power falls to half its maximum value: call it  $\Delta\omega_{\text{HWHM}}$ , the half width half max (HWHM) of the resonance. From eqn. A.26 it can be shown with a little algebra that  $\Delta\omega_{\text{HWHM}}$  satisfies

$$\sin(\Delta\omega_{\text{HWHM}}\tau/2) = \frac{1 - rF}{2\sqrt{rF}} \equiv \frac{\pi}{2\mathcal{F}}, \quad (\text{A.27})$$

where

$$\mathcal{F} \equiv \frac{\pi\sqrt{rF}}{1 - rF} \quad (\text{A.28})$$

is defined to be the finesse of the cavity. If the mirror reflectivities are high enough and cavity losses low enough such that  $\mathcal{F} \gg 1$ , then we have that  $\sin(\Delta\omega_{\text{HWHM}}\tau/2) \approx \Delta\omega_{\text{HWHM}}\tau/2 \ll 1$  and the full width half max (FWHM) of the cavity mode is then

$$\Delta\omega_{\text{FWHM}} = 2\Delta\omega_{\text{HWHM}} \approx \frac{2\pi}{\tau\mathcal{F}} = \frac{2\pi\text{FSR}}{\mathcal{F}}, \quad (\text{A.29})$$

and the local lineshape around each resonance approaches the Lorentzian

$$\left| \frac{\tilde{E}_c}{\tilde{E}_i} \right|_{\text{local}}^2 \approx \frac{T_1}{(1 - rF)^2 + rF(\Delta\omega\tau)^2} \quad (\text{A.30})$$

where  $\Delta\omega$  is the frequency deviation off the resonance peak. Via a temporal Fourier Transform, it can be shown that the FWHM of the Lorentzian gives the cavity decay rate for the mode (i.e. time for stored energy in the mode to drop to  $\exp(-1)$  its initial value), and that the finesse  $\mathcal{F}$  gives a measure of the number of roundtrips each photon makes in the cavity before leaving it. The Lorentzian approximation of the resonance line shape is good even for cavities with  $\mathcal{F} \sim 10$ , which is the regime for the cavities in this experiment, and an example is plotted below.

In an analogous manner, the reflected field off the input mirror  $M_1$  can be found as the sum of the reflected incident field and the circulating field after one cavity roundtrip that's *transmitted* (instead of reflected) back out  $M_1$ :

$$\tilde{E}_r = r_1\tilde{E}_i + \frac{it_1rF \exp(-i\omega p/c)}{r_1}\tilde{E}_c, \quad (\text{A.31})$$

so that



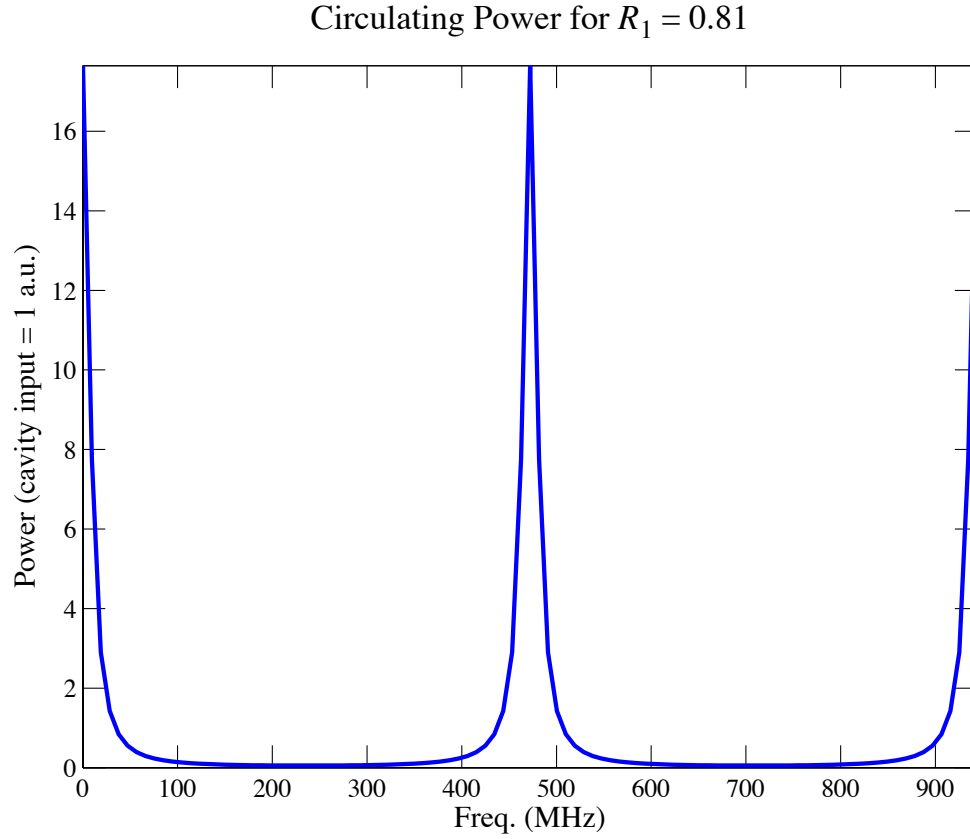


Figure A.4: Cavity circulating power versus input frequency for a bowtie cavity with mirror power reflectivities  $R_1 = 0.81$ ,  $R_2 = R_3 = 0.9999$ ,  $R_4 = 0.999$ , perimeter  $p = 0.635$  m and intracavity loss factor  $F = 0.998$ , corresponding to the parameters of our basic cavity design. The FSR = 472 MHz, FWHM linewidth = 17 MHz, and finesse  $\mathcal{F} = 28$ .

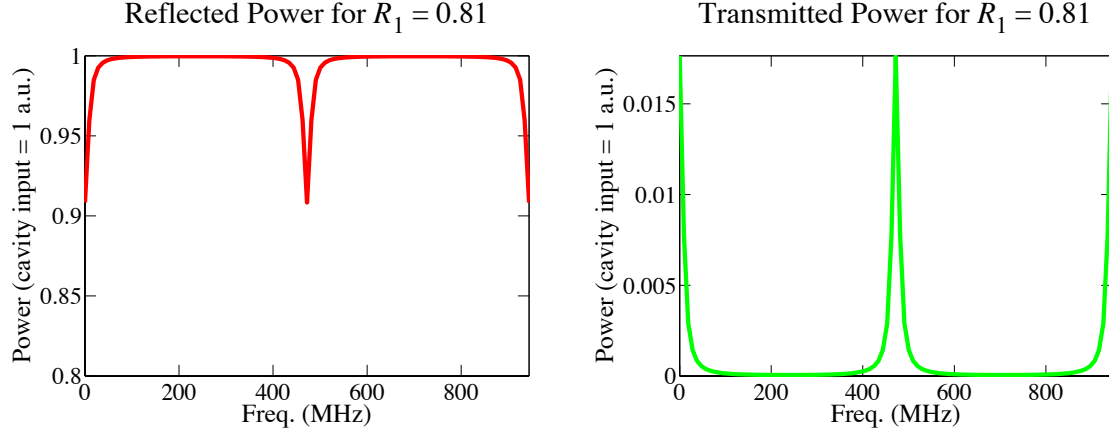


Figure A.5: Cavity reflected and transmitted power versus input frequency for a bowtie cavity with mirror power reflectivities  $R_1 = 0.81$ ,  $R_2 = R_3 = 0.9999$ ,  $R_4 = 0.999$ , perimeter  $p = 0.635$  m and intracavity loss factor  $F = 0.998$ , corresponding to the parameters of our basic cavity design. The FSR = 472 MHz, FWHM linewidth = 17 MHz, and finesse  $\mathcal{F} = 28$ ; the reflected power is off in the input mirror  $M_1$ , while the transmitted power comes out through  $M_4$ .

$$\left| \frac{\tilde{E}_r}{\tilde{E}_i} \right|^2 = \frac{1}{R_1} \frac{R_1^2 + r^2 F^2 - 2R_1 r F \cos(\omega\tau)}{1 + r^2 F^2 - 2r F \cos(\omega\tau)}, \quad (\text{A.32})$$

where  $\tilde{E}_r$  is the reflected field amplitude. Note that it's possible for the reflected power to go to zero (and this only occurs, as it can be shown, on resonance) if  $R_1 = rF$ , which is called the impedance matched condition (i.e. the input mirror power reflectivity is equal to the roundtrip field amplitude retention  $rF$ , which has contributions from all the mirror reflectivities and intracavity loss), and in this case the power transfer through the cavity is maximized. This can be useful for applications that require minimal reflected power and/or substantial transmitted power out the other cavity mirrors, but in our experiment all the mirrors are high reflectors ( $R_{i \neq 1} \leq 0.1\%$ ) except the input mirror  $M_1$ , which has  $R_1 \sim 80\%$ , so that we're far away from this condition.

Finally, the transmitted field from any of the other mirrors  $M_{i \neq 1}$  can be found by following the circulating field around its path in the cavity to the output mirror of interest. Starting from its initial position just inside the input mirror  $M_1$ , we keep

track of losses due to reflection of each mirror as well as any other intracavity loss along the path to the output mirror. If the output mirror of interest is for e.g.  $M_4$ , then we have

$$\tilde{E}_t = it_4 r_3 r_2 F_t \exp(-i\omega p_t/c) \tilde{E}_c, \quad (\text{A.33})$$

so that

$$\left| \frac{\tilde{E}_t}{\tilde{E}_i} \right|^2 = \frac{T_4 R_3 R_2 T_1 F_t^2}{1 + r^2 F^2 - 2rF \cos(\omega\tau)}, \quad (\text{A.34})$$

where  $p_t$  is the path length from the input mirror to the output mirror and  $F_t$  is the amount of intracavity loss up to the output mirror. For our bowtie cavity design as shown in fig. A.1, the intracavity loss on the last part of the cavity roundtrip from  $M_3$  to  $M_4$  is very small, so we essentially have  $F_t = F$  (since the dominant loss comes from absorption and scattering from the crystal), and we plot an example of reflected and transmitted fields in fig. A.5. Both dip in reflected power and the peak in the transmitted power have the same lineshape as the circulating power, and can be used to lock the cavity to the resonance frequency via for e.g. the Pound-Drever-Hall technique [35]. The magnitude of dip/peak can also be used to confirm the amount of intracavity loss present in the cavity.

# Appendix B

## Electronics for locking and detection

This Appendix contains the circuit level schematics for the homemade electronics used in the apparatus for cavity and phase locking, as well as the detector designs. We won't go into a detailed description of their operation or their components here, but rather will note their general function along with their schematic to aid the next researcher at the highest level in using or duplicating them for their own purposes. Once again, a hearty thanks to Hardeep(s), Nate, Yeong Dae, Charles, and the Catcher in the Lab for their help with assembling and debugging the veritable army of servos, amplifiers and detectors used in the apparatus!

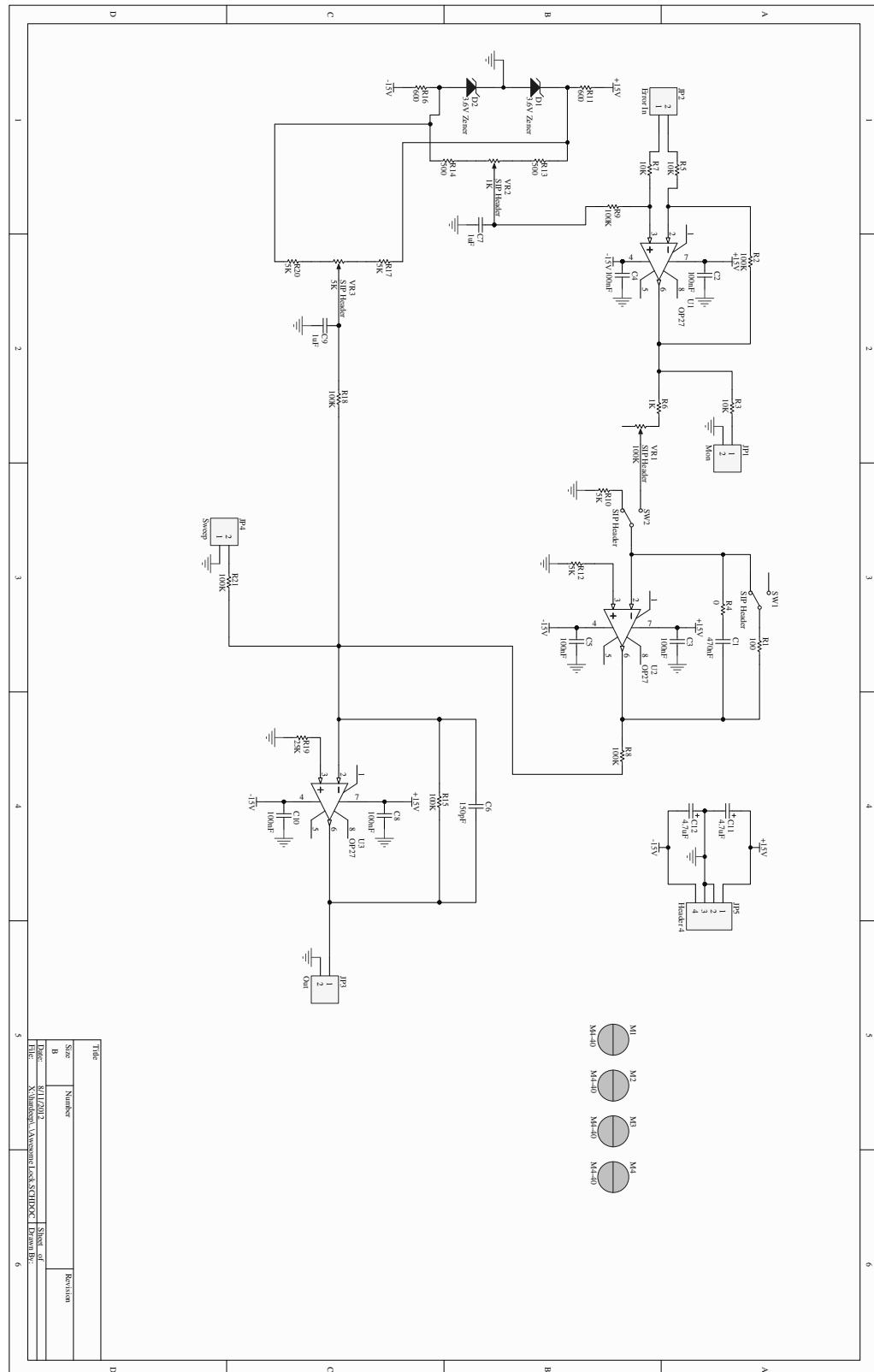
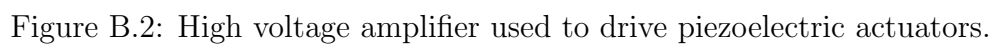


Figure B.1: Simple servo utilizing integral control for cavity locking and phase locking.



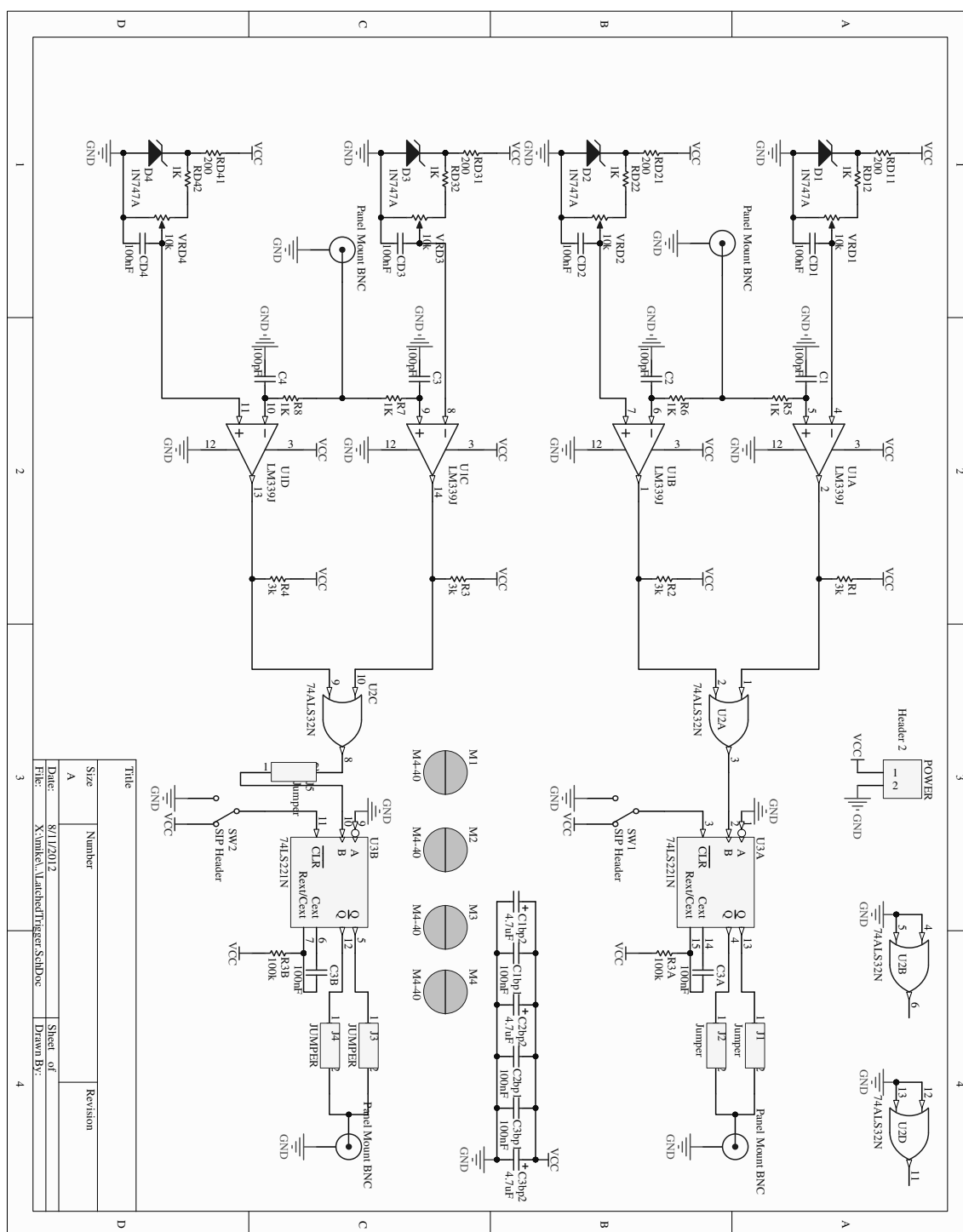


Figure B.3: Latched trigger (two output ports) for resetting piezo position during phase locking when end of range reached.

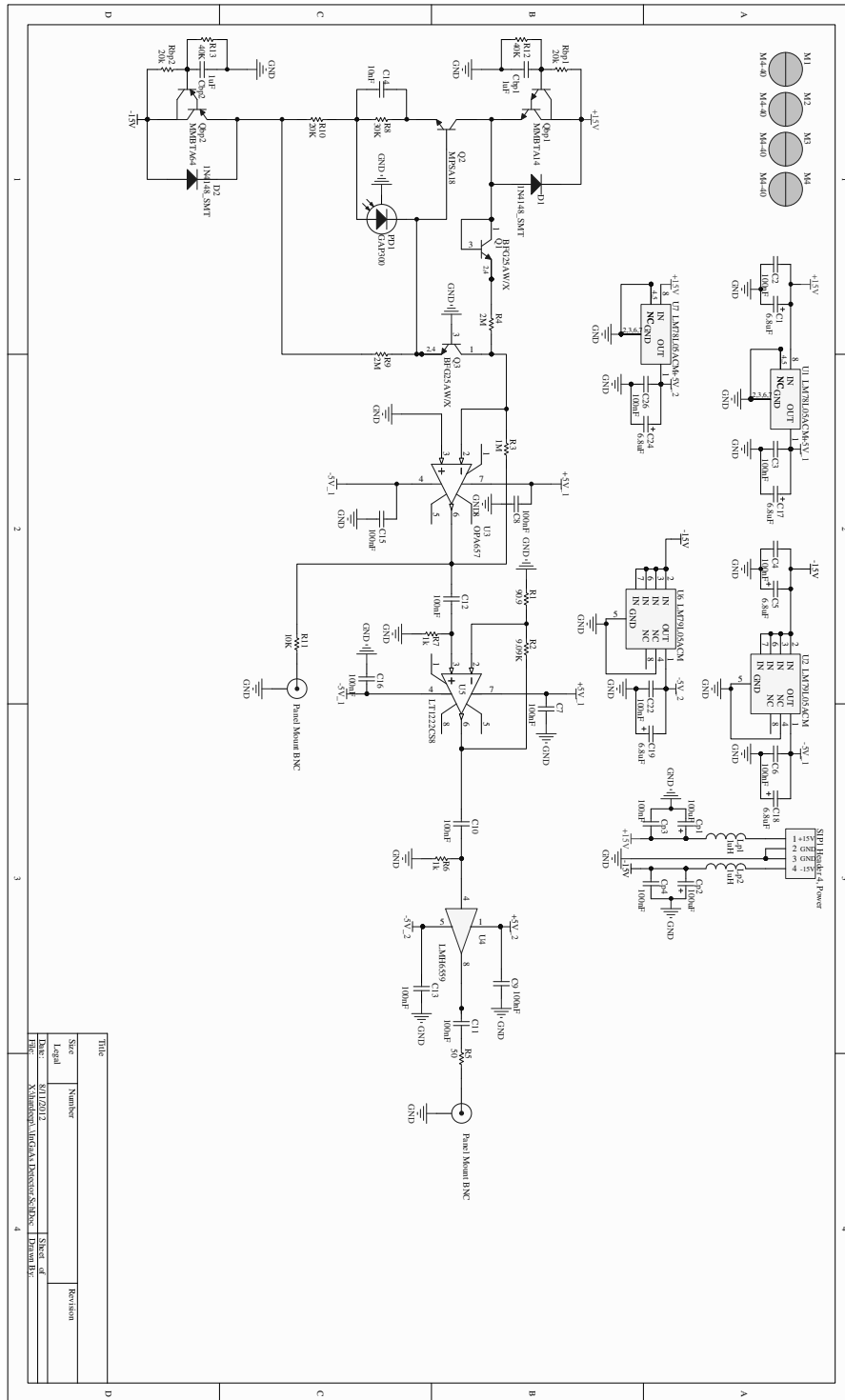


Figure B.4: 1 MHz bandwidth detector used to measure cavity transmission.





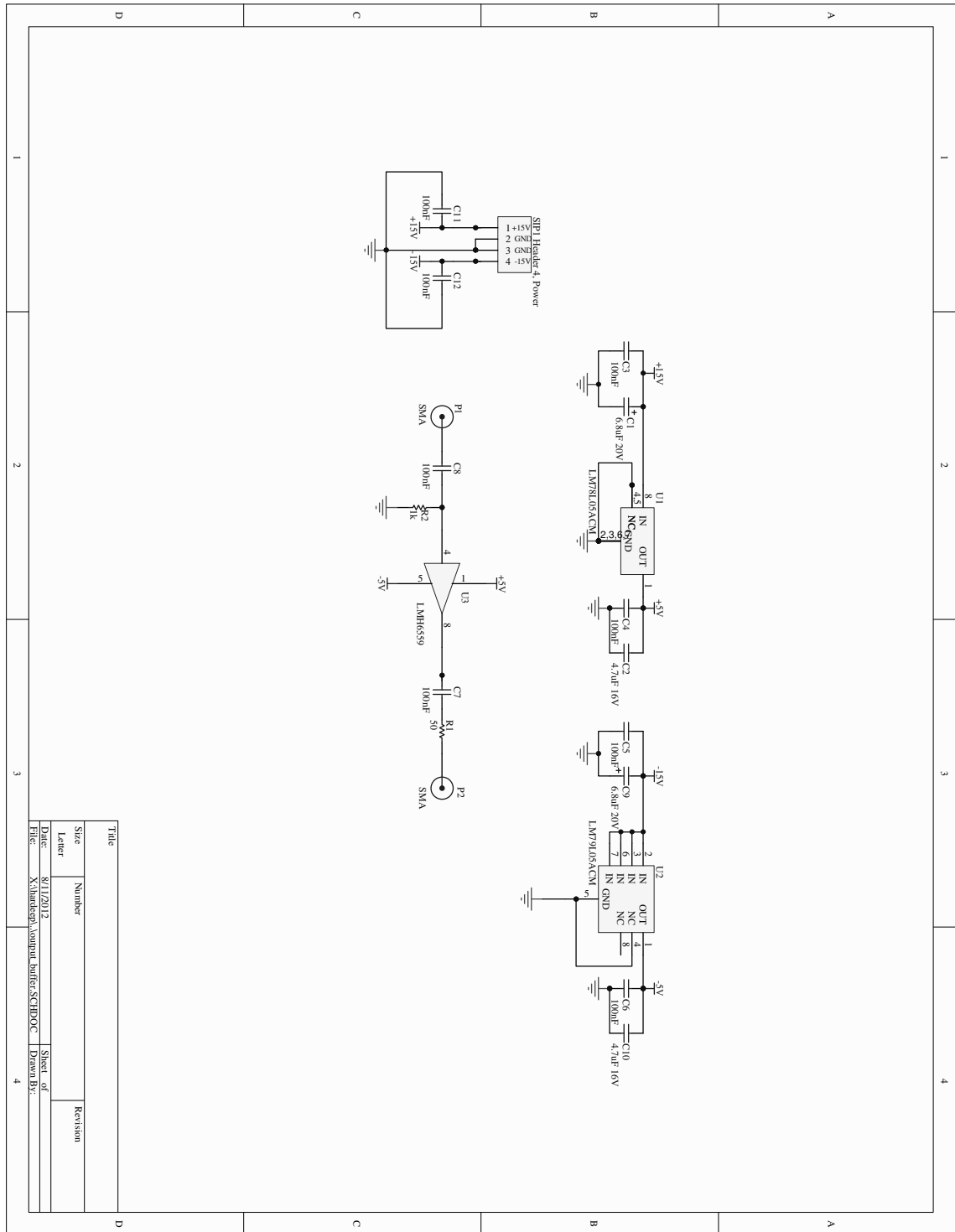


Figure B.6: Output buffer to enable subtracting detector to drive low impedance loads.

# Appendix C

## SHG and OPA with $\chi^{(2)}$ crystals in practice

This Appendix focuses on how to do second harmonic generation (SHG) and optical parametric amplification (OPA) with nonlinear optical crystals in the lab, and is essentially garnered from my own practical experiences (in this Appendix, the royal "we" finally switches to the humble "I").

### C.1 Second harmonic generation

Second harmonic generation (SHG) is used to generate the 532 nm beam used in this experiment (here, it's the pump beam for the parametric oscillations that squeeze of the cavity modes of interest). I briefly review the values of second harmonic (SH) power I obtained when attempting SHG in a bulk periodically poled Lithium Niobate (PPLN) crystal and a bulk periodically poled Potassium Titanyl Phosphate (PPKTP) crystal, and compare with the values predicted from textbook calculations. I then also note some important things I came across in trying to get the process to work in the lab, which should be helpful to others attempting to work with these processes in the future.

When working with  $\chi^{(2)}$  nonlinear optical processes, it really is worth it to make sure that one can do SHG properly before moving on to other processes, both because

SHG is the most basic (it has only one non-zero input field, i.e. the fundamental or "pump" beam) and thus most transparent to potential problems, and because it's useful in aligning more complicated processes, e.g. parametric amplification.

The fundamental beam for the SHG process that I describe here was for the MOPA YAG laser beam at 1064.4 nm, focused relatively loosely to a  $\sim 55 \mu\text{m}$  spot inside the crystal (or so I had thought at the time!), which then generated the SH beam at 532.2 nm. The first crystal I tested was a bulk MgO doped PPLN crystal from Covision (the MgO doping significantly increases the laser power damage threshold of the material, and thus the achievable SH power), and after some optimization steps that I describe below, I was able to obtain *a lot* of SH power (see fig. C.1).

The predicted values come from the idealized expression found in textbooks [37] for an incident planewave beam of finite size (that's the idealization of a Gaussian beam), perfectly phase matched to the crystal and includes pump depletion:

$$P_{SH} = P_p \tanh^2 \left( \frac{\sqrt{2}\omega d_{\text{eff}} L}{n_0^{3/2}} \left( \frac{\mu_0}{\epsilon_0} \right)^{3/4} \sqrt{\frac{P_p}{A}} \right) \quad (\text{C.1})$$

which is  $\propto P_p^2$  for low pump powers (note  $\tanh^2(x) \approx x^2$  for  $x \ll 1$ ). Above,  $P_p$  is the pump power,  $\omega$  the pump frequency,  $d_{\text{eff}}$  the effective nonlinear coefficient for the periodically poled crystal,  $L$  the crystal length,  $n_0$  the crystal index of refraction near the pump and second harmonic frequencies,  $\mu_0$  and  $\epsilon_0$  the vacuum permeability and permittivity, and  $A$  the beam area). In practice, in order to get the actual measured SH power values to agree with these predicted values, there are several things that need to be carefully considered in the setup, as described further below.

Next, I tested the bulk hydrothermal PPKTP crystal obtained from AdvR. Although PPLN was expected to have the higher nonlinear coefficient (as well as potentially damage threshold) and would thus be more useful in generating SH power, the performance of the PPKTP was important because the crystal material can also be used in other types of nonlinear processes (e.g. particular Type II parametric amplification where the signal and idler beams have orthogonal polarizations relative to each other; PPLN can also support this process but is harder to find from companies for this interaction). Without changing the the pump beam at all, I found that the

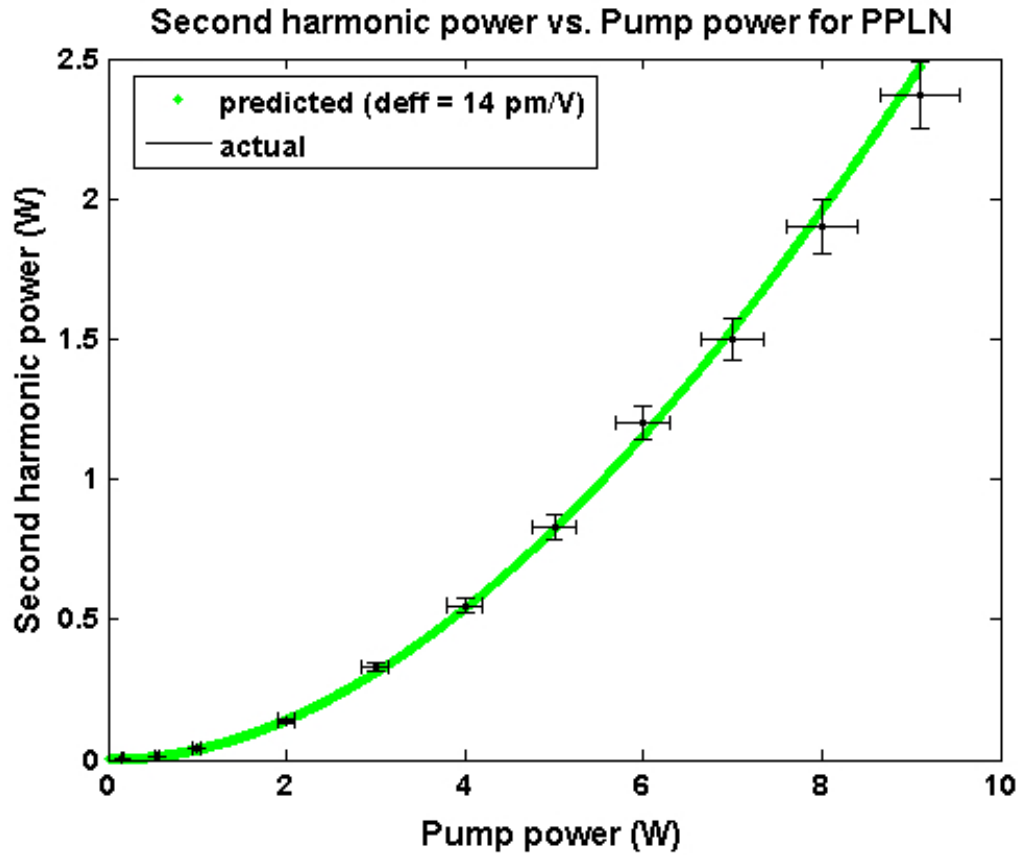


Figure C.1: Multi-watt second harmonic generation on a single pass through PPLN. The horizontal and vertical errorbars come from the specs for the calibration accuracy of the Thorlabs PM50 thermal power meter. The value of  $d_{\text{eff}}$  was obtained by fitting the textbook equation for planewave SHG to the data *assuming* the beam spot size was  $\sim 55 \mu\text{m}$ , but as I would later discover, the beam was thermally lensing and focusing to a smaller spot in the crystal; the true value of  $d_{\text{eff}}$  was closer to  $9 \text{ pm/V}$ , as could be seen by repeatedly measure the SH power for lower fundamental powers and various known spot sizes.

expected power was less than the predicted value given me by the company (see fig. C.2).

Now we'll talk about some of those details I mentioned to optimize the SHG in practice for a given crystal. The first consideration is the focusing and quality of the pump beam itself. Assuming an ideal TEM00 Gaussian pump beam, for a bulk  $\chi^2$  nonlinear crystal of given length and index Boyd and Kleinman ([34], a solid 43 page analysis) worked out the choice of beam parameters which maximizes the power generated in the SH beam (which would then also be an ideal TEM00 Gaussian beam). Specifically, the pump focus should be at the center of the crystal, and the Rayleigh range of the beam  $z_R$  in the crystal material  $= L/5.68$  (which then also sets the optimum spot size; note that when comparing a Gaussian beam in free space to its counterpart in the crystal, the beam focuses more slowly in the crystal so its Rayleigh range is down by a factor of the crystal index  $n_0$ , but the spot size at the waist remains the same). The Boyd-Kleinman analysis is exact in its inclusion of the Gaussian nature (i. e. in both real space and momentum space) of the beams, and it's important to note that overfocusing a beam not only reduces efficiency because the average beam area inside the crystal eventually gets larger (and thus the average intensity reduced), but also because the momentum space distribution of the Gaussian becomes broader and thus the phase matching becomes poorer. Fortunately, the analysis shows that the drop in process efficiency isn't extremely sharp for focusing conditions a little away from the optimum (for e.g. loosening the focusing to  $z_R = L/2$  still gives  $\approx 83\%$  of the optimal power), so it gives a good ballpark to shoot for when setting up the incident beam. It's also important to note that when turning up the power in a high power laser system (such as the Mephisto YAG MOPA) via the drive current, the beam size and parameters may change as the power is increased, due to for e.g. spatial saturation of the gain medium (here the YAG crystals) with increasing laser diode pump power (this is also noted in Chapter 3). Thus, it's usually best to keep the laser power output fixed while using another means to control the power of the beam that you want to use (e.g. waveplates with polarizing beam-splitters; *absorptive attenuators* will control the power, but at high powers they will also act a little like lenses and change the focusing properties of the beam, so be aware of this

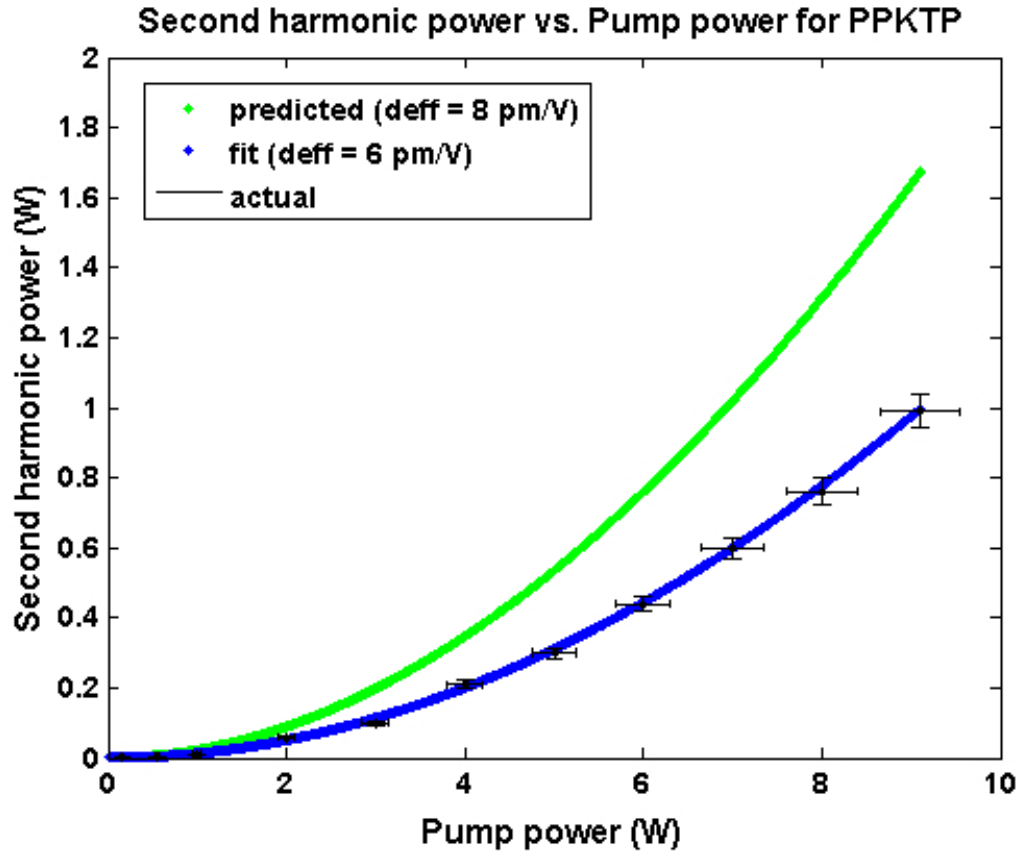


Figure C.2: Single watt second harmonic generation on a single pass through PPKTP. Again, the horizontal and vertical errorbars come from the specs for the calibration accuracy of the Thorlabs PM50 thermal power meter. By fitting, I measured the value of  $d_{\text{eff}}$  to be 6 pm/V instead of the 8 pm/V given to me by the company, but again thermal lensing was giving me a slightly higher value than actual, which turned out to be closer to 4.5 pm/V, half that of the PPLN.

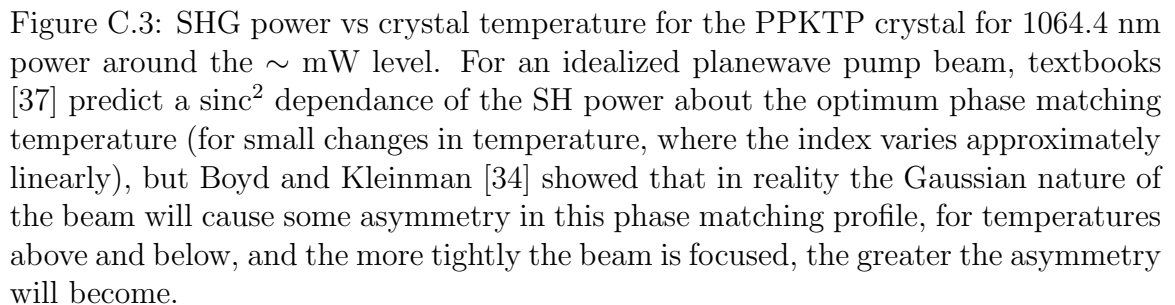
fact), so that the beam size and focusing remains fixed; and as usual, initial alignment into the crystal should be done with a lower power beam.

Just as important as the beam size, good beam "quality" (i.e. lack of substantial beam aberration) is crucial to getting high process efficiency, and in particular the beam behavior near the focus is important as that's what the crystal "sees" during the SHG process. Longitudinal spherical aberration from singlet lenses and/or truncation by apertures can cause a "hole" to form in the center of the beam near the focus on one side or the other, which then not only causes the generated SH beam to potentially have a "hole" (even in the far field), but also distorts the momentum space distribution of the field and thus reduces phase matching efficiency. The Spiricon beam imaging camera is an essential tool to monitor the beam behavior near the focus, as well as accurately measure the focused spot size for an accurate comparison with theory. Techniques to avoid aberrating the beam include the use of aspheric lenses when focusing/expanding the beam and to avoid moderately large beam spot sizes incident on 1 in. diameter optics (especially lenses), as these can lead to significant aberrations near the desired eventual focus, even if the beam itself appears to be undistorted in the far field.

Once the incident pump beam is reasonably focused and aligned into the crystal, the crystal temperature should be adjusted around the phase matching temperature until SH light becomes visible (note that even if the IR pump beam power is low, say 10's of  $\mu\text{W}$ , and the SH beam is  $\sim \text{nW}$  or a little less, the SH spot near the focus will still be visible to the naked eye off a white card or with room lights off). It's worth mentioning that the phase matching temperature that companies give for the crystal is a good starting point for the temperature search, but sample variation during crystal manufacture as well as the actual output wavelength of your laser may require you to sweep the temperatures a few degrees to find the optimum value. An actual SH power vs. temperature profile I obtained during the search for the optimum with the PPKTP crystal looks like can be seen in fig. C.3.

Another important point to note is that if absorption at either the pump or the SH wavelength is appreciable (e.g. in PPLN it's only  $0.1\% \text{ cm}^{-1}$  at 1064 nm, but it's  $3.4\% \text{ cm}^{-1}$  at the 532 nm—that's  $6.8\%$  for a 2cm long crystal), local heating effects can be





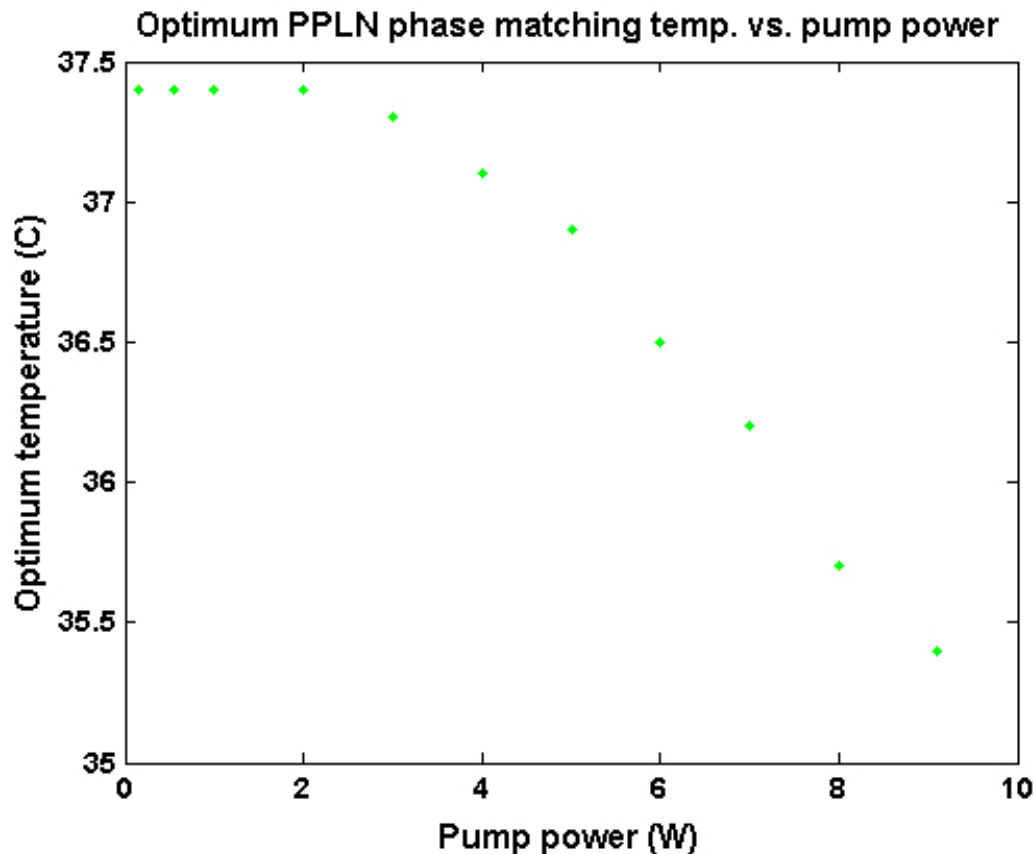


Figure C.4: The optimal phase matching temperature in PPLN for SHG decreases as the fundamental power becomes high, and thus temperature (and sometime longitudinal alignment) should be re-optimized.

considerable and both the alignment (particularly along the beam propagation axis) and the phase matching temperature should be re-optimized as power is increased. For PPLN, because of increased local heating, the optimum set temperature of the crystal decreased with increasing pump power, as shown in fig. C.4.

It's important to note that for the PPLN crystal, since the generated SH beam is the dominant contributor to local heating, at the highest powers a small deviation off the optimum temperature setting can actually cause the generated SH power to drop sharply: as the SH power decreases, the local heating decreases causing a shift away (or towards and perhaps past) from the phase matching temperature, which then further decreases the SH power, which further moves temperature away from phase

matching, etc. Thus, as noted before, at high power levels it's best to turn up the pump power gradually and allow the effects of local heating to equilibrate at a given power, and optimize the set temperature of the crystal for phase matching, before further increasing the pump power. In contrast with the PPLN crystal, because of its lower absorption at both pump and SH wavelengths ( $< 1\% \text{ cm}^{-1}$ ) (which make the effects of local heating less prominent), the set temperature for the PPKTP crystal for optimum phase matching is approximately constant, even at the highest powers.

Some final remarks about laser frequency and SHG are also in order. At a fixed temperature, the spectral acceptance bandwidth of the periodically poled crystals is determined by the number of poling periods in the crystal (knowing this number gives an estimate of the ideal behavior of the crystal assuming perfect poling [37]), and the actual behavior of the crystal can be found by fixing the temperature and sweeping the laser frequency (here, I swept the temperature of the YAG crystal in the laser and monitored the frequency of the output with the Burleigh wavemeter; see fig. C.5).

When I sweep the laser frequency, I see that for the PPKTP crystal the spectral acceptance bandwidth has a  $\sim 40 \text{ GHz}$  FWHM, which is actually broader than the  $\sim 30 \text{ GHz}$  tuning range of the laser. The laser modehops about every  $\sim 3 \text{ GHz}$  or so over its tuning range, causing a need for re-optimization of the alignment and leads to some variation of the total detected power. However, what is *not* shown in the above plot is the detected SH power during the laser modehop, which can actually be substantially greater than the values during single mode operation (I've observed increases by as much as a factor  $1.4$  to  $1.5 \times$ ); this actually stems from the fact that during modehopping, when two modes of comparable amplitude and frequency separation substantially less than the spectral acceptance width of the crystal are simultaneously lasing, the peak electric field amplitude of the sum (which can be written as a "slowly" varying envelope modulating a carrier at the average mode frequency) can be larger than the single mode case (for the same total laser optical power), which is the quantity relevant for SHG, thus giving rise to higher SH power. However, you usually want a stable frequency operation regime for your laser in an actual experiment, so it's best to confirm that the laser is single mode, and generated SH power is what you would expect for single mode operation.

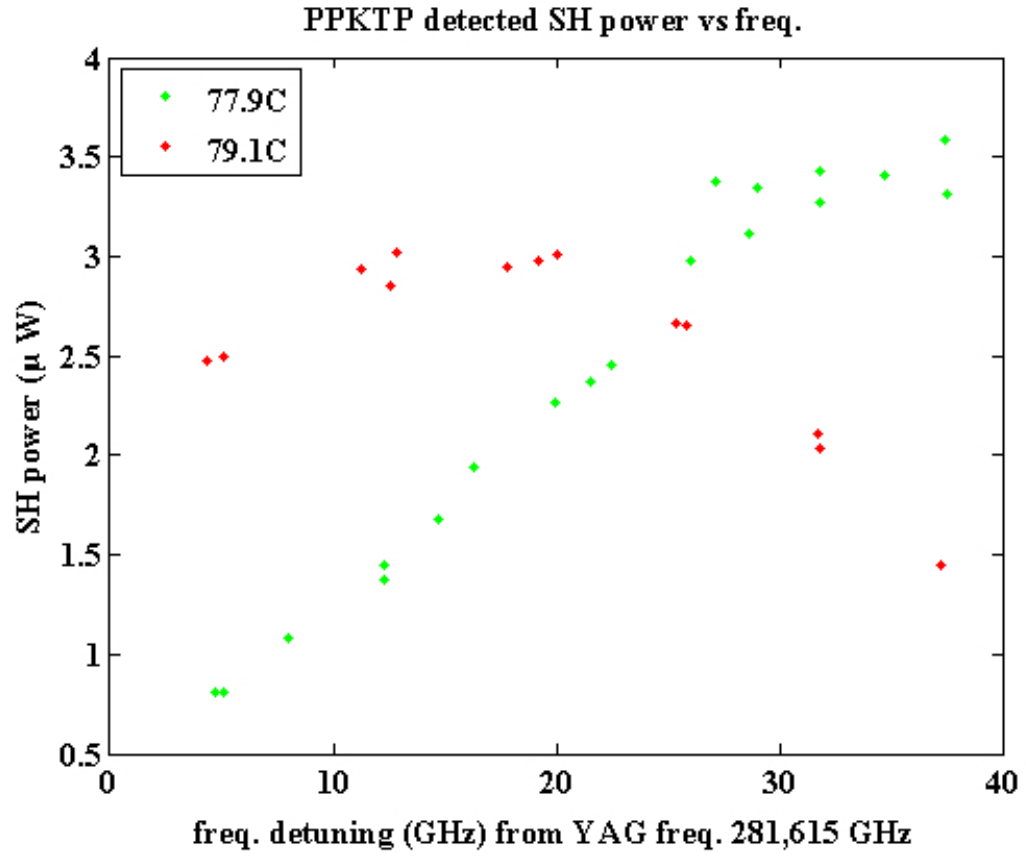


Figure C.5: SHG as the laser frequency is tuned for two different (fixed) PPKTP crystal temperatures.

Now, at this point you might ask, "what happened to that amazing 2.4 W of SH power that was generated, you should be able to drive both OPOs independently above threshold and still have power to spare?" The answer is that that power didn't last very long, mainly because the crystal couldn't stand it (as seen in fig. C.4, it was generated from the lowest temperature grating, and thus local heating and thermal lensing was very strong). A few days later I measured it to be 1.8 W, and the optimum phase matching temperature had increased; over the months it continued a steady decline, until it finally settled below 0.5 W. I switched to the next higher temperature grating (phase matching at  $\approx 60^\circ\text{C}$ ), which gave about 1 W (consistent with the  $d_{\text{eff}}$  values = 9 pm/V I measured for the remaining crystals) to start with, but it too began to degrade, dropping to 0.7 W over a few days, and then even lower. Switching tactics, I decided to try the highest temperature grating (phase matching at  $\approx 120^\circ\text{C}$ ) which should have been most robust to degradation, but for some reason was never able to get an appreciable amount of SH light from it, despite knowing that the fundamental beam was clearly going through the grating and the temperature swept over the far below and above the supposed phase matching value. The same was true for the next lower temperature grating, but for some reason the third (and central) grating in the crystal worked fine—but only to start with! In the final days on which I worked on the experiment, it too degraded substantially until the power dropped below the level needed to drive the "plant" OPO above threshold.

For high power SHG, my recommendation would be to try the highest temperature gratings first, as they should (in principle!) be the slowest to degrade, and also least susceptible to temperature gradients formed by local heating as the heat generated by the beam should be a smaller fraction of the total heat transferred to the crystal from its immediate environment (i.e. the oven and the beam). This then should reduce the effect of thermal lensing, which not only may prevent the beam from overfocusing, but will also allow the output SH beam parameters to be more stable with time as the crystal wears.

## C.2 Optical parametric amplification

This section will be much more brief than the previous one on SHG as it builds on the information presented there. No diagrams this time, just a few words of "wisdom".

The process of degenerate (the case we'll focus on here) optical parametric amplification (OPA) is very similar to SHG except that now the fundamental beam is amplified by the SH beam, with the SH input power typically much greater than the fundamental power. Boyd and Kleinman [34] once again found that optimal SH beam for transferring SH power to the fundamental would have the same Rayleigh range and same waist position as the fundamental beam (and thus have a waist that's smaller by a factor of  $\sqrt{2}$ ; it would have exactly the same beam parameters as the SH beam *generated* by the fundamental). This immediately suggests a good trick for finding the optimal beam parameters for the 532 nm beam to pump the crystal with: send in enough fundamental power to generate a SH beam, measure that beam's parameters, and then select lenses and lens positions to try to match the 532 nm pump beam to it (a backwards generated SH beam would work fine for this as well).

This actually works reasonably well: you can use an iris pair to get both signal (i.e. fundamental) and pump beams close to each other, or rasterize the pump beam across the face of the crystal, and you should be able to get a parametric amplification/de-amplification effect on the signal as the phases of the two beams are swept relative to each other. One catch is that (like in many mode matching scenarios) it's unlikely that the lenses, their positions and the beam directions in the crystal will be optimal, so you'll have to do some varying of each of these things to try to optimize the amplification.

But, even when this is done, it can be difficult to get close to a coupling efficiency that gets the measured amount of amplification close to what would be predicted by textbook planewave formulas (again, the Gaussian nature of the beams does have some role to play in the discrepancy you see). One final trick (actually the first thing I tried, when there was space to do so!) is to actually image the beams at their focus (with the crystal removed), since this is where the dominant part of the interaction and power transfer occurs. Doing this with the Spiricon camera allowed me to not

only match the spot sizes accurately to their appropriate relative values at the beam waists, but perhaps more importantly confirm that the actual longitudinal location of the waists were on top of each other by  $< 1$  mm. Longitudinal misalignments can be more difficult to detect by just looking at the beams in the far field, but unfortunately they can reduce the coupling efficiency by a significant amount. Using this trick, I managed to achieve a very high pump coupling efficiency for the "controller" OPO at the start, but unfortunately this was lost as the doubling crystal degraded, and the pump power reduced (simultaneously reducing its own thermal lensing and thus changing its beam parameters). Later, with more optics on the table, there was no room to repeat this trick, so the best I could do is what is mentioned in the previous paragraph; that was still adequate to get appreciable gain from the "controller", but it's been difficult to approach the optimum value I found before. If the power of the Catcher in the Lab can be harnessed, however, anything becomes possible...

# Bibliography

- [1] K. Astrom and R. M. Murray. *Feedback Systems: An Introduction for Scientists and Engineers*. Princeton University Press, 2008.
- [2] V. P. Belavkin. On the theory of controlling observable quantum systems. *Autom. Rem. Control*, 44(2):178, 1983.
- [3] H. M. Wiseman and G. J. Milburn. Quantum theory of optical feedback via homodyne detection. *Phys. Rev. Lett.*, 70(5):548, 1993.
- [4] A. C. Doherty et al. Quantum feedback control and classical control theory. *Phys. Rev. A*, 62(1):1–13, June 2000.
- [5] H. M. Wiseman and G. J. Milburn. *Quantum Measurement and Control*. Springer, 2009.
- [6] W. Smith et al. Capture and Release of a Conditional State of a Cavity QED System by Quantum Feedback. *Phys. Rev. Lett.*, 89(13):3–6, September 2002.
- [7] M. Armen et al. Adaptive Homodyne Measurement of Optical Phase. *Phys. Rev. Lett.*, 89(13):1–4, September 2002.
- [8] P. Bushev et al. Feedback Cooling of a Single Trapped Ion. *Phys. Rev. Lett.*, 96(4):1–4, February 2006.
- [9] G. G. Gillett et al. Experimental Feedback Control of Quantum Systems Using Weak Measurements. *Phys. Rev. Lett.*, 104(8):2–5, February 2010.



- [10] C. Sayrin et al. Real-time quantum feedback prepares and stabilizes photon number states. *Nature*, 477:73, August 2011.
- [11] V. P. Belavkin. Quantum stochastic calculus and quantum nonlinear filtering. *J. Multivariate Anal.*, 42:171, 1992.
- [12] R. van Handel L. Bouten and M. R. James. An introduction to quantum filtering. *SIAM J. Contr. Optim.*, 46(6):79, 2007.
- [13] A. Faraon et al. Integrated quantum optical networks based on quantum dots and photonic crystals. *New J. Phys.*, 13:055025, 2011.
- [14] S. Lloyd. Coherent quantum feedback. *Phys. Rev. A*, 62:022108, 2000.
- [15] H. Mabuchi. Coherent-feedback quantum control with a dynamic compensator. *Phys. Rev. A*, 78(3):1–5, September 2008.
- [16] S. Iida et al. Experimental Demonstration of Coherent Feedback Control on Optical Field Squeezing. *IEEE Trans. Autom. Contr.*, 57:2045, August 2012.
- [17] R. Hamerly and H. Mabuchi. Advantages of Coherent Feedback for Cooling Quantum Oscillators. *arXiv*, page 1206.0829, 2012.
- [18] R. Hamerly and H. Mabuchi. Coherent controllers for optical-feedback cooling of quantum oscillators. *arXiv*, page 1206.2688, 2012.
- [19] H. Mabuchi. Coherent-feedback control strategy to suppress spontaneous switching in ultralow power optical bistability. *Appl. Phys. Lett.*, 98:193109, May 2011.
- [20] J. Kerckhoff et al. Designing Quantum Memories with Embedded Control: Photonic Circuits for Autonomous Quantum Error Correction. *Phys. Rev. Lett.*, 105:040502, 2010.
- [21] J. Kerckhoff et al. Design of nanophotonic circuits for autonomous subsystem quantum error correction. *New J. Phys.*, 13:055022, May 2011.

- [22] B. Park et al. Photonic Crystal Fiber Tip Sensor for High-Temperature Measurement. *IEEE Sensors J.*, 11(11):2643, 2011.
- [23] R. L. Hudson and K. R. Parthasarathy. Quantum Ito's formula and stochastic evolutions. *Comm. Math. Phys.*, 93(3):301, 1984.
- [24] H. J. Carmichael. Quantum trajectory theory for cascaded open systems. *Phys. Rev. Lett.*, 70(15):2273–2276, 1993.
- [25] A. S. Parkins C. W. Gardiner and P. Zoller. Wave-function quantum stochastic differential equations and quantum-jump simulation methods. *Phys. Rev. A*, 46(7):4363–4381, 1992.
- [26] H. I. Nurdin M. R. James and I. R. Petersen.  $H^\infty$  control of linear quantum stochastic systems. *IEEE Trans. Autom. Contr.*, 53:1787, September 2008.
- [27] I. R. Petersen H. I. Nurdin, M. R. James. Coherent quantum LQG control. *Automatica*, 45(8):1837, 2009.
- [28] M. R. James H. I. Nurdin and A. C. Doherty. Network synthesis of linear dynamical quantum stochastic systems. *SIAM J. Control Optim.*, 48:2686, September 2009.
- [29] C. W. Gardiner and P. Zoller. *Quantum Noise*. Springer, 2nd edition, 2000.
- [30] C. W. Gardiner. Driving a Quantum System with the Output Field From Another Driven Quantum System. *Phys. Rev. Lett.*, 70(15):2269–2272, 1993.
- [31] J. Gough and M. R. James. The Series Product and Its Application to Quantum Feedforward and Feedback Networks. *IEEE Trans. Auto. Control*, 54:2530, 2009.
- [32] R. C. Dorf and R. H. Bishop. *Modern Control Systems*. Prentice Hall, 9th edition, 2001.
- [33] J. E. Gough and S. Wildfeuer. Enhancement of field squeezing using coherent feedback. *Phys. Rev. A*, 80:042107, Oct 2009.

- [34] G. D. Boyd and D. A. Kleinman. Parametric Interaction of Focused Gaussian Light Beams. *J. Appl. Phys.*, 39:3597, 1968.
- [35] E. D. Black. An introduction to Pound-Drever-Hall laser frequency stabilization. *Am. J. Phys.*, 69:79, January 2001.
- [36] R. A. Boyd et al. Teaching physics with 670nm diode lasers—experiments with Fabry-Perot cavities. *Am. J. Phys.*, 64:1109, September 1996.
- [37] A. Yariv and P. Yeh. *Photonics: Optical Electronics in Modern Communications*. Oxford University Press, 6th edition, 2007.
- [38] P. K. Lam et al. Optimization and transfer of vacuum squeezing from an optical parametric oscillator. *Journal of Optics B: Quantum and Semiclassical Optics*, 1(4):469–474, August 1999.
- [39] A. Yariv. *Quantum Electronics*. Wiley, 3rd edition, 1988.
- [40] F. A. Jenkins and H. E. White. *Fundamentals of Optics*. McGraw-Hill, 4th edition, 1976.
- [41] A. E. Siegman. *Lasers*. University Science, 1986.